AFRL-VA-WP-TR-2006-3160

COMPUTATIONAL AND EXPERIMENTAL STUDIES TO DEMONSTRATE ACCURACY OF CRACK3D

Delivery Order 0001: Stable Tearing Predictions Using Large Deformation Kinematics and General 3D Crack Growth Algorithms Under Mixed Mode Loading Conditions

Prof. Michael A. Sutton
Prof. Xiaomin Deng
Dr. Jianzheng Zuo

University of South Carolina
Department of Mechanical Engineering
Columbia, SC 29208

MARCH 2006

Final Report for 05 February 2005 – 31 March 2006

Approved for public release; distribution is unlimited.

STINFO COPY

AIR VEHICLES DIRECTORATE
AIR FORCE MATERIEL COMMAND
AIR FORCE RESEARCH LABORATORY
WRIGHT-PATTERSON AIR FORCE BASE, OH 45433-7542

NOTICE AND SIGNATURE PAGE

This report was cleared for public release by the Air Force Research Laboratory Wright Site (AFRL/WS) Public Affairs Office and is available to the general public, including foreign nationals.

Copies may be obtained from the Defense Technical Information Center (DTIC) (http://www.dtic.mil).

AFRL-VA-WP-TR-2006-3160 HAS BEEN REVIEWED AND IS APPROVED FOR PUBLICATION IN ACCORDANCE WITH ASSIGNED DISTRIBUTION STATEMENT.

*//Signature//

JIM A. HARTER, Senior Aerospace Engineer
Analytical Structural Mechanics Branch
Air Force Research Laboratory

//Signature//

ANDREW G. SPARKS, Chief
Analytical Structural Mechanics Branch
Air Force Research Laboratory

//Signature//

DAVID M. PRATT, Ph.D.
Technical Advisor
Structures Division

*Disseminated copies will show "//Signature//" stamped or typed above the signature blocks.

REPORT DOCUMENTATION PAGE

Form Approved
OMB No. 0704-0188

1. REPORT DATE *(DD-MM-YY)*	2. REPORT TYPE	3. DATES COVERED *(From - To)*
March 2006	Final	02/05/2005 – 03/31/2006

4. TITLE AND SUBTITLE

COMPUTATIONAL AND EXPERIMENTAL STUDIES TO DEMONSTRATE ACCURACY OF CRACK3D
Delivery Order 0001: Stable Tearing Predictions Using Large Deformation Kinematics and General 3D Crack Growth Algorithms Under Mixed Mode Loading Conditions

5a. CONTRACT NUMBER
FA8650-04-D-3446-0001

5b. GRANT NUMBER

5c. PROGRAM ELEMENT NUMBER
0602201

6. AUTHOR(S)

Prof. Michael A. Sutton
Prof. Xiaomin Deng
Dr. Jianzheng Zuo

5d. PROJECT NUMBER
A02P

5e. TASK NUMBER

5f. WORK UNIT NUMBER
0B

7. PERFORMING ORGANIZATION NAME(S) AND ADDRESS(ES)

University of South Carolina
Department of Mechanical Engineering
Columbia, SC 29208

8. PERFORMING ORGANIZATION REPORT NUMBER

9. SPONSORING/MONITORING AGENCY NAME(S) AND ADDRESS(ES)

Air Vehicles Directorate
Air Force Research Laboratory
Air Force Materiel Command
Wright-Patterson Air Force Base, OH 45433-7542

10. SPONSORING/MONITORING AGENCY ACRONYM(S)
AFRL-VA-WP

11. SPONSORING/MONITORING AGENCY REPORT NUMBER(S)
AFRL-VA-WP-TR-2006-3160

12. DISTRIBUTION/AVAILABILITY STATEMENT
Approved for public release; distribution is unlimited.

13. SUPPLEMENTARY NOTES
Report contains color. PAO Case Number: AFRL/WS 06-1800, 20 Jul 2006.

14. ABSTRACT

This report summarizes work done to develop an analytical method to predict stable tearing crack path and shapes under complex mixed mode loading conditions using large deformation kinematics. A simulation program, CRACK3D, was developed as part of this effort. This report also documents the strategies used to automatically re-mesh finite elements around the crack tip in CRACK3D.

15. SUBJECT TERMS
stable tearing, mixed mode loading, CRACK3D

16. SECURITY CLASSIFICATION OF:			17. LIMITATION OF ABSTRACT:	18. NUMBER OF PAGES	19a. NAME OF RESPONSIBLE PERSON (Monitor)
a. REPORT	b. ABSTRACT	c. THIS PAGE			James A. Harter
Unclassified	Unclassified	Unclassified	SAR	94	19b. TELEPHONE NUMBER *(Include Area Code)* N/A

Standard Form 298 (Rev. 8-98)
Prescribed by ANSI Std. Z39-18

TABLE OF CONTENTS

EXECUTIVE SUMMARY

The broad objectives of this project are to (a) develop a computational methodology for implementing the criterion to predict stable tearing along a general path in three-dimensions and (b) develop and validate a mixed mode fracture criterion using the initial experimental data base and completed computational methodology.

First, a fully functional three-dimensional crack growth algorithm has been developed that is capable of predicting crack growth along a general, three-dimensional surface. The algorithm, designated CRACK3D, utilizes the pre- and post-processing capabilities of ANSYS while performing all of the crack-front calculations internally. The computer code, designated CRACK3D, developed as part of this project is fully capable of handling the kinematics of general crack growth and determining the stress and deformation states during crack growth. In addition, the code can be interfaced with subroutines that implement a broad range of fracture criterion to predict the instant and direction of crack growth. Finally, the simulation of mixed-mode crack growth under three-dimensional (3D) conditions, such as the growth of surface cracks, corner cracks, embedded cracks, and cracks with a curved crack surface and/or a curved crack front has also been fully automated within CRACK3D. Since a major portion of the work performed to finalize CRACK3D involved the development of a remeshing capability in 3D, Part II of this final report discusses the computational aspects of the simulation procedure and associated algorithms implemented for simulating arbitrary 3D crack growth under general loading conditions. In particular, this paper discusses the strategies used for implementing automatic re-meshing of regions around growing crack fronts in a 3D body, along with verification examples.

Second, Section III of this report describes a combined experimental-computational effort using aluminum alloy 2024-T351 that was performed to gain an understanding of slant fracture events and to provide insight for establishing a general fracture criterion. The stable tearing fracture experiments were performed previously under (a) combined tension-torsion (nominal mixed-mode I/III) loading and (b) under nominally Mode I load using Arcan specimens.

Two types of finite element models were considered for the study of slant fracture: (a) combined tension-torsion specimens containing stationary, flat and slant cracks subject to loads corresponding to the onset of crack growth, and (b) stable tearing crack growth with slanting in a nominal Mode I Arcan specimen. Analysis results reveal that there exists a strong correlation between the direction of the maximum effective plastic strain ahead of a crack front and the orientation direction of slant fracture. In particular, it is observed that (a) at the onset of crack growth, the angular position of the maximum effective plastic strain around the crack front serves as a good indicator for the slant fracture surface orientation during subsequent crack growth; and (b) during stable tearing crack growth with a flat-to-slant transition, the crack growth path on each section plane through the thickness of a specimen coincides with the angular position of the maximum effective plastic strain around the crack front. The results of this study suggest that the effective plastic strain may be used as a fracture parameter for predicting the fracture surface path of stable crack growth with slant fracture.

I. INTRODUCTION

As noted by the National Materials Advisory Board, a critical limitation in the state-of-the-art for crack-growth simulation technology is the lack of an experimentally verifiable, general stable tearing criterion that can be applied to the whole spectrum of possible crack-tip loading conditions. This would include plane stress, plane strain and general, three-dimensional conditions.

This program was directed towards (a) developing 3D simulation algorithms that can be used to perform node-by-node stable tearing analyses on aerospace alloys and (b) understanding and developing a reliable fracture criterion for prediction of stable tearing in 3D structures.

II. Computational Aspects and Code Development of Three-dimensional Crack Growth Simulations

Abstract

An important task in mixed-mode fracture analysis and prediction is the simulation of crack growth under mixed-mode conditions. To complete such a task, one must have (a) a computer code capable of handling the kinematics of general crack growth and determining the stress and deformation states during crack growth, and (b) a fracture criterion that can properly predict the instant and direction of crack growth. A current challenge is the simulation of mixed-mode crack growth under three-dimensional (3D) conditions, such as the growth of surface cracks, corner cracks, embedded cracks, and cracks with a curved crack surface and/or a curved crack front.

This section addresses item (a) in the above discussion and describes the computational aspects of a simulation procedure and associated algorithms for simulating arbitrary 3D crack growth under general loading conditions, which have been developed and successfully implemented by the authors in a custom, finite element based, crack growth analysis and simulation code— CRACK3D. In particular, this paper will present strategies for automatic re-meshing of regions around growing crack fronts in a 3D body, and will discuss verification examples.

II.1. Introduction

Residual strength and fatigue lifetime prediction for damaged structures and components has been attracting more and more attention of engineers and scientists [1-5]. In many cases the residual strength and lifetime of such kinds of structures and components is depending on the behavior of flaws in them [6, 7]. Thereby, the accurate prediction of three-dimensional crack propagation in ductile materials plays an important role in the evaluation of residual strength and lifetime of structures and components with cracks [8-10].

Due to the strict requirement on boundary conditions and the geometry of objects, currently the analytical solution is nearly impossible to be obtained in many problems of cracks, especially for the process of ductile crack propagation in three-dimensional structures. Thus, different attempts have been made to develop efficient and robust numerical simulation tools to predict the response of components during the process of crack propagation [11-15].

To develop a general three-dimensional crack growth simulation tool, there are several key issues. Firstly, a three-dimensional fracture criterion is required to be used to determine the onset and the direction of crack growth. A lot of experimental, analytical and numerical studies have been done on this topic [16-20] and the results show that, for different kinds of materials, such as brittle materials and ductile materials, the behavior of failure has more or less difference, especially for mixed-mode fracture. For aluminum alloy 2024-T3, experimental results show that there is a sharp transition of crack growth behavior from predominantly Mode I type to Mode II type during the variation of the amount of mixed mode loading [18]. Clearly, using Stress Intensity Factor (SIF) [8, 12] to predict the direction of crack growth in ductile materials will result in inconsistent results with the experimental results [18].

Secondly, a robust remeshing algorithm is requisite to simulate the crack growth by updating the finite element mesh. As one knows, the geometric topology of structures can be any type during the evolution of crack surfaces. To make the simulation of crack growth run smoothly and automatically, the remeshing algorithm should have the ability to handle any kind of cracks, such as surface cracks, through-thickness cracks and embedded cracks [21]. It is usually required in fracture mechanics that the element size in the region near crack fronts is quite small comparing to the element size in the region far from the crack fronts. However, the crack front may go anywhere and the dense mesh in the previous position of the crack front contributes little to the quantities of fields near the current crack front. If the remeshing scheme can not loose the mesh in the previous position of the crack front, the total number of element will increase significantly as the movement of crack front [5], which causes the size of finite element model and subsequent CUP time-consuming increasing quickly during the process of crack growth.

In this paper, the authors focus on the development of new software, CRACK3D, for three-dimensional crack growth simulation. It addresses the computational aspects of the simulation procedure and associated algorithms used for simulating arbitrary three-dimensional crack propagation under general loading conditions which have been developed and successfully implemented into a custom, finite element based, crack growth simulation code — CRACK3D. The paper is organized as follows. Section 2 introduces the hierarchy of the simulation tool, CRACK3D. Section 3 describes the schemes of modification of geometry and topology after each step of crack growth. Section 4 discusses the issues of cutting a local region from the global model for remeshing. Section 5 gives the approaches of local remeshing and mesh connection between the local regions and the remnant of global model. Section 6 gives the approach used in CRACK3D for data transformation from the previous mesh to the current mesh. Section 7 employs two selected examples to demonstrate the capabilities of CRACK3D in simulating three-dimensional crack growth. Section 8 presents the conclusions of the work.

II.2. Hierarchy of the software CRACK3D

Crack growth simulation is a combined incremental process including increasing or decreasing loads and incrementally variation of the size of crack surface, which is more complicated than many other numerical applications in computational mechanics in the aspects of the structure of program and the management of database. To take the

advantage of the existing pre- and post-processing capabilities of general commercial software, such as ANSYS, current version of CRACK3D was developed to focus on the three-dimensional crack growth simulation. During the whole process of crack growth simulation, CRACK3D has no data-exchange with third-party software. The third-party software has nothing to do with the analysis of mechanics except providing initial mesh and visualization of results. Fig. 1 shows the relation of CRACK3D with commercial software ANSYS.

CRACK3D is a package of three-dimensional crack propagation simulation, which was developed modularly. Generally speaking, CRACK3D consists of four modules, stress analysis, determination of new crack front, modification of geometry and topology and local remeshing. These modules are locally independent and invoked successively during the simulation of crack growth, as shown in Fig. 2.

It has been widely accepted that the macroscopic fracture criteria are dependent on the behavior and properties of materials, such as brittle and ductile materials. For the consideration of the implementation of different fracture criteria into CRACK3D in the future, a user subroutine interface is provided for users to implement their own fracture criteria into CRACK3D. From Fig. 2, one can find that fracture criteria will work on the base of the stress and strain results provided by the module “STRESS ANALYSIS”; it will provide information necessary for determining the location of new crack fronts and the shape of new crack surfaces in the module “NEW CRACK FRONT”. Another use of the user subroutine interface of fracture criteria is that, users can take the advantage in studying or verifying new fracture criteria for different materials.

The module “GEOMETRY & TOPOLOGY MODIFICATION” utilizes the information of new crack front and new crack surfaces to modify the configuration of the structure under consideration, including its geometry and topology, and creates a reasonable geometric model with the combination of new crack surfaces. The module “LOCAL REMESHING” will generate a new mesh around the new crack front and convert the numerical results from previous mesh to current mesh so that the model “STRESS ANALYSIS” can accept the data of the new mesh and automatically continue the simulation.

It need mention that, even though the remeshing tool is available in current version of CRACK3D, the initial mesh is required for user to input, which can also be generated by a third-party software. Once the initial mesh data and controlling parameters are provided, CRACK3D can automatically perform fracture analysis, modification of geometry and topology, remeshing and data transformation in sequence without user’s interference during the whole process of crack growth simulation.

II.3. Modification of geometry and topology

To simulate the crack growth in three-dimensional structures, a fracture criterion is requisite to determine the onset and direction of crack propagation at each node along the current crack front. The distance of crack extension at different nodes may be assumed to be proportional to the magnitude of driving force at the corresponding node. By utilizing the direction and the length of crack growth at each node along crack front, one can straightforwardly obtain the coordinates of the location of new crack front.

It is apparent that the new crack front determined by the direction and length of crack extension is a virtual crack front, which needs some modification so that it

becomes the real crack front. Fig. 3 illustrates some kinds of the modifications to the virtual crack front for a plate with a through-thickness crack. In most cases, for instance, some parts of the virtual crack front may go outside the material, especially for a curvilinear crack front. Firstly, the module "GEOMETRY & TOPOLOGY MODIFICATION" determines the real crack front by making use of the virtual crack front and geometric information of the boundary surfaces of the structure. Secondly, it performs the geometric Boolean calculation by utilizing the virtual new crack surfaces to determine the new topology of the structure, and subsequent new boundary lines, new boundary surfaces. Thirdly, some of the existing boundary surfaces and boundary lines also need to be updated by the module to reflect the change of geometry induced by the crack propagation.

In order to generate and provide a reasonable geometric model for the purpose of remeshing, some criteria are used during the modification. For example, for a through-thickness crack as shown in Fig. 3, if the predicted location of any end of the crack front is too close to any one of the surfaces of the structure (see Fig. 3d) the ill-shaped elements will be generated in the vicinity of the end of crack front during remeshing. To solve this problem, a straightforward method is to move the predicted location of the end of crack front onto the closest surface to it. In CRACK3D, a tolerance less than or equal to one fourth of the minimum element size is used to determine if the movement is necessary. Generally speaking, to avoid the occurrence of ill-shaped elements, the modification to the virtual crack front should result in a real crack front which satisfies

1. *There is no node on the crack front whose distance to its closest boundary surface is less than the specified tolerance and greater than zero.*
2. *The length of any one of crack fronts is greater than the minimum element size.*
3. *For surface cracks and through-thickness cracks, there is no end of the crack fronts whose distance to its closest boundary line is less than the specified tolerance and greater than zero.*
4. *For each crack front, the number of nodes on the crack front whose distance to its corresponding closest boundary surface is equal to zero can only be equal to zero or two.*

Once the locations of crack fronts have been determined, the module "GEOMETRY & TOPOLOGY MODIFICATION" is to perform the geometric Boolean calculation by utilizing the virtual new crack surfaces to determine the new topology of the structure, and subsequent new boundary lines, new boundary surfaces. To reduce the possibility of generating ill-shaped elements during the process of remeshing, the resulting geometric model should also satisfy

1. *There is no boundary line whose length is less than the minimum element size.*
2. *There is no boundary surface whose area is equal to zero.*
3. *The area of any separated cross-section cut by any oriented plane is greater than a specified tolerance.*
4. *Any segment of boundary lines must be shared and can only be shared by two boundary surfaces.*

II.4. Determination of local region

To take into account the effect of geometric change induced by crack propagation on the finite element model, CRACK3D has the capacity to specify a certain region by making use of the user-inputted parameter controlling the size of a local region and remesh it. A straightforward way is to investigate each element to see if the minimum distance of its centroid to any node on the new crack front is less than the given distance specified by users. A local region will be formed by collecting all the elements lying within the distance. The specific approach is given in the following

1. *Find out the geometric topology of region Ω on the base of the current mesh. Suppose S_Ω is the set of all boundary surfaces of Ω, L_Ω is the set of all boundary lines of all boundary surfaces of Ω*

$$S_\Omega = \{S_i,\ S_i \in \Omega\}$$
$$L_\Omega = \{l_i,\ l_i \in \Omega\}$$

2. *Determine Ω_k (k=1, 2, … n), which is a local region around the k[th] crack front, the size of Ω_k is controlled by the parameter R, where n is the total number of crack fronts in the structure.*
3. *Determine Λ_R, which is the remnant of region Ω subtracted with Ω_k (k=1, 2, … n), thus*

$$\Omega = \Lambda_R \cup \Omega_1 \cup \Omega_2 \cup \ldots \cup \Omega_n$$

4. *Find out the geometric topology of region Λ_R based on the current mesh and the sets of L_Ω and S_Ω. Suppose S_Λ is the set of all boundary surfaces of Λ_R, L_Λ is the set of all boundary lines of Λ_R*

$$S_\Lambda = \{S_i,\ S_i \in \Lambda_R\}$$
$$L_\Lambda = \{l_i,\ l_i \in \Lambda_R\}$$

5. *Investigate the relationship of all the local regions Ω_k (k=1, 2, … n). Check if one of them intersects with another. If yes, then combine those local regions intersected mutually to form a larger new local region. Suppose there are m local regions $\Re_k$ (k=1, 2, … m) constructed after the combination among the set of Ω_i (i=1, 2, …n), accordingly*

$$\Omega = \Lambda_R \cup \Re_1 \cup \Re_2 \cup \ldots \cup \Re_m$$

In most cases, the local region formed in the above approach is acceptable and can be put back into global model after remeshing. We also experienced difficulties in some cases that the new mesh of the local region formed in this way after remeshing did not match the previous mesh outside the local region on the interface. By studying the findings we found that the modification to the local region determined in the above method became requisite so that the local region after modification should meet the following conditions

5. *There is no segment of any global boundary lines in the local region $\Re_k$ (k=1, 2, … m) which is shared by the boundary line in the remnant Λ_R*
6. *For any one of local regions $\Re_k$ (k=1, 2, …m), there is no segment of the local boundary lines which is shared by more than two local boundary surfaces in the local region $\Re_k$ (k=1, 2, … m).*

It needs to be mentioned that, after each modification, the evaluation of the relationship among all the local regions and the geometric features of each local region should be performed again until no modification is needed and all the local regions satisfy the above conditions.

Clearly, if the user-inputted parameter controlling the size of a local region is large enough to let all the elements lie inside the local region, then the local region is actually equal to the whole global region, and all the above requirements on the local region will be met automatically. It will simplify the determination of local region, but the time consumed during the process of remeshing and data transformation from previous mesh to new mesh will increase significantly.

II.5. Remeshing on the specified local region

Once the local regions have been determined, the module “LOCAL REMESHING” will be invoked to re-mesh the local region one by one and perform the data transformation from previous mesh to the new generated mesh.

As one can understands, any kind of geometry shapes and topologies has the possibility of occurrence during the process of crack propagation that makes remeshing around crack fronts more difficult than many other kinds of remeshing in a region without cracks, and the robustness of the remeshing tool usually turn to decrease. To develop a robust remeshing tool for arbitrary three-dimensional structures with cracks, two features of the regions with cracks require the most attention. One feature arises due to the geometric coincidence of two crack surfaces. When this occurs, two nodes on separate fracture surfaces may occupy the same spatial position. Since there are two candidate nodes at the same spatial position, simple geometric arguments are not sufficient to identify the appropriate node for inclusion in a new element’s definition during the meshing (re-meshing) process. The second feature is introduced when there is inter-penetration of two crack surfaces, a common occurrence during the meshing (re-meshing) of curved crack surfaces that results in the intersection of volume elements in the region adjacent to curved crack surfaces.

There are three kinds of basic cracks in three-dimensional structures, surface cracks, through-thickness cracks and embedded cracks, which result in different kinds of geometric topologies. The module “LOCAL REMESHING” in CRACK3D was developed based on the mesh generation algorithm given in [21] and took into consideration all the features of the three kinds of cracks. Figs 4-6 show the resulting meshes of domains containing different kinds of cracks. From the resulting meshes, it can be found that the element quality around any kind of crack fronts is acceptable.

As mentioned in section 4, if a local region is to be remeshed then it will become more complicate than remeshing the global region since there exists a necessary

requirement during the local remeshing. It is clear that, since only parts of the global region undergoes remeshing, the mesh consistency on the interface between the local regions and the remnant of the global region obtained by subtracting the local regions should be satisfied so that the local regions after remeshing can be put back and connected to the previous mesh around the local regions without any gap and/or penetration. This process can be illustrated in Fig. 7.

To assure the consistency of mesh on the interface between local regions and the remnant of the global region, it needs to identify the local boundary lines and local boundary surfaces which need to be remeshed, and those which should not be remeshed so that the profile of the local mesh on the interface keep consistent with that of the remnant mesh. To achieve this goal, the following approach is suggested

1. *For a given global region* Ω, *denote* S_Ω *the set of all boundary surfaces of* Ω, L_Ω *the set of all boundary lines of all boundary surfaces of* Ω

$$S_\Omega = \{S_i,\ S_i \in \Omega\}$$
$$L_\Omega = \{l_i,\ l_i \in \Omega\}$$

2. *For any one of local regions,* $\Re_k$ *(k=1, 2, … m), denote* $S_{\Re_k}$ *the set of all local boundary surfaces of the local region* $\Re_k$, $L_{\Re_k}$ *the set of all local boundary lines of the local region* $\Re_k$,

$$S_{\Re_k} = \{S_i,\ S_i \in \Re_k\} \qquad (k=1, 2, \ldots m)$$
$$L_{\Re_k} = \{l_i,\ l_i \in \Re_k\} \qquad (k=1, 2, \ldots m)$$

3. *Denote* Λ_R *the remnant of the global region* Ω *subtracted with* $\Re_k$ *(k=1, 2, … m), which satisfies*

$$\Omega = \Lambda_R \cup \Re_1 \cup \Re_2 \cup \ldots \cup \Re_k$$

4. *Evaluate the geometric topology of the remnant region,* Λ_R. *Suppose* S_Λ *is the set of all boundary surfaces of* Λ_R, L_Λ *is the set of all boundary lines of all boundary surfaces of* Λ_R

$$S_\Lambda = \{S_i,\ S_i \in \Lambda_R\}$$
$$L_\Lambda = \{l_i,\ l_i \in \Lambda_R\}$$

5. *Evaluate the relationship between* S_Λ *and* $S_{\Re_k}$ *(k=1, 2, … m), and the relationship between* L_Λ *and* $L_{\Re_k}$ *(k=1, 2, … m). Denote* S_C *the common part of* S_Λ *and* $S_{\Re_k}$ *(k=1, 2, … m),* L_C *the common part of* L_Λ *and* $L_{\Re_k}$ *(k=1, 2, … m)*

$$S_C = S_\Lambda \cap S_{\Re_1} \cap S_{\Re_2} \cap \ldots \cap S_{\Re_k}$$
$$L_C = L_\Lambda \cap L_{\Re_1} \cap L_{\Re_2} \cap \ldots \cap L_{\Re_k}$$

6. *For any one of local regions,* $\Re_k$ *(k=1, 2, … m), decompose* $S_{\Re_k}$ *and* $L_{\Re_k}$ *into two parts,* $S^1_{R_k}$ *and* $S^2_{R_k}$, $L^1_{R_k}$ *and* $L^2_{R_k}$, *respectively, which yield to the following relations*

$S_{\Re_k} = S^1_{R_k} \bigcup S^2_{R_k}$, $S^1_{R_k} \notin S_C$, $S^2_{R_k} \in S_C$, *(k=1, 2, … m)*

$L_{\Re_k} = L^1_{R_k} \bigcup L^2_{R_k}$, $L^1_{R_k} \notin L_C$, $L^2_{R_k} \in L_C$, *(k=1, 2, … m)*

7. *For the local region $\Re_k$ (k=1, 2, … m), remesh the boundary lines in $L^1_{R_k}$ and the boundary surfaces in $S^1_{R_k}$, while the mesh on the boundary lines in $L^2_{R_k}$ and on the boundary surfaces in $S^2_{R_k}$ keep the original. After all the mesh on the boundary lines and the boundary surfaces of the local region $\Re_k$ is determined, the volume mesh can be generated in the local region, $\Re_k$.*

After remeshing in each local region, the techniques of mesh optimization are employed in the module "LOCAL REMESHING" to optimize the distribution and quality of elements around the crack fronts. Since the gradient of element size in the region near crack fronts is severe, the resulting meshes after mesh optimization also show that the transition of element size gets significant improvement in such regions.

II.6. Data mapping from previous mesh to current mesh

For the incremental elastic-plastic stress analysis, the numerical calculation in time step t_N is based on the numerical results in time step t_{N-1}. To simulate the crack propagation automatically after remeshing without interruption due to the evolution of finite element model induced by crack growth, the previous results, such as displacement, strain and stress, need to be mapped from the previous mesh to the current mesh so that the subsequent computation based on the current mesh has valid and continuous results.

Currently there are two types of elements used in CRACK3D for the three-dimensional simulation of crack propagation with local remeshing, 4-noded tetrahedral element and 10-noded tetrahedral element. Hereinafter we will employ the 4-noded tetrahedral elements to demonstrate the approach used in CRACK3D for the data transformation between two adjacent mesh frames.

II.7. Locate a new node in the previous mesh frame

Suppose (x_0, y_0, z_0) is the coordinates of a given point *P* in the current mesh frame, which may be either a new nodal point or a Gaussian integration point of a new element in the current finite element mesh, we need search an element first in the previous mesh which contains the given point *P*.

For an arbitrary element, say E_P, in the previous mesh, without loss of generality, suppose N_1, N_2, N_3 and N_4 are the four nodes of the element E_P, as shown in Fig. 8. One can calculate the volumes of the four tetrahedrons $PN_2N_3N_4$, $PN_3N_1N_4$, $PN_1N_2N_4$ and $PN_1N_3N_2$ by evaluating the following determinants

$$V_1 = \frac{1}{6}\begin{vmatrix} x_2 - x_0 & y_2 - y_0 & z_2 - z_0 \\ x_3 - x_0 & y_3 - y_0 & z_3 - z_0 \\ x_4 - x_0 & y_4 - y_0 & z_4 - z_0 \end{vmatrix} \qquad \text{(1a)}$$

$$V_2 = \frac{1}{6}\begin{vmatrix} x_3 - x_0 & y_3 - y_0 & z_3 - z_0 \\ x_1 - x_0 & y_1 - y_0 & z_1 - z_0 \\ x_4 - x_0 & y_4 - y_0 & z_4 - z_0 \end{vmatrix} \quad (1b)$$

$$V_3 = \frac{1}{6}\begin{vmatrix} x_1 - x_0 & y_1 - y_0 & z_1 - z_0 \\ x_2 - x_0 & y_2 - y_0 & z_2 - z_0 \\ x_4 - x_0 & y_4 - y_0 & z_4 - z_0 \end{vmatrix} \quad (1c)$$

$$V_4 = \frac{1}{6}\begin{vmatrix} x_1 - x_0 & y_1 - y_0 & z_1 - z_0 \\ x_3 - x_0 & y_3 - y_0 & z_3 - z_0 \\ x_2 - x_0 & y_2 - y_0 & z_2 - z_0 \end{vmatrix} \quad (1d)$$

where (x_i, y_i, z_i) (i=1, 2, 3, 4) are the coordinates of nodes N_1, N_2, N_3 and N_4. By utilizing the magnitudes of V_1, V_2, V_3, and V_4, one can draw a conclusion whether or not the given point P is inside the element E_P. If none of the volumes V_1, V_2, V_3, and V_4 is less than zero, then the element E_P contains the given point P, otherwise it doesn't contain the given point P.

To speed up the search process in CRACK3D, only the elements of the previous mesh inside the local region are chosen to be the candidates.

II.8. Evaluate the field quantities for a specified point

Once the element in the previous mesh containing the point in the current mesh has been found, a straightforward approach is used to evaluate all the field quantities such as displacement, strain and stress, at the new point in the current mesh.

For a given new point P in the current mesh, suppose the element E_P in the previous mesh contain the given point P. Then one can evaluate the field quantities at the point P by employing the field quantities of element E_P in the frame of previous mesh. For any specific field quantity at point P, F_P, it can be interpolated by making use of the shape function of the 4-noded tetrahedral element with respect to the location of point P.

The shape function of the 4-noded tetrahedral element with respect to the coordinates of point P can be expressed as

$$\Phi_1 = V_1 / V_E, \quad \Phi_2 = V_2 / V_E, \quad \Phi_3 = V_3 / V_E, \quad \Phi_4 = V_4 / V_E,$$

where $V_E = V_1 + V_2 + V_3 + V_4$. Accordingly, the field quantity at point P, F_P, can be interpolated in the following

$$F_P^k = \sum_{i=1}^{4} \Phi_i F_i^{k-1}$$

where F_P^k is the quantity at the point P in mesh k, F_i^{k-1} is the quantity at node i of element E_P in mesh k-1.

II.9. Geometry and Topology Changes due to Crack Evolution

The module "GEOMETRY & TOPOLOGY MODIFICATION" in CRACK3D can handle geometric and topological changes due to several common types of crack evolution (e.g. from an embedded crack to a surface crack to a through-thickness crack) due to intersections of growing cracks with surfaces, as shown in Figure 9. In addition, some special features of 3D crack growth observed in many real applications are also addressed in CRACK3D, such as the disappearance of a crack front due to local separation of a structure, corner cracks, and cracks passing structural stiffeners. Figure 10 shows the schematics of some of the features implemented in CRACK3D.

II.10. Examples

In this section two selected examples are used to demonstrate the reliability and capability of CRACK3D in the application of simulating crack growth in three-dimensional components. In these two examples, the effects of crack tunneling and slanting on fracture toughness are not taken into consideration. During the process of crack growth, the crack front was assumed to be a straight line. Thus, the Mixed-Mode CTOD fracture criterion [5] could be employed in the simulations.

During the simulations, the direction of crack growth was determined by the Mixed-Mode CTOD fracture criterion [5] and the onset of crack growth was determined by the critical CTOD of aluminum on the surface of specimens. When the CTOD at the distance of 1 mm behind the crack front on the surface of the specimen reaches the critical value δ_c =0.08 mm, then the whole crack front extends 0.8mm in the predicted direction of crack growth.

Simulation of crack growth in a plate

The geometry of the plate with a single edge crack is shown in Fig. 11. The plate is made of aluminum alloy 2024-T3, and the thickness of the plate is 2 mm. The material properties of aluminum alloy 2024-T3 are as follows. Young's modulus E = 71.2*GPa*, Poisson's ratio v = 0.3, initial yield stress σ_y = 358 *MPa*. The strain hardening curve of 2024-T3 is shown in Fig. 12.

The plate underwent the Mode I displacement loading, as shown in Fig. 13. The 4-noded tetrahedral elements were used in the finite element model. In the initial mesh, there were 5974 elements and 2155 nodes. The deformed mesh and predicted crack path are shown in Fig. 14. It can be seen from Fig. 14 that, during the process of crack growth, the mesh in a local region around the crack front is automatically updated as the crack propagates, and the element density of the mesh in all the previous locations of crack fronts is also updated during remeshing so that the total number of elements in the finite element model can be controlled to vary only in a small range. Fig. 15 shows the variation of the number of elements versus crack extension during the process of crack propagation.

Simulation of crack growth in Arcan specimen

The Arcan test specimen and the loading fixture (composed of a pair grips) are shown in Fig. 16. The fixture is made of 15-5PH stainless steel and has a thickness of

12.6 mm. The specimen is made of aluminum alloy 2024-T3 and has a thickness of 2.3 mm. An edge crack is introduced in the mid-section of the specimen. The initial crack front is fabricated by the fatigue loading. The specimen is then attached to the fixture by three hardened-steel pins at each end. The material properties of 15-5PH stainless steel are as follows. Young's modulus E = 207GPa, Poisson's ratio v = 0.3, initial yield stress σ_y = 1722MPa.

By changing the angle of loading direction in the fixture, different local mode-mixity can be obtained. In this section, only the case of 15 degree loading is provided, as shown in Fig. 17. Considering that the fixture and pins are relatively rigid compared to the specimen, the connection between the fixture and specimen in the finite element model can be assumed to be a rigid and continuous joint. In this simulation (see Fig. 17), 10-noded tetrahedral elements are employed, and there are 4571 elements and 8688 nodes in the initial mesh. Also the Mixed-Mode CTOD fracture criterion [5] is employed in the simulation to predict the onset and direction of crack propagation.

The profiles of deformed meshes at different loading steps are shown in Fig. 16. The comparison of predicted crack path to the experimentally measured crack path is given in Fig. 18. Fig. 19 shows the predicted load versus crack extension by CRACK3D. It is shown in Fig. 19 that there is a good agreement between the numerical results and experimental results.

II.11. Conclusions

A finite element based, crack growth analysis and simulation code— CRACK3D was presented. The hierarchy of the code and some key issues related to the code development and computational aspects of three-dimensional crack growth simulation were given. In the presented program — CRACK3D, the remeshing technology is used to simulate the process of three-dimensional crack growth in any direction predicted by the fracture criteria. From the selected verification examples, it is shown that CRACK3D is reliable and robust. In addition to being used to simulate crack propagation in three-dimensional structures and components, it can also be used to develop and verify new fracture criteria for brittle and ductile materials.

II.12. References

[1] Newman, J.C. Jr., Dawicke, D.S. and Seshadri, B.R., Residual strength analyses of stiffened and un-stiffened panels—Part I: laboratory specimens. *Engineering Fracture Mechanics*, 70(3), 493-507, 2003.

[2] Zuo, J., Kermanidis, Al. Th. and Pantelakis, Sp. G., Strain energy density prediction of fatigue crack growth from hole of aging aircraft structures, *Theoretical and Applied Fracture Mechanics*, 38(1), 37-51, 2002.

[3] McDowell, D.L., An engineering model for propagation of small cracks in fatigue, *Engineering Fracture Mechanics*, 56(3), 357-377, 1997.

[4] Deng, X. and Newman, J.C. Jr., A study of some issues in stable tearing crack growth simulations, *Engineering Fracture Mechanics*, 64(3), 291-304, 1999.

[5] Sutton, M.A., Deng, X., Ma, F., Newman, J.C. Jr. and James, M., Development and application of a crack tip opening displacement-based mixed mode fracture criterion, *International Journal of Solids and Structures*, 37(26), 3591-3618, 2000.

[6] Hwang, C. G. and A. R. Ingraffea, A.R., Shape prediction and stability analysis of Mode-I planar cracks. *Engineering Fracture Mechanics*, 71(12), 1751-1777, 2004.
[7] Dyskin, A.V., Sahouryeh, E., Jewell, R.J., Joer, H. and Ustinov, K.B., Influence of shape and locations of initial 3-D cracks on their growth in uniaxial compression. *Engineering Fracture Mechanics*, 70(15), 2115-2136, 2003.
[8] Riddell W.T., Ingraffea A.R. and Wawrzynek P.A. Experimental observations and numerical predictions of three-dimensional fatigue crack propagation. *Engineering Fracture Mechanics*, 58(4), 293-310, 1997.
[9] Gullerud, A.S., Dodds, R.H. Jr., Hampton, R.W. and Dawicke, D.S., Three-dimensional modeling of ductile crack growth in thin sheet metals: computational aspects and validation. *Engineering Fracture Mechanics*, 63(4), 347-374, 1999.
[10] O'Donoghue, R.E, Atluri, S.N. and Pipkins, D.S., Computational strategies for fatigue crack growth in three dimensions with application to aircraft components. *Engineering Fracture Mechanics*, 52(1), 51-64, 1995.
[11] Deng, X. and Newman, J.C. Jr., ZIP2DL — an elastic-plastic, large-rotation finite element stress analysis and crack growth simulation program. *NASA Langley Research Center* (NASA Technical Memorandum 110332), 1997.
[12] Nishioka T., Tokudome H. and Kinoshita M. Dynamic fracture-path prediction in impact fracture phenomena using moving finite element method based on Delaunay automatic mesh generation. *International Journal of Solids and Structures*, 38(31), 5273-5301, 2001.
[13] FRANC3D Version 2.6, Concepts/Users Guide. Cornell University, New York, 2003.
[14] WARP3D, Release 13.15, University of Illinois, Urbana, Illinois, 2002.
[15] Schollmann M., Fulland M. and Richard H.A. Development of new software for adaptive crack growth simulations in 3D structures. *Engineering Fracture Mechanics*, 70(2), 249-268, 2003.
[16] Sih, G.C., Introductory chapter: a special theory of crack propagation. *Mechanics of Fracture,* Vol. 1, Noordhoof, Holland, pp.XXI-XLV, 1972.
[17] Ma, F., Deng, X., Sutton, M.A. and Newman, J.C. Jr., A CTOD-based mixed-mode fracture criterion. *Mixed-Mode Crack Behavior* ASTM STP 1359, 86-110, 1999.
[18] Amstutz, B.E., Sutton, M.A., Dawicke, D.S. and Newman, J.C. Jr., An experimental study of CTOD for mode I/II stable crack growth in thin 2024-T3 aluminum specimens. *Fracture mechanics* ASTM STP 1256, 256-271, 1995.
[19] Sutton, M.A., Helm, J.D. and Boone, M.L., Experimental study of crack growth in thin sheet 2024-T3 aluminum under tension-torsion loading. *International Journal of Fracture*, 109(3), 285-301, 2001.
[20] Schollmann M., Richard H.A Kullmer, G and Fulland M., A new criterion for the prediction of crack development in multi-axially loaded structures. *International Journal of Fracture*, 117(2), 129-141, 2002.
[21] Zuo, J., Deng, X. and Sutton, M.A., Advances in tetrahedral mesh generation for modeling of three-dimensional regions with complex, curvilinear crack shapes. Submitted for publication.

II.12. Figures

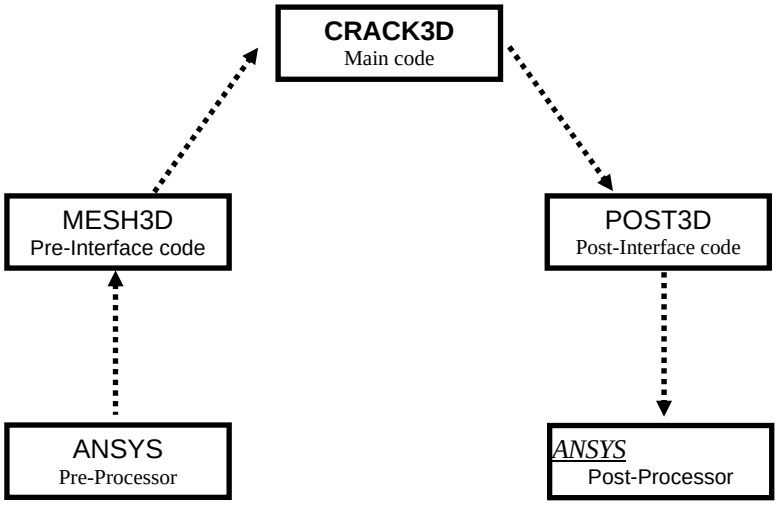

Figure 1. Relation of CRACK3D with ANSYS in the simulation

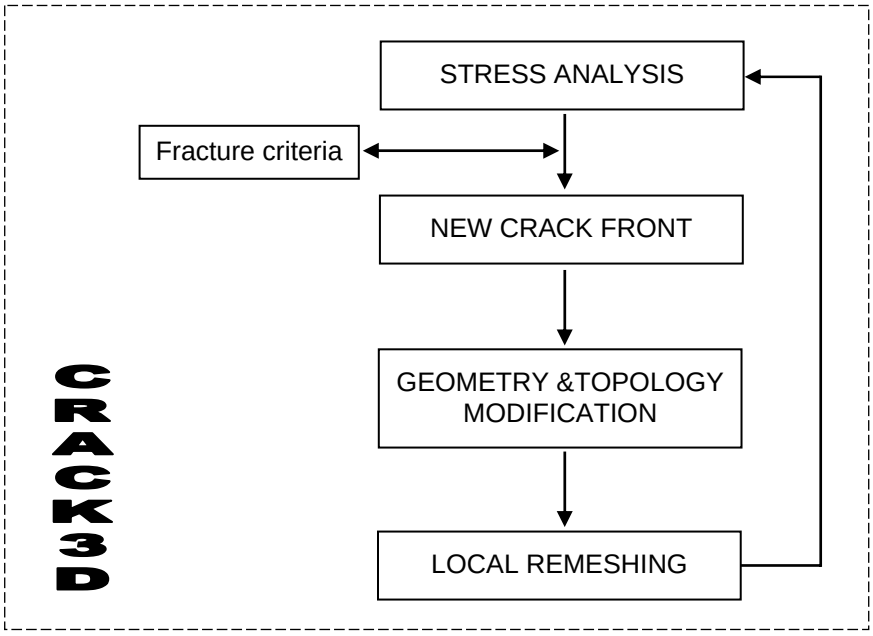

Figure 2. Hierarchy of crack growth simulation code CRACK3D

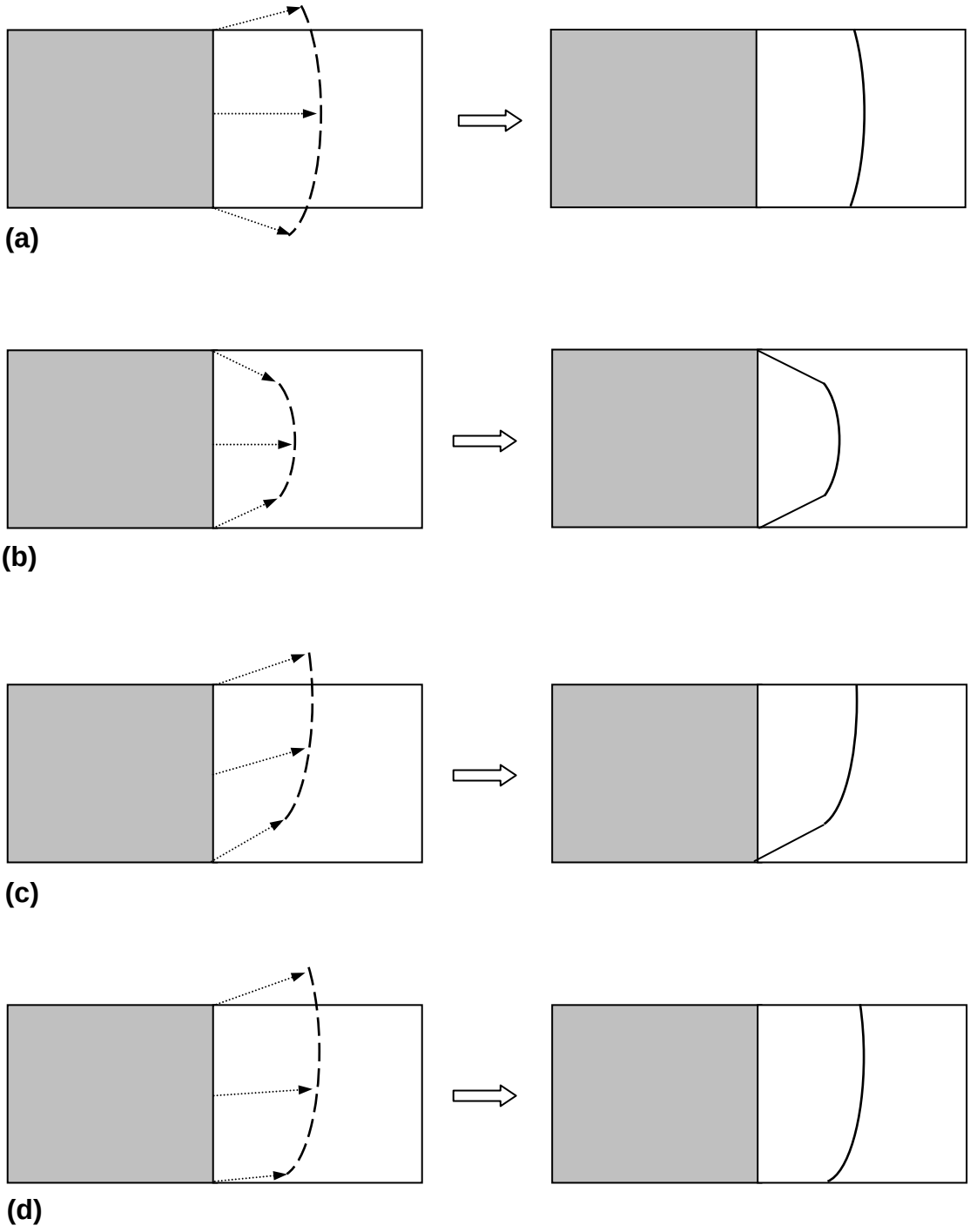

Figure 3. Schematic of crack front determination in a plate with an edge crack

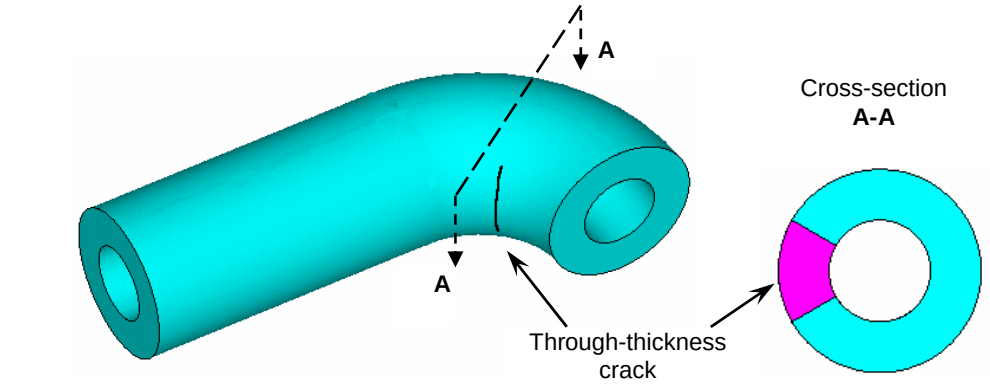

(a)

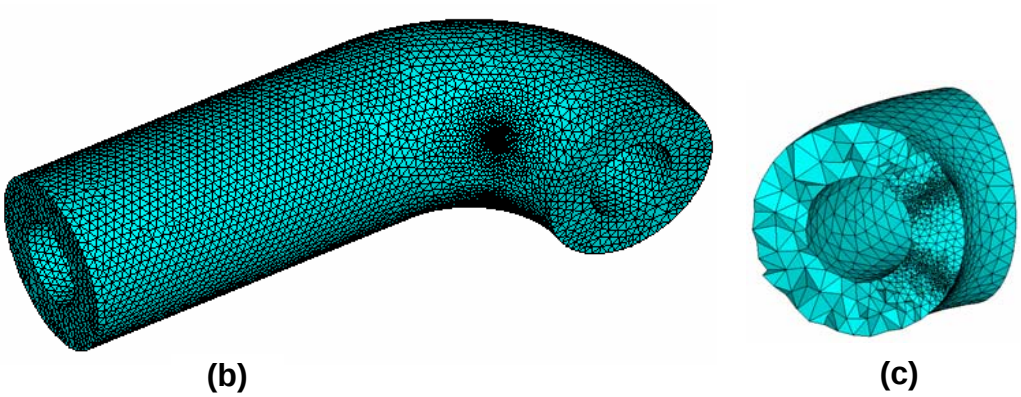

(b) **(c)**

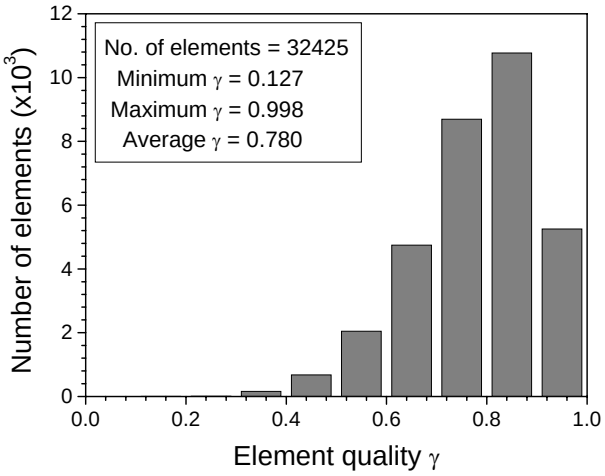

(d)

Figure 4. 3D mesh of a 90^0-elbow pipe with a through-thickness crack: (a) pipe geometry and crack location; (b) an overall view of the mesh; (c) a cross-sectional view along the crack surface; and (d) mesh quality distribution.

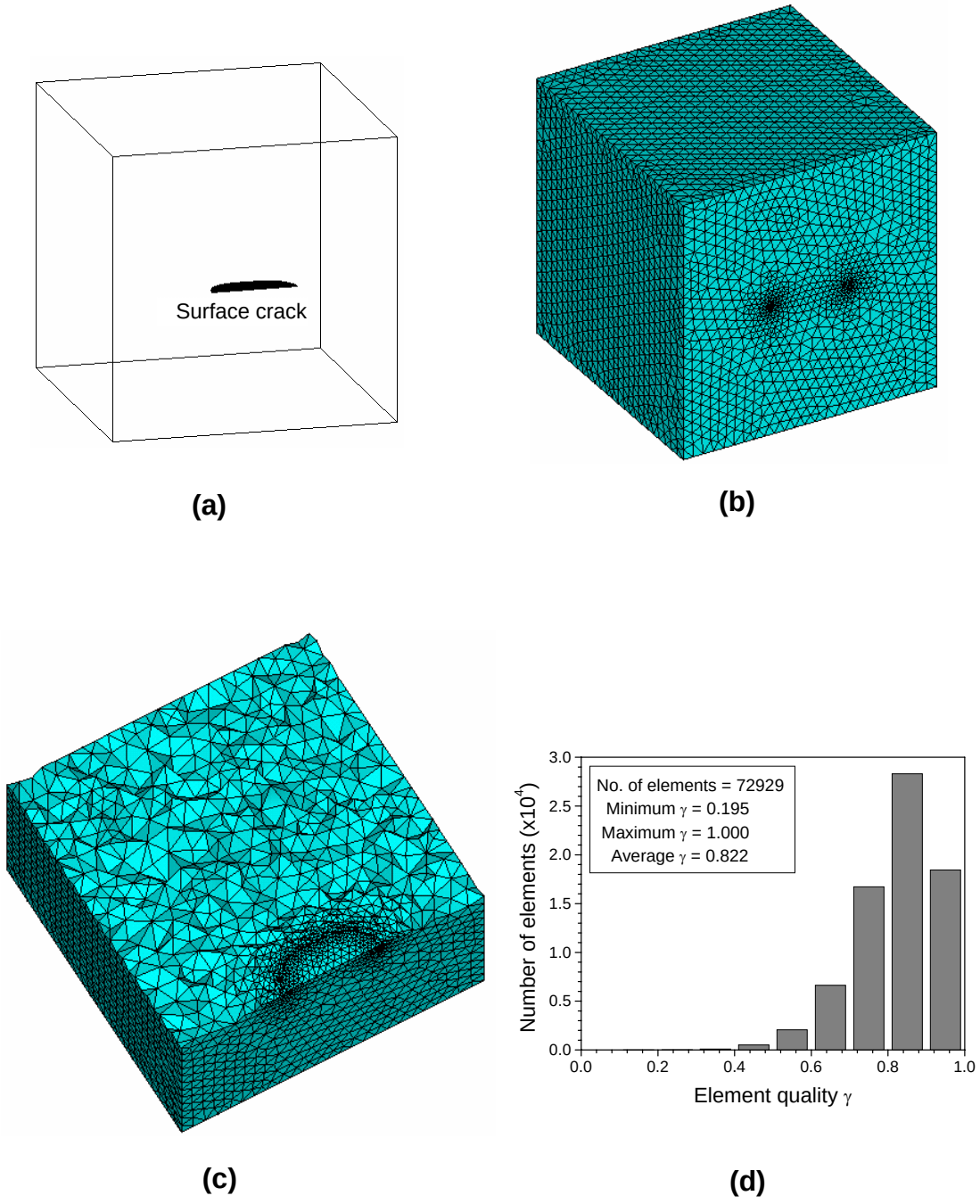

Figure. 5. 3D mesh of a cube with a semi-elliptical surface crack: (a) cube geometry and crack location; (b) an overall view of the mesh; (c) a cross-sectional view along the crack surface; and (d) mesh quality distribution.

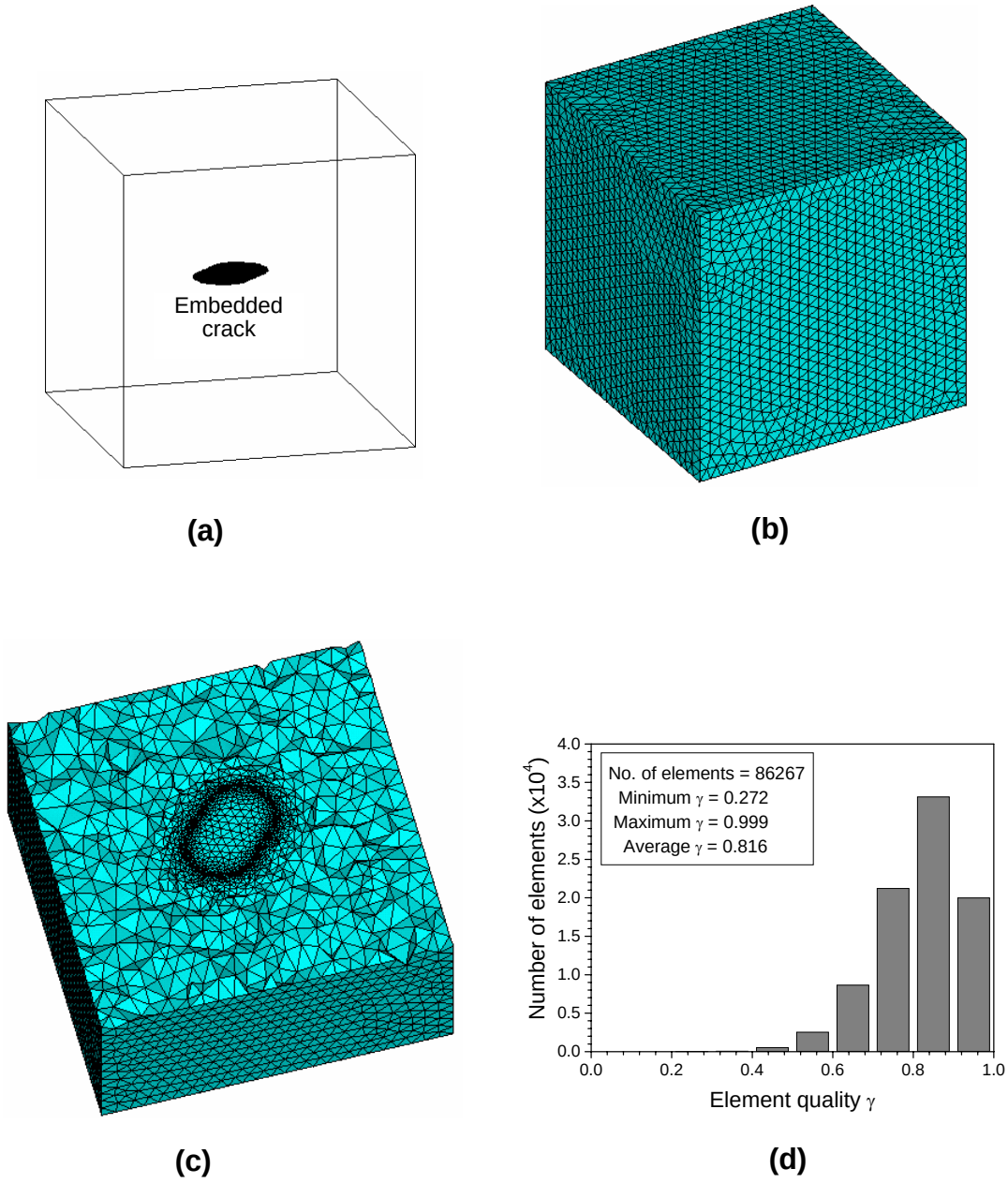

Figure. 6. 3D mesh of a cube with an embedded elliptical crack: (a) geometry and crack location; (b) an overall view of the mesh; (c) a cross-sectional view along the crack surface; and (d) mesh quality distribution.

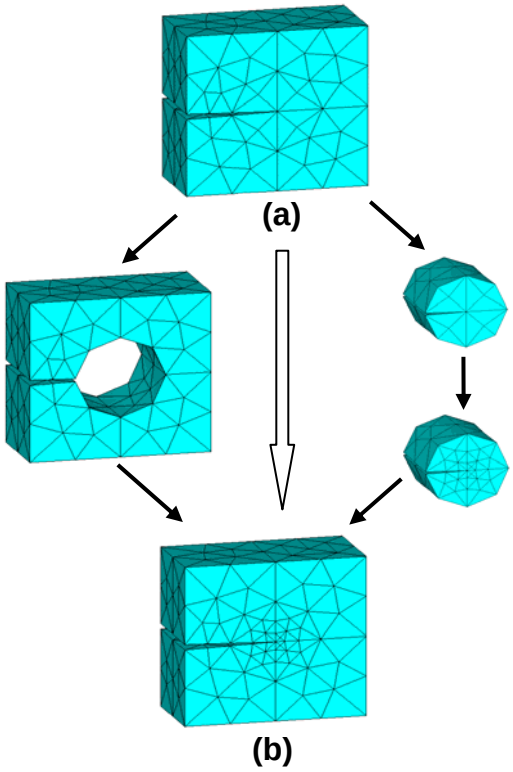

Figure 7. A schematic oflocal remeshing in CRACK3D, (a) mesh before local remeshing; (b) mesh after local remeshing

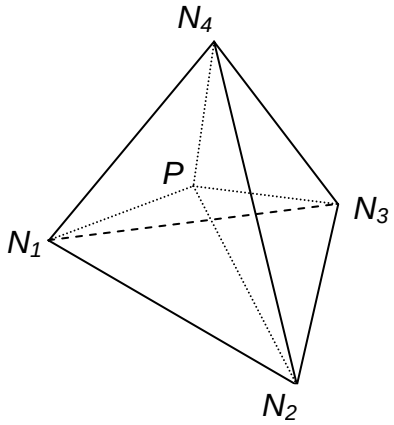

Figure 8. A new point P in the element E_P of the previous mesh

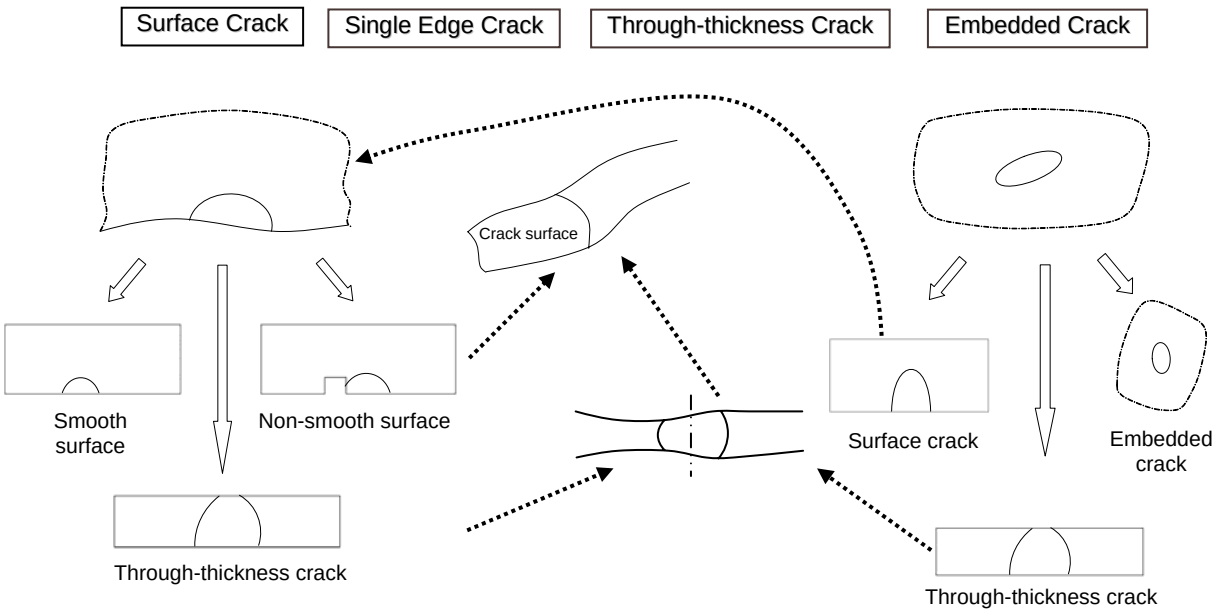

Figure 9: Evolution of flaw shapes

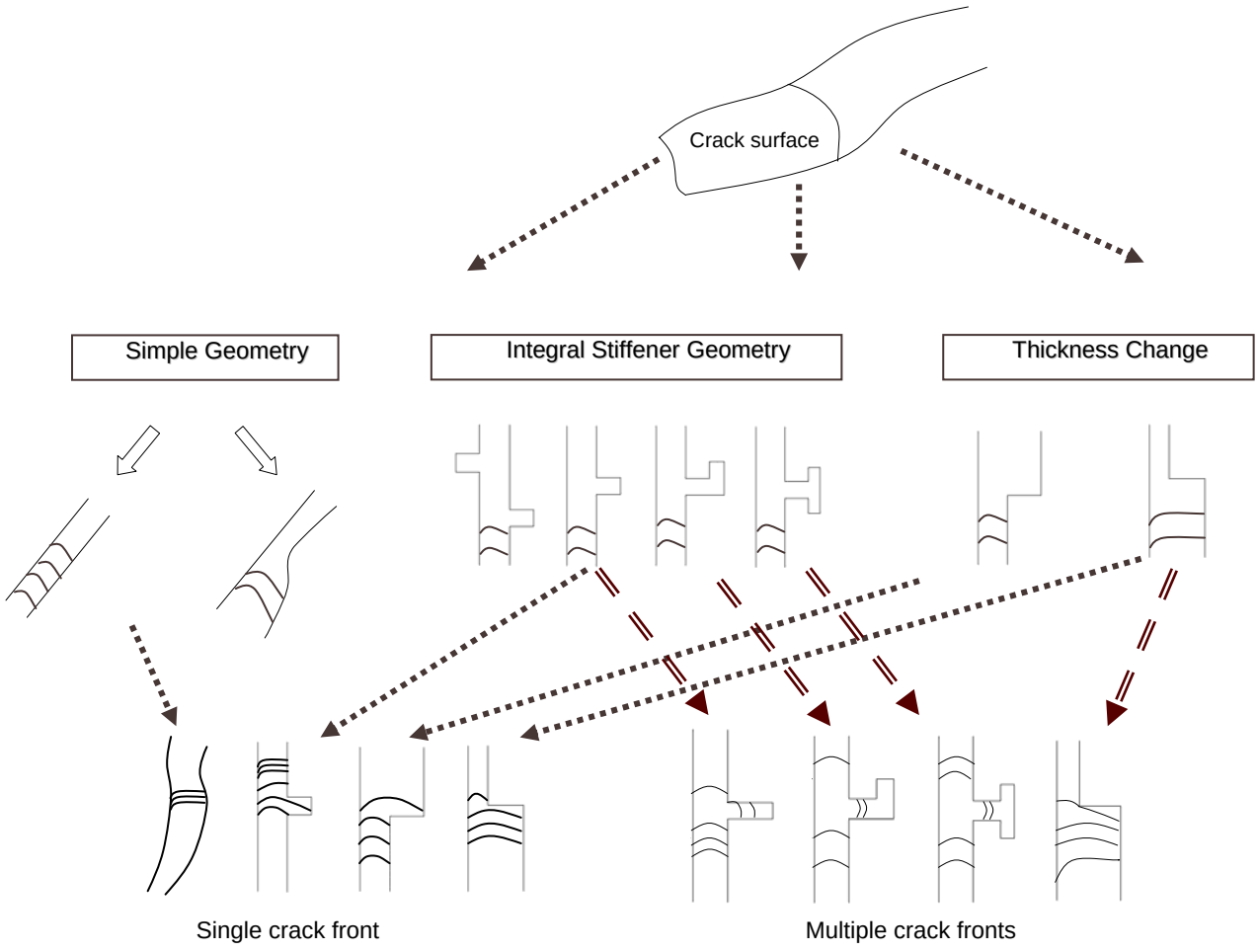

Figure 10: Additional features during flaw evolution

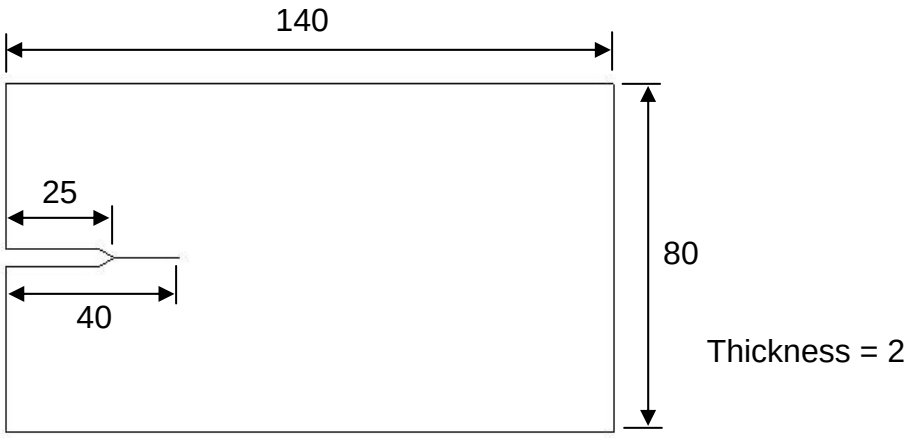

Figure 11. Dimensions of a plate with a single edge crack (Unit: mm)

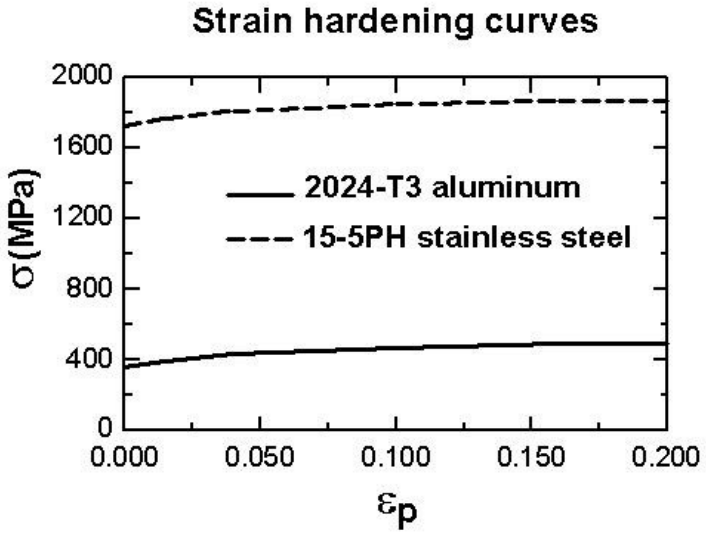

Figure 12. Strain hardening curves for grip material and specimen material

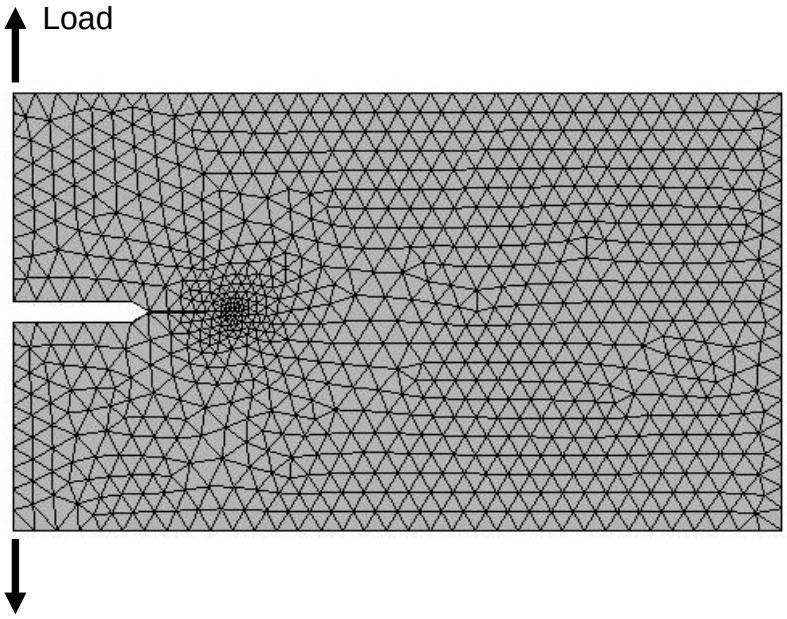

Figure 13. Initial finite element mesh of the plate with a single edge crack (front view)

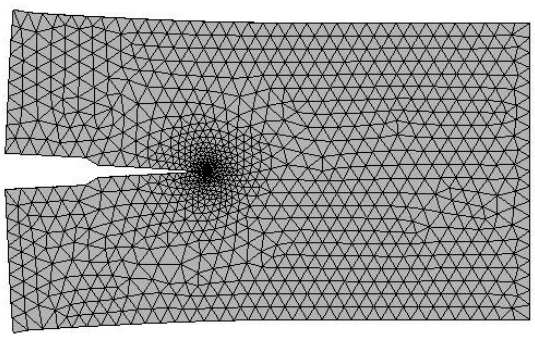

(a) Δa = 14mm

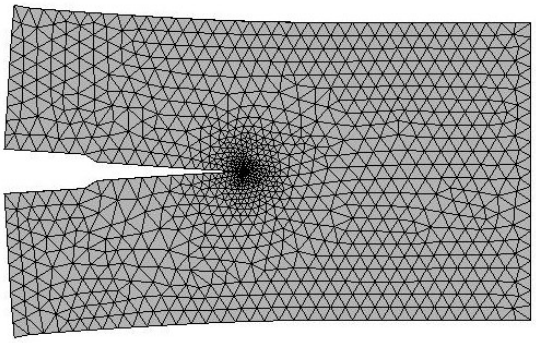

(b) Δa = 24mm

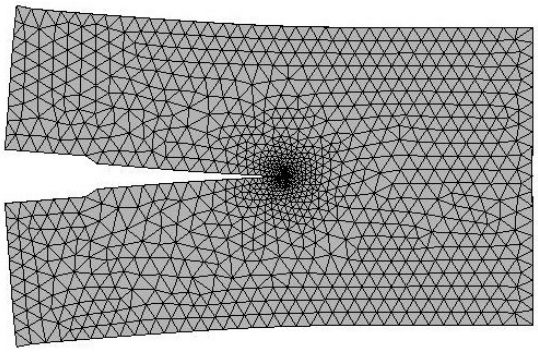

(c) Δa = 34mm

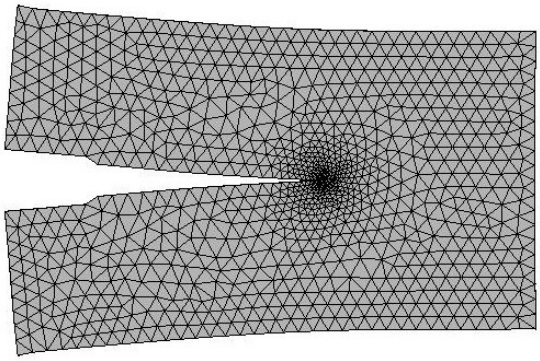

(d) Δa = 44mm

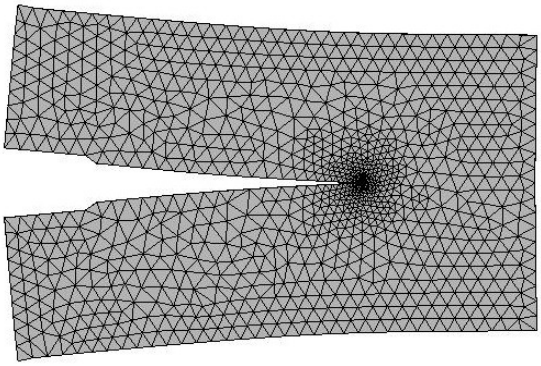

(e) Δa = 54mm

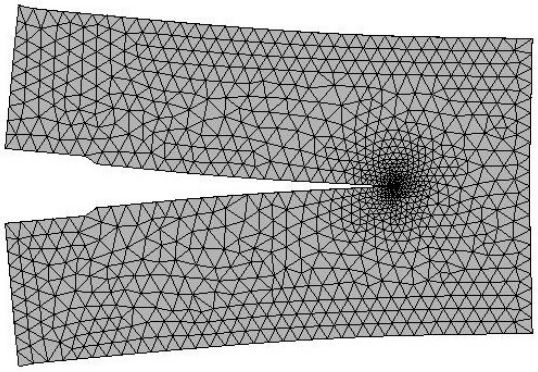

(f) Δa = 64mm

Figure 14. Mesh evolution and predicted crack path during the crack growth (front view)

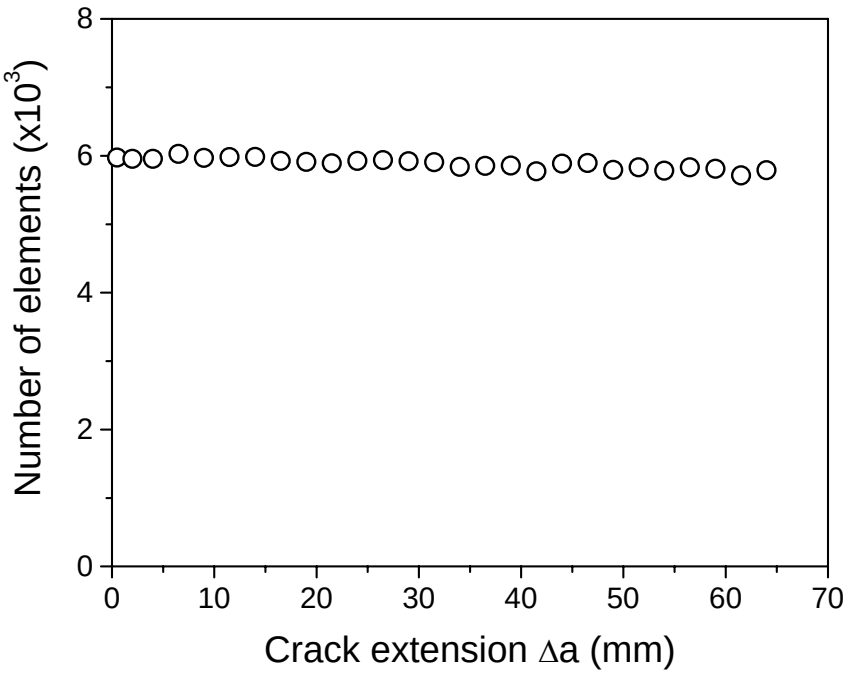

Figure 15. Number of elements versus crack extension during crack growth

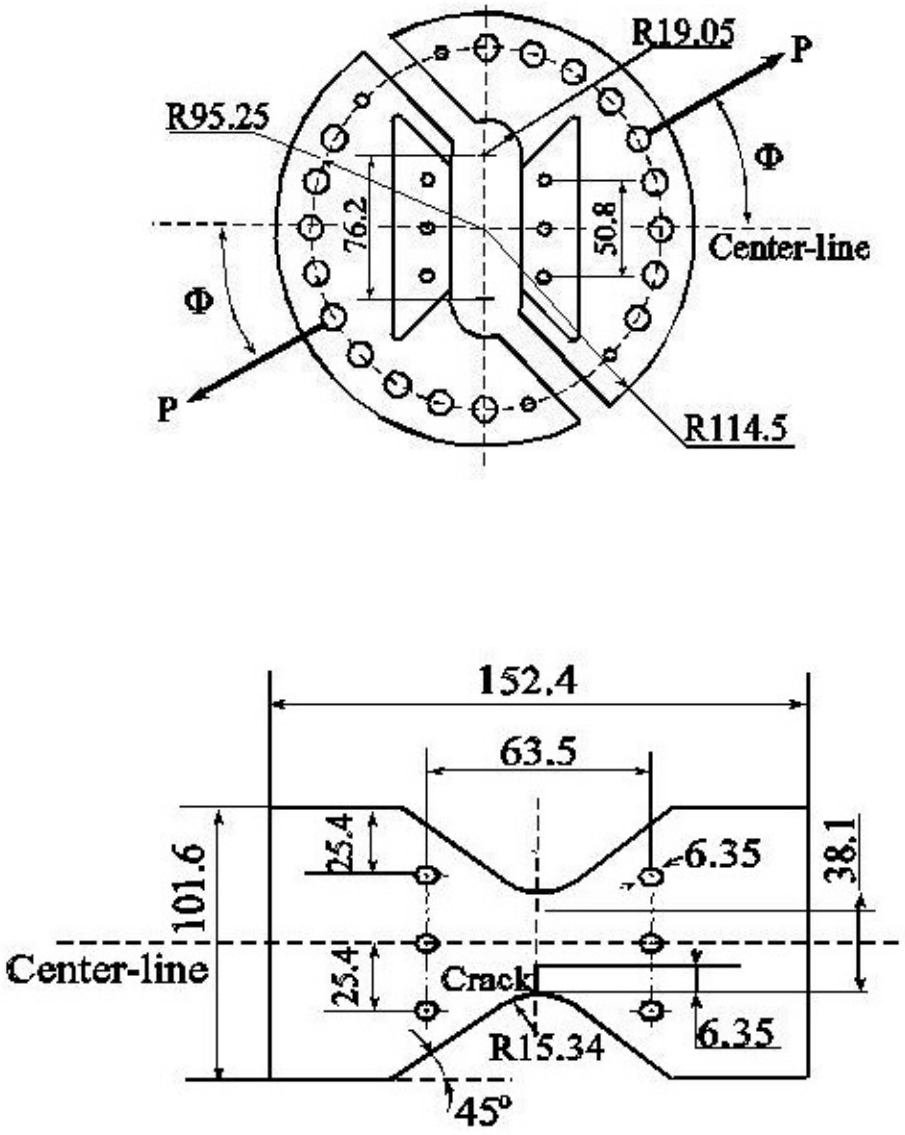

Figure 16. A schematic of the Arcan test specimen and loading fixture (all dimensions in mm)

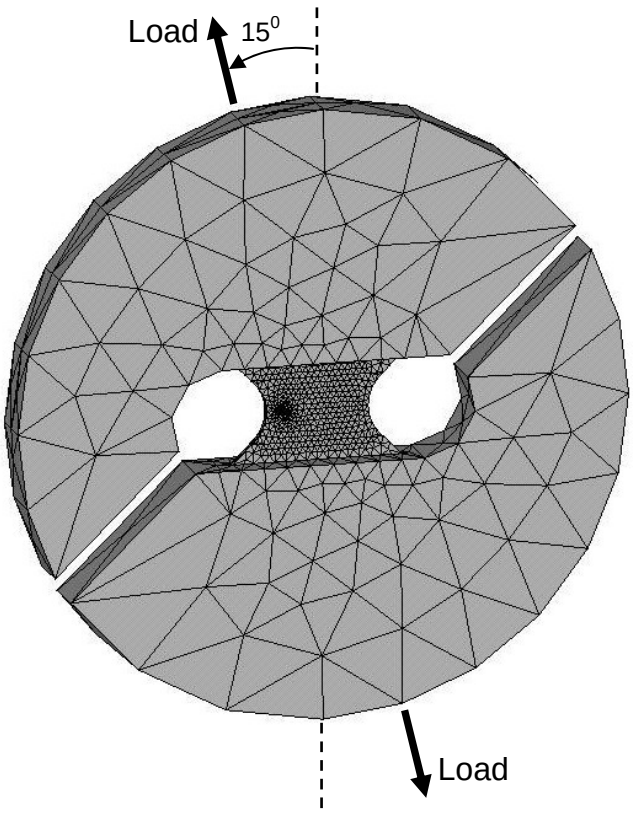

Figure 17. Initial finite element mesh and loading direction ($\Phi = 15^0$)

(a) Δa=3.2mm

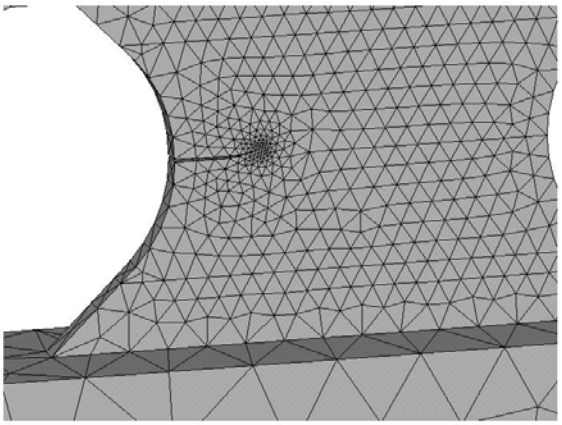

(b)
Δa=11.2mm

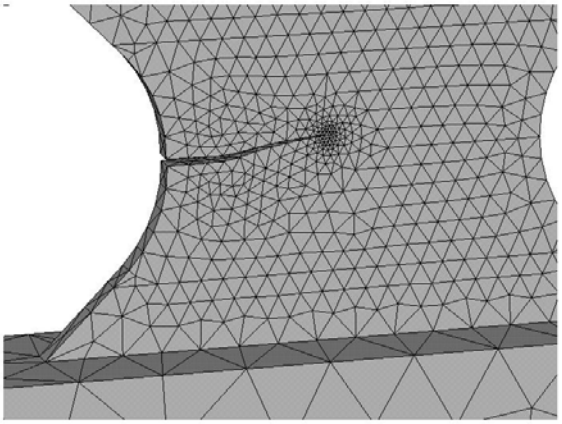

(c)
Δa=19.2mm

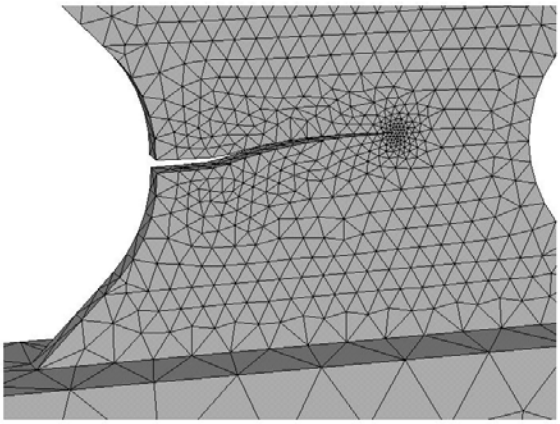

Figure 18. Crack propagation under mixed-mode loading

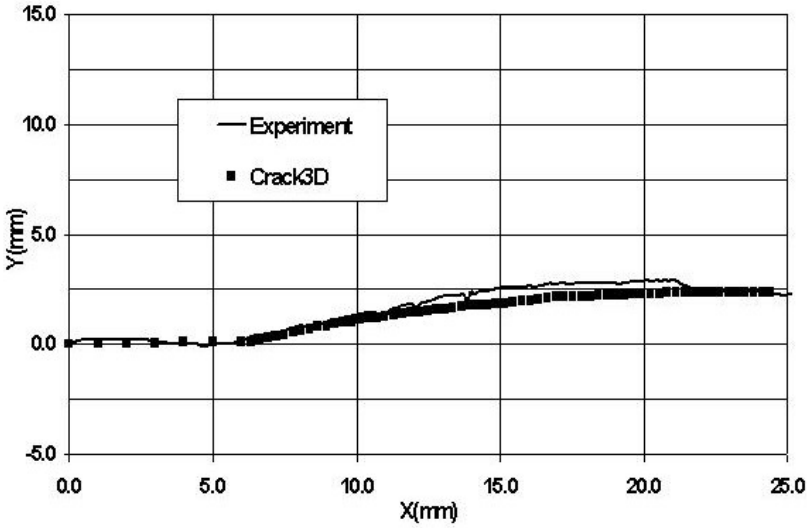

Figure 19. Comparison of the crack path ($\Phi = 15^0$)

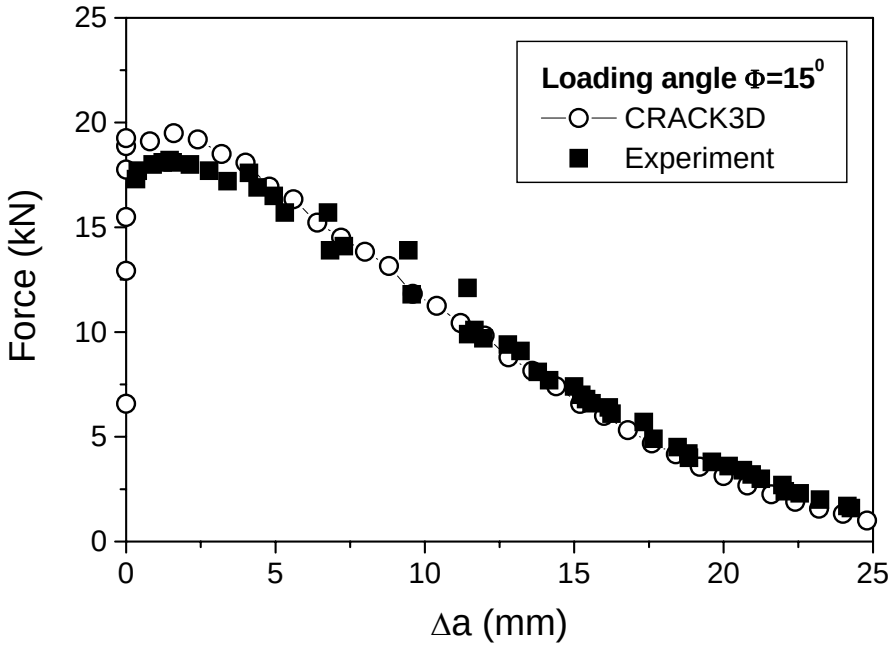

Figure 20. Experimental and numerical load versus crack extension

III. Analysis and Simulation of Three-Dimensional Crack Growth in Ductile Materials: Effect of Stress Constraint on Crack Tunneling

Abstract: This work describes the results of an effort to understand crack tunneling events in ductile materials, which is made possible by the finite element based crack growth simulation code, CRACK3D, where Section II describes the underlying computational schemes developed for general 3D crack growth simulation and their implementation in CRACK3D.

Crack tunneling is a crack growth feature often seen in stable tearing crack growth tests on specimens made of ductile materials and containing through-thickness cracks with initially straight crack fronts. As a specimen is loaded monotonically, the mid-section of the crack front will advance first, which will be followed by crack growth along the rest of the crack front, leading to the formation of a thumb-nail shaped crack-front profile. From the viewpoint of fracture mechanics, crack tunneling will occur if the operating fracture criterion is met first in the mid-section of the crack front, which may be due to a higher fracture driving force and/or a lower fracture toughness in the mid-section. A proper understanding of this fracture behavior is important to the development of a three-dimensional fracture criterion for general stable tearing crack growth in ductile materials. In this paper, the phenomenon of crack tunneling during stable tearing crack growth in a single-edge crack specimen is investigated by considering the effect of stress constraint on the fracture toughness. Crack growth in the specimen under nominally Mode I loading conditions is considered. In this case, crack tunneling occurs while the initially flat crack surface (which is normal to the specimen's lateral surfaces) evolves into a final slanted fracture surface. A mixed-mode CTOD fracture criterion and a custom three-dimensional fracture simulation code, CRACK3D, are used to analyze the tunneling and slanting process in the specimen. Results of this investigation suggest that the critical CTOD value (which is the fracture toughness) has a clear dependence on the crack front stress constraint (also called the stress triaxiality, which is the ratio of the mean stress to the von Mises effective stress). For simplicity, this dependence can be fitted to a straight line within the range of stress constraint values found, with the toughness decreasing as the constraint increases. It is found that crack tunneling in this case is mainly the result of a higher stress constraint (hence a lower fracture toughness) in the mid-section of the crack front. Details of the crack growth simulation and other findings of this study will also be presented.

III.1. Introduction

Prediction of ductile fracture in metallic materials has been an important subject of fracture mechanics research. A key focus of this research effort has been the development of fracture criteria for determining the onset and/or direction of crack growth. Currently, several approaches have been proposed to characterize the process of stable crack growth (e.g. J-Integral [1], J-A_2 [2], CTOD [3, 4] or CTOA [5] and so on).

Experimental results (e.g. [6-8]) show that crack tunneling is a common crack growth feature in stable tearing fracture in specimens made of ductile materials. For a specimen containing a through-thickness crack with an initially straight crack front, as the a specimen is loaded monotonically, the mid-section of the crack front will advance first and then the rest of the crack front will grow, leading to the formation of thumb-nail

shaped crack-front profiles. In addition to tunneling, slant crack growth may also occur in ductile materials. Stable tearing tests performed on specimens made of AL2024-T3 sheets indicate [6, 7] that slanting occurs when the specimens are in the LT orientation whereas it does not occur when the specimens are in the TL orientation. On the other hand, specimens made of AL 2024-T351 display both flat and slant crack growth in LT orientation [8]. However, what is consistent from these tests is that crack tunneling always occurs regardless of specimen orientation. However, tunneling in flat fracture is usually more severe than that in slant fracture.

From the viewpoint of fracture mechanics, the phenomenon of crack tunneling may be explained using a fracture criterion if a non-uniform fracture driving force and/or a non-uniform fracture toughness exists along the crack front. Specifically, tunneling will occur if the operating fracture criterion is met first in the mid-section of the crack front, either due to a higher fracture driving force and/or lower fracture toughness in the mid-section. A proper understanding of this fracture behavior is important to the development of a three-dimensional fracture criterion for general stable tearing crack growth in ductile materials.

The present work investigates crack tunneling during stable tearing crack growth in a single-edge crack specimen [6, 7], with a focus on the understanding of the effect of stress constraint on fracture toughness [9, 10], based on a CTOD fracture criterion [3, 4]. It is organized as follows. For reference purposes, Section 2 gives a brief description of the experimental results considered in this study. Section 3 introduces the finite element model and computational approach for simulating crack front evolution observed in the tests. Section 4 presents the distributions of CTOD and stress constraint along different crack fronts based on the simulation results and establishes a correlation between CTOD toughness values and stress constraint values in terms of a linear equation. As an application/verification, this equation is then used in Section 5 as part of the CTOD criterion to enable the simulation of the stable tearing tests to predict crack tunneling profiles during crack growth. The predicted results are compared with experimental measurements. Section 6 presents the conclusions from this study.

III.2. Crack tunneling measurement

Figure 1 provides a schematic of the single-edge crack specimen geometry [6]. The specimens were machined from rolled 2.3mm-thick sheets made of aluminum alloy 2024-T3. The specimens were then fatigue pre-cracked in the LT orientation so that the initial crack/width ratio, a/w=0.0833. To assess the amount of crack tunneling, an experimental procedure described in [11] was used to acquire crack front profile measurement data on the fracture surface at various levels of loading, as shown in Figure 2 for stable tearing crack growth in a specimen under remote Mode I loading conditions. The corresponding applied load for each crack front profile is also included in the figure. It is noted that, after the initiation of crack growth, the fracture surface undergoes a transition from an initially flat crack plane to a steady slanted crack plane as the crack front advances.

III.3. Finite element model and computational approach

The finite element method is used to analyze the stable tearing crack growth experiments described above in order to understand the crack tunneling phenomenon. To carry out such analyses, a finite element code capable of simulating general three-dimensional (3D) crack growth in elastic-plastic solids is required. In this study, the custom code CRACK3D developed at the University of South Carolina is used. Preprocessing (for generating the initial finite element mesh) and post-processing (for analyzing stress and deformation state at a particular stage of crack growth) are performed using the commercial code ANSYS, through interface options in CRACK3D.

Two simulation options are available in CRACK3D. In the first option (the nodal release option), the crack front is made to advance along a prescribed path, which is accomplished through the release of nodal pairs (the two nodes in a pair are initially tied together by rigid springs) along the crack path when a certain condition (e.g. when a critical load from a test is reached) is satisfied. This option is useful for analyzing fracture tests. In the second option (the local remeshing option), the crack front position is not prescribed but is predicted by a fracture criterion (the CTOD criterion in this study) and a user-specified region around the new crack front is remeshed as the crack front grows.

Figure 3 shows frontal planar views of a 3D finite element mesh used in analyzing the stable tearing tests based on the nodal release option, where Fig. 3(a) is for the entire problem domain and Fig. (b) a local view of the mesh around the crack front (note that the fatigue crack front has extended from the initial notch into the region on the right). The mesh consists of 8,917 ten-node tetrahedral elements with 14,315 nodes. The minimal element size around the crack front is 0.2 mm. A remote Mode I load was applied in terms of a monotonically increasing displacement, so that nodes at the bottom edge of the specimen were constrained with zero displacements in all directions, and nodes at the specimen's top edge were made to move in the y-direction (vertical direction) (while displacements in the x and z directions were held to zero).

Mesh convergence analysis has been performed by bisecting each edge of elements in 3D space. The study of mesh convergence here is focused mainly on two parameters, the stress constraint and the crack opening displacement (COD) (note that values of COD at points not far from the crack front are called CTOD in this paper). Figures 4 and 5 show comparisons of the numerical results obtained based on finite element mesh I (as shown in Fig. 3 with element size of 0.2mm around the crack front) and finite element mesh II, which is a refined mesh with element size of 0.1mm around the crack front. The values of COD in Fig. 4 are computed on the front surface of the specimen, while the values of the stress constraint in Fig. 5 are computed on the mid-plane of the specimen. The reason for choosing the mid-plane of the specimen for this evaluation is that the gradient of the stress constraint ahead the crack front on the mid-plane of the specimen is much larger than that on the free surfaces of the specimen.

It can be found based on HHR fields [12, 13] that both the mean stress and the von Mises effective stress have the same singularity in terms of the distance to crack tip. Therefore, the stress constraint (which is the ratio of mean stress and von Mises effective stress) is expected to be independent of the distance to the crack tip in a near-tip region under small scale yielding (SSY) and HRR-dominance conditions. Indeed under plane strain conditions [14] the stress constraint is nearly constant along the

radial direction in the region around crack tip. However, neither the plane strain condition nor the plane stress condition can be exactly satisfied in real-life cracked structures. Due to variations of field singularities along three-dimensional crack fronts, the stress constraint is expected to depend somewhat on the radial distance to the crack front even though a strong near-tip singularity is not observed (see Fig. 5). To alleviate this radial dependence, an average stress constraint value is taken in this paper, which is obtained by integrating the stress constraint over a small distance ahead of the crack fronts.

To evaluate fracture parameter values around the actual 3D crack fronts, the experimentally measured fracture surface and crack front profiles associated with different loading levels (see Fig. 2) were built into the finite element mesh to be used in the nodal release approach. It is noted that the crack front profiles used in the finite element model have been slightly smoothed. Figure 6 shows the profiles of smoothed crack fronts in the finite element model. Due to slant crack growth, the fracture surface is not flat. As such, Fig. 6 is only a projected section view of the actually slant fracture surface (viewed from the positive y-direction; see Fig. 1). The profiles numbered 1, 2, 4, and 6 are for crack fronts measured based on fatigue striation marks during interrupted crack growth tests, and the profiles numbered 3 and 5 are interpolated from profiles 2 and 4, and 4 and 6, respectively. Since the x-y plane coincides with the specimen's mid-plane (where z is zero), the back surface of the specimen corresponds to negative z coordinates and the front surface corresponds to positive z coordinates. A typical 3D crack front profile is shown in Fig. 7.

It is noted that crack front #1 is the initial fatigue crack front and has slight tunneling in the middle. As the specimen is loaded monotonically to the critical load for the initiation of crack growth, the middle region of the specimen grows first while the regions in the specimen's front and back surfaces remain stationary. As the load is further increased, the crack front advances from crack front #1 to crack front #2. The flaw eventually advances to crack front #6, with an increasing amount of crack tunneling. The maximum load required for continued crack growth occurred at crack front #6, after which the required load began to decrease gradually.

CRACK3D is used to analyze the crack tunneling and slanting process in the specimen. With respect to the fracture criterion used during the simulation, the measured critical load corresponding to each crack front is used to control the crack growth at different crack length. The total CTOD (defined as the vector magnitude of its opening, shearing and tearing components) and stress constraint (defined as the ratio of the mean stress to the von Mises effective stress) with regard to the normal plane at each node on crack front are evaluated at the critical instant just before crack propagation.

In a CTOD based fracture criterion [3, 4], the driving force is the total CTOD, which is measured at a fixed distance behind the crack front. In this study, CTOD was strictly computed at a distance of 0.5 mm behind the crack front (along a line normal to the crack front). Since it is impractical to use an extremely refined mesh and an extremely small distance behind the crack front for computing CTOD, and since severe crack tunneling creates a length scale that may not be sufficient large compared to 0.5 mm, the computed CTOD value is expected to be less accurate in the middle region of a crack front than away from that region. The reason is that, due to severe crack

tunneling in the middle region, a point at 0.5 mm (or another small distance) behind the crack front along a line normal to the crack front may be too close to other parts of the crack front, making this point inappropriate for calculating CTOD. To alleviate this problem, it is chosen in the calculation to compute a nominal CTOD value, when the situation noted above occurs, by using the crack-front CTOA (crack-tip opening angle) value to extrapolate to a distance of 0.5 mm behind the crack front.

It is important to note that, in this analysis phase of the study, crack growth simulations were performed using the nodal release option, with the experimentally measured crack front profile positions and the corresponding loads. The CTOD criterion was not applied even though CTOD variations along the crack fronts were evaluated.

III.4. Effect of stress constraint on critical CTOD

The main results of interests from the finite element simulations described in the preceding section are the variations of CTOD and stress constraints along the measured crack fronts, which will be used to establish a correlation between CTOD fracture toughness and stress constraint. Since the CTOD values along a crack front correspond to the critical load that causes growth of the crack front, they are critical CTOD values and equal to the corresponding CTOD fracture toughness values along the crack front.

Figures 8, 9, 10 provide the variations of the total (combined) CTOD and CTOD components for Mode I (opening), Mode II (shearing) and Mode III (tearing) along crack fronts #4, #5, and #6, respectively, at a distance of 0.5 mm behind the crack front (along a line normal to the crack front). In the figures, the through-thickness value refers to the z coordinate value along the crack front. Results for crack fronts in the early stage of crack growth are not shown because these crack fronts have growth only in the middle section and do not provide reliable critical CTOD values (note that CTOD values along parts of the crack front that are not at the impending moment of growth are not critical values and do not equal to CTOD fracture toughness values there).

Two important observations can be made from these figures. First, due to crack tunneling and slanting, a perfect symmetry about the specimen's mid-plane, a feature expected in Model I crack growth, is seen to disappear as crack grows, which lead to a truly three-dimensional mixed-mode CTOD distribution along the crack front, especially in the middle region of the crack fronts. The crack front is Mode I dominant only in the middle region. Second, the total CTOD value (which represents the CTOD-based fracture toughness during crack growth) is not a constant along the crack front—it is lower in the middle region than near the specimen surfaces. As discussed later, this variation in fact reflects the dependence of CTOD toughness on the stress constraint A_m.

Alternatively, variations of the total CTOD along the crack fronts can be plotted in one figure, as shown in Fig. 11. It is seen that the trend shown in the variations along different crack fronts is basically the same. This observation will be utilized subsequently to relate CTOD variation with stress constraint variation along the crack fronts. Before this is done, it must be pointed out that CTOD variations shown so far are strictly computed at a distance of 0.5 mm behind the crack front. Because of severe tunneling (as discussed earlier), the computed CTOD values are less accurate in the middle region of a crack front than away from that region. It is suggested earlier that

improved CTOD values in the middle region can be obtained by using the crack-front CTOA value to extrapolate to a distance of 0.5 mm behind the crack front. This seems to be a viable approach for crack fronts after a certain amount of crack growth, so that crack blunting usually seen at the early stage of crack growth can be avoided. Based on this approach, the total CTOD variations in Fig. 11 are updated and are shown in Fig. 12.

Shown in Fig. 13 are the variations of A_m along crack fronts #3, #4, #5, and #6. The constraint value at each crack front point is computed based on an integrated average from the crack front to 0.3 mm ahead of the crack front, in the direction normal to the crack front, within the plane of the crack surface. It must be pointed out that, at and very near the specimen's front and back surfaces, a distance of 0.3mm ahead of a crack front may go outside the specimen domain. In this case, we use the constraint value of the next interior crack front point to approximate the constraint value for the current crack front point. Similar to the total CTOD variations in Fig. 12, a common trend in the stress constraint variations can also be seen.

To reduce scatter in the subsequent data reduction for possible correlation between CTOD toughness and stress constraint A_m, the variations in Figs. 12 and 13 need to be smoothed. To this end, an averaged total CTOD variation is obtained from Fig. 12 and an averaged stress constraint variation is obtained from Fig. 13. Now, a correlation between CTOD and A_m can be obtained by plotting all (CTOD, A_m) pairs from the same crack front locations, and this correlation is shown in Fig. 14. It is seen that the CTOD-based fracture toughness value decreases as the value of the stress constraint increases. For simplicity, a straight line can be used to fit the CTOD-A_m data points within the range of values for A_m, which can be written as

$$\text{CTOD}=0.0932-0.0312\,A_m \qquad (1)$$

Since the CTOD and A_m values are extracted from simulation results of actual fracture tests, with experimentally recorded crack fronts and load values during stable crack growth, there is strong reason to believe that Eq. (1) may represent the dependence of the CTOD based fracture toughness on stress constraint A_m for the material in concern, aluminum alloy 2024-T3. Eq. (1) suggests that the CTOD fracture toughness value is lower when the stress constrain is higher.

If validated by further studies, the simple linear fit described by Eq. (1) or a more accurate curve fit can be treated as a material property and can be extremely useful in three-dimensional fracture mechanics applications where constraint effects on fracture toughness are important.

III.5. Prediction of crack tunneling

The relationship between the CTOD toughness and stress constrain can be used to predict crack tunneling based on the CTOD fracture criterion. To demonstrate this application, the remote Mode I stable tearing fracture test described in previous sections is now simulated. Two types of simulations using CRACK3D are performed.

In the first case, the nodal release option is used with a coarse mesh (to save computation time) with design similar to that in Fig. 3. The mesh consists of 3,308 ten-node tetrahedral elements with 6,169 nodes. The minimal element size around the crack front is 0.4mm. The difference between the simulation here and that in section 4 is

that, there are no specified crack front positions on the crack surface except for the initial fatigue crack front (see Fig. 15). The crack front shape is predicted by the CTOD criterion and Eq. (1) even though the crack front is constrained to grow on the measured slant fracture surface. Since the nodal release option is used, the elements are fixed. As a result, some mesh dependence in the predicted crack front positions is expected (see Fig. 16). The dependence can be reduced if finer meshes are used (a coarse mesh is used here). Alternatively, the crack front profile can be smoothed based on predicted crack growth amounts at difference points along the crack front.

In the second case, instead of using a fixed mesh and the nodal release option, the local remeshing option is used so that the mesh in a user-specified region around the current crack front is remeshed each time the crack front is predicted to grow. Again, the CTOD criterion and the relationship between the CTOD toughness and stress constraint are employed to predict the crack front profile although the crack front is still constrained to grow on the measured slant fracture surface.

All simulations are conducted using CRACK3D. In the simulations, the CTOD criterion is evaluated node by node along the current crack front. A crack-front point will advance along the measured slant fracture surface when the CTOD value at that point reaches the critical value defined by the stress constraint A_m ahead of the crack front according to Eq. (1).

The predicted crack front profiles (without smoothing) during stable crack growth are shown in Fig. 16 (with nodal release) and Fig. 17 (with local remeshing). In order to make the different crack fronts displayed clearly, some of crack fronts in (Fig. 16) are displayed in dotted lines. From both figures it was found that the crack starts to grow at the mid-section of specimen first, and crack tunneling happens as the crack propagates. The shape of crack front is consistent with the measured crack fronts. The depth of crack tunnel on the crack path increases in the early stage of crack growth, and decreases after the crack extension on the surface of specimen is about 1mm, which is consistent with the measured results.

Comparisons of predicted and measured crack tunneling variations during crack growth can be made by the use of a non-dimensional crack tunneling depth parameter, as defined below and in Fig. 18 (a). Let Δa_1 be the amount of crack extension on the specimen's back surface, Δa_2 the amount of crack extension on the specimen's front surface, and Δa_c the amount of crack extension on the mid-plane of the specimen. The average crack extension on the specimen's front and back surfaces is

$$\Delta a_S = \frac{\Delta a_1 + \Delta a_2}{2} \qquad (2)$$

Then the non-dimensional crack front tunneling depth, T, is defined as

$$T = \frac{\Delta a_C - \Delta a_S}{B} \qquad (3)$$

where B is the thickness of the specimen. Figure 18 (b) shows the variations of T based on crack-front profile measurements and simulation predictions using the nodal release and local re-meshing options of CRACK3D. A good agreement is observed in both cases.

III.6. Conclusions

In this study the crack tunneling phenomenon is investigated by considering stable tearing crack growth in a single-edge crack specimen made of AL 2024-T3. Although the specimen was loaded remotely under Mode I conditions, severe crack tunneling and slant fracture were both present during crack growth. This test was analyzed using a custom three-dimensional crack growth simulation code, CRACK3D.

Results of this study show that the CTOD-based fracture toughness for the ductile material considered is a function of stress constraint at the crack front. Based on the experimentally recorded crack front profiles and the corresponding critical loads, the simulation results suggest that the relationship between the CTOD toughness and the stress constraint, for AL 2024-T3 and within the stress constraint values, can be fitted to a simple linear curve, such that a higher stress constraint value would lead to a lower CTOD toughness value.

Based on this study, crack tunneling in the specimen may be interpreted as the result of a lower CTOD toughness (due to higher stress constraint) at the mid-section of the crack front and a higher CTOD toughness (due to lower stress constraint) near the specimen's front and back surfaces. Good comparisons of the predicted and measured crack front profiles seem to confirm the result of a previous study [10] that stress constraint is a key parameter in ductile failure and fracture criteria.

Acknowledgements
The authors gratefully acknowledge the sponsorship of this work by GM, AFRL and NASA.

III.7. References

[1] Hutchinson, J.W. and Paris, P.C., 1979, "Stability analysis of J-controlled crack growth, Elastic-plastic fracture", ASTM STP 668, pp.37-64.

[2] Chao, Y.J. and Sutton, M.A., 1994, "On the fracture of solids characterized by one or two parameters: theory and practice", Journal of the Mechanics and Physics of Solids, 42, pp. 269-647.

[3] Ma, F., Deng, X., Sutton, M. A., and Newman, J. C., Jr., 1999, "A CTOD-based mixed-mode fracture criterion," Mixed-Mode Crack Behavior, ASTM STP 1359, pp. 86-110.

[4] Sutton, M. A., Deng, X., Ma, F., J. C. Newman, Jr., and M. James, 2000, "Development and application of a crack tip opening displacement-based mixed mode fracture criterion," International Journal of Solids and Structures 37, pp. 3591-3618.

[5] Dawicke, D.S. Sutton, M.A., Newman Jr. J.C. and Bigelow, C.A., 1993, "Measurement and analysis of critical CTOA for an aluminum alloy sheet", NASA TM 109024. Hampton, VA: NASA Langley Research Center.

[6] Boone, M. L., 1999, "Characterization of stable tearing in thin sheet of 2024-T3 aluminum alloy under tension-torsion loading conditions," Master Thesis, Department of Mechanical Engineering, University of South Carolina.

[7] Sutton, M. A., Helm, J. D. and Boone, M. L., 2001, "Experimental study of crack growth in thin sheet 2024-T3 aluminum under tension-torsion loading", International Journal of Fracture, 109, pp. 285-301.

[8] James, M.A. and Newman Jr. J.C., 2003, “The effect of crack tunneling on crack growth: experiments and CTOA analysis”, Engineering Fracture Mechanics, 70, pp. 457-468.
[9] Hancock, J.W. and Mackenzie, A.C., 1976, “On the mechanisms of ductile failure in high-strength steels subjected to multi-axial stress-states”, J. Mech. Phys. Solids, 24, pp.147-169.
[10] Zuo, J., Sutton, M.A. and Deng, X., 2004, “Basic studies of ductile failure processes and implications for fracture prediction”, Fatigue & Fracture of Engineering Materials & Structures, 27, pp. 231-243.
[11] Dawicke, D.S. and Sutton, M.A., 1994, “CTOA and crack tunneling measurements in thin sheet 2024-T3 aluminum alloy”, Exp. Mech. 34, pp. 357-368.
[12] Hutchinson, J.W., 1968, “Plastic stress and strain fields at a crack tip”, J. Mech. Phys. Solids 16, pp. 337–347.
[13] Rice, J.R., Rosengren, G.F., 1968, “Plane strain deformation near a crack tip in a power law hardening material”, J. Mech. Phys. Solids 16, pp. 13–31
[14] Ma, F., Sutton, M.A and Deng, X., 2001, “Plane strain mixed mode crack-tip stress fields characterized by a triaxial stress parameter and a plastic deformation extent based characteristic length”, J. Mech. Phys. Solids 49, pp.2921-2953.

III.8. Figures

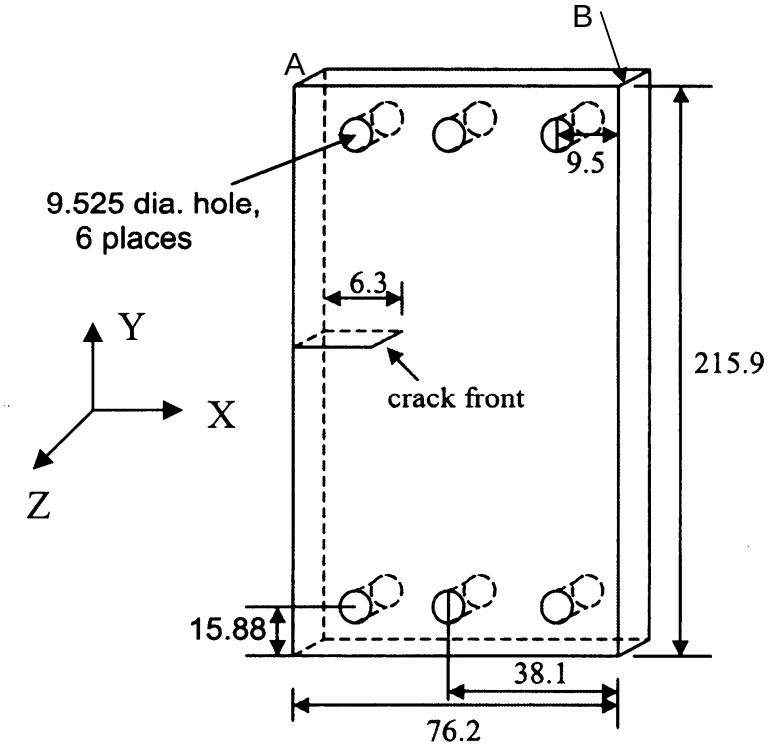

Fig. 1 Schematic of a single-edge crack test specimen (all dimensions in mm).

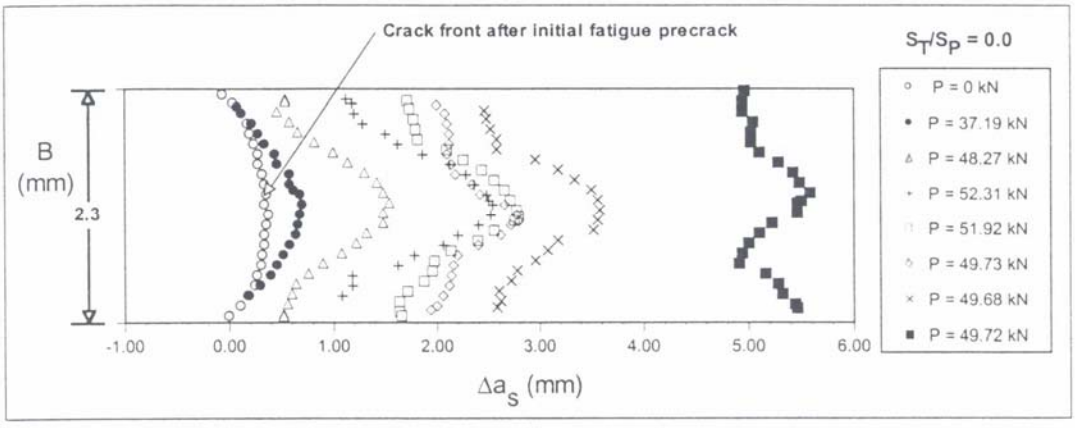

Fig. 2. Crack front profiles from a Mode I stable tearing crack growth test.

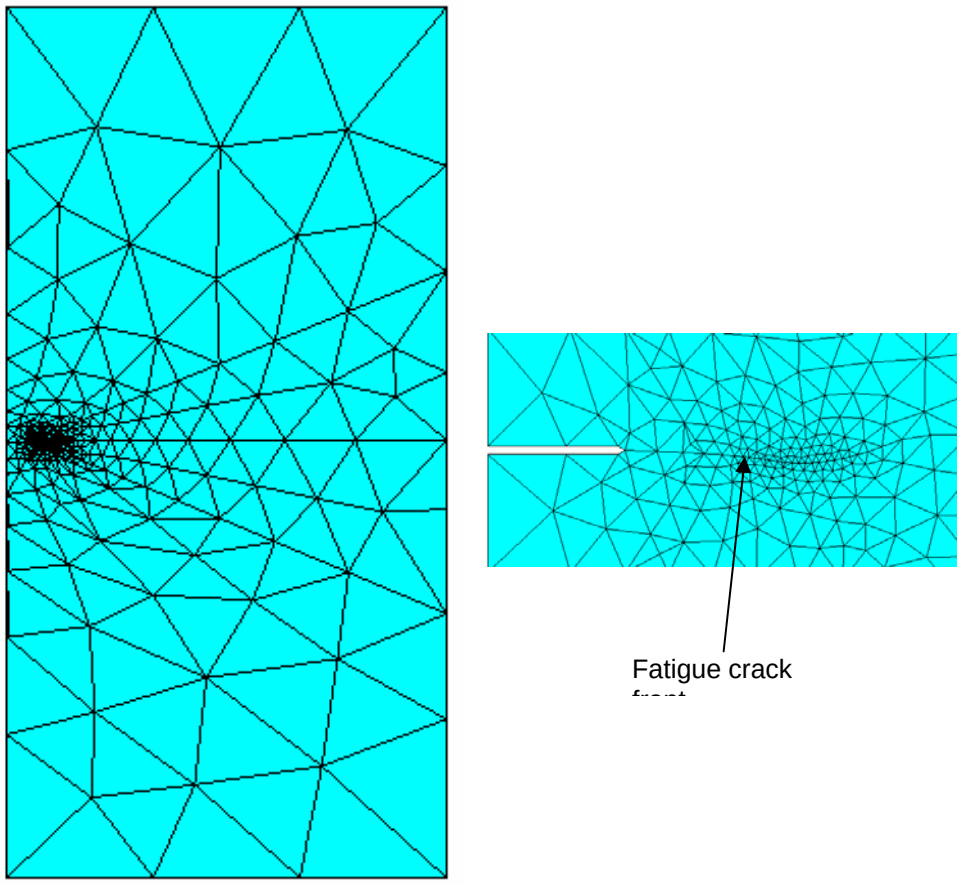

Fig. 3 Frontal views of the finite element mesh: (a) mesh for the entire problem domain and (b) zoomed-in mesh around the crack front.

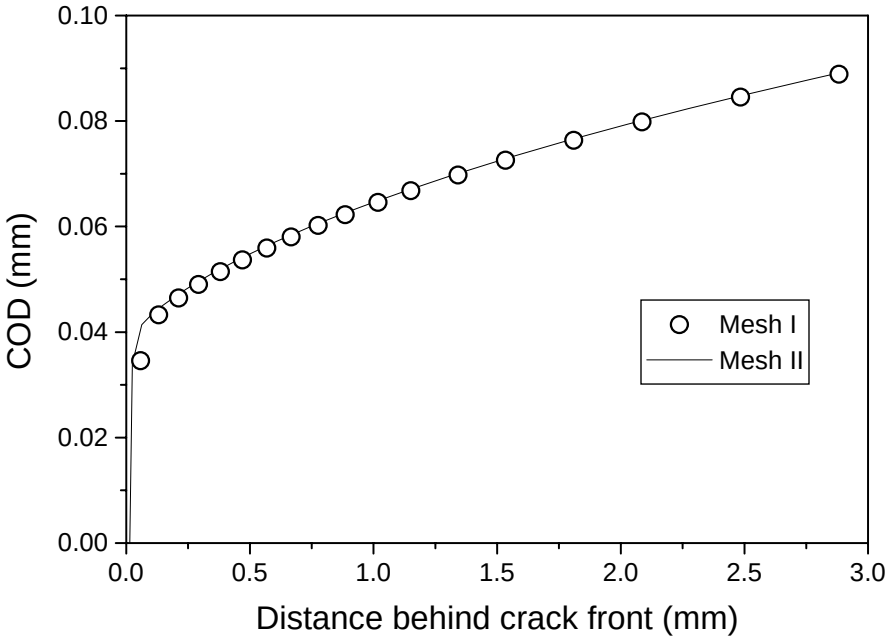

Fig. 4 COD comparison between two finite element meshes

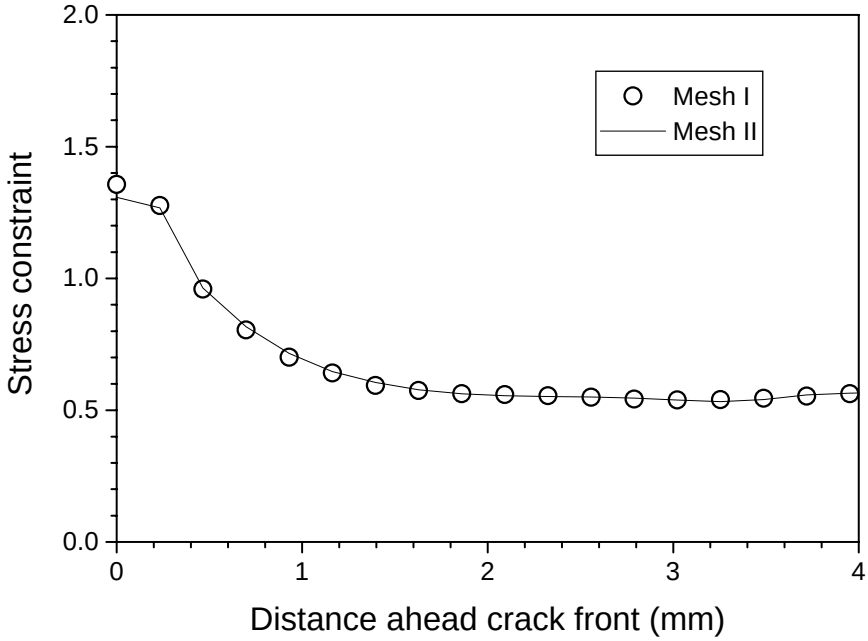

Fig. 5 Stress constraint comparison between two finite element meshes

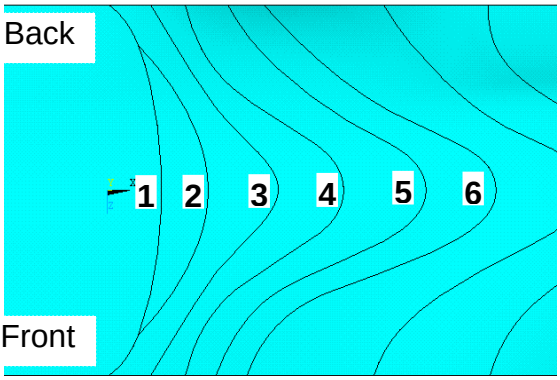

Fig. 6 Crack front profiles used in stable tearing crack growth analyses

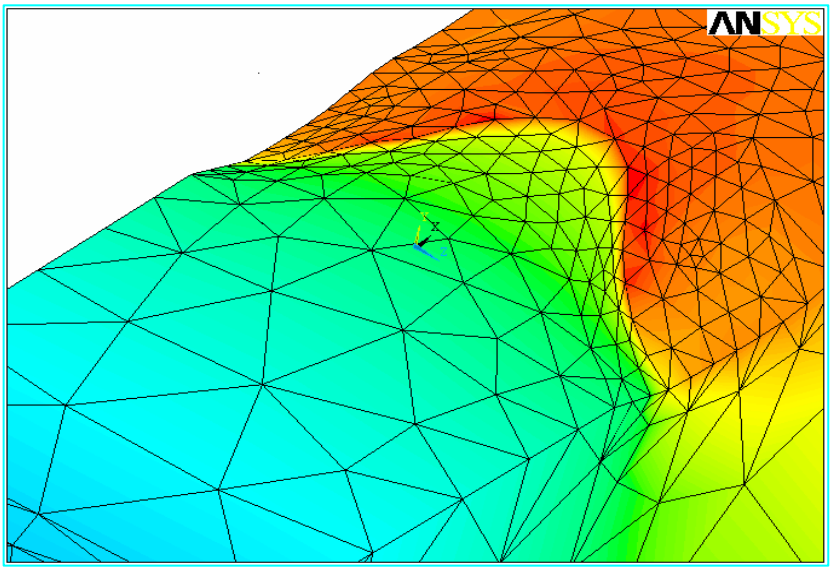

Fig. 7 A 3D crack front profile from a stable tearing crack growth test.

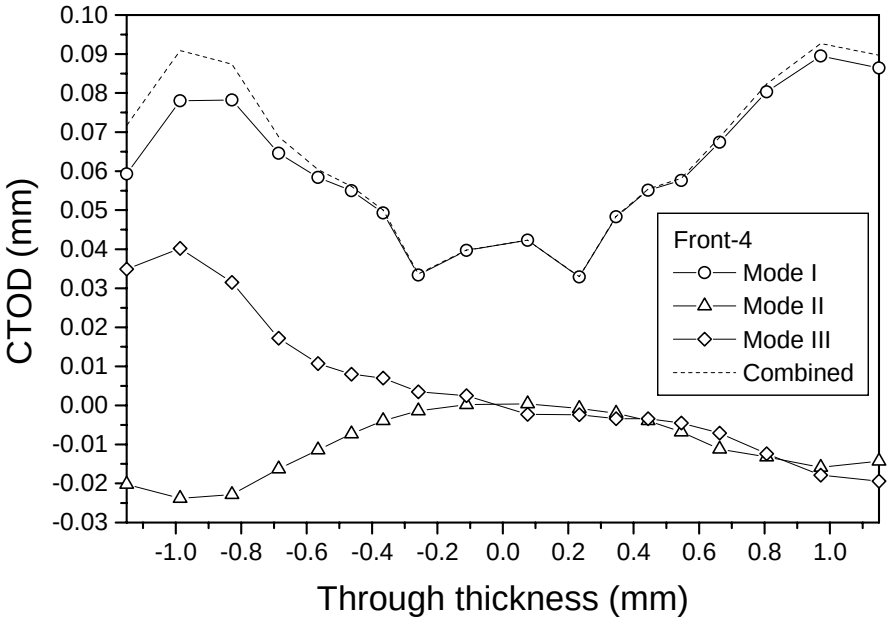

Fig. 8 Variation of CTOD and its components along crack front #4

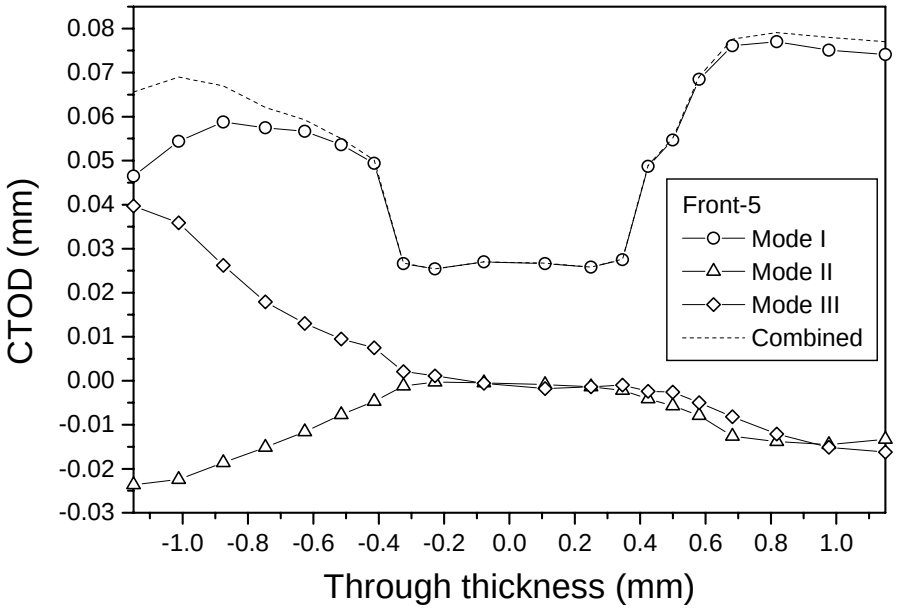

Fig. 9 Variation of CTOD and its components along crack front #5

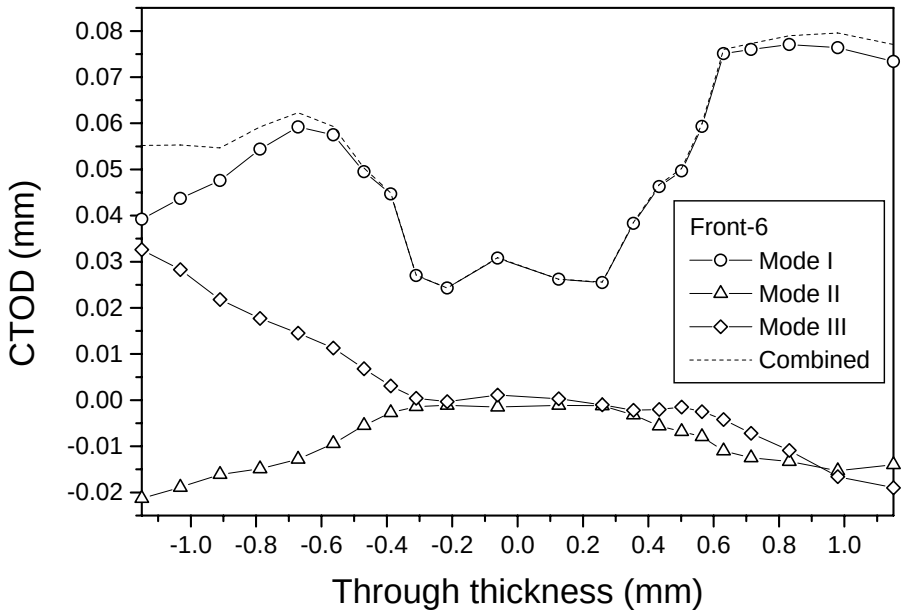

Fig. 10 Variation of CTOD and its components along crack front #6

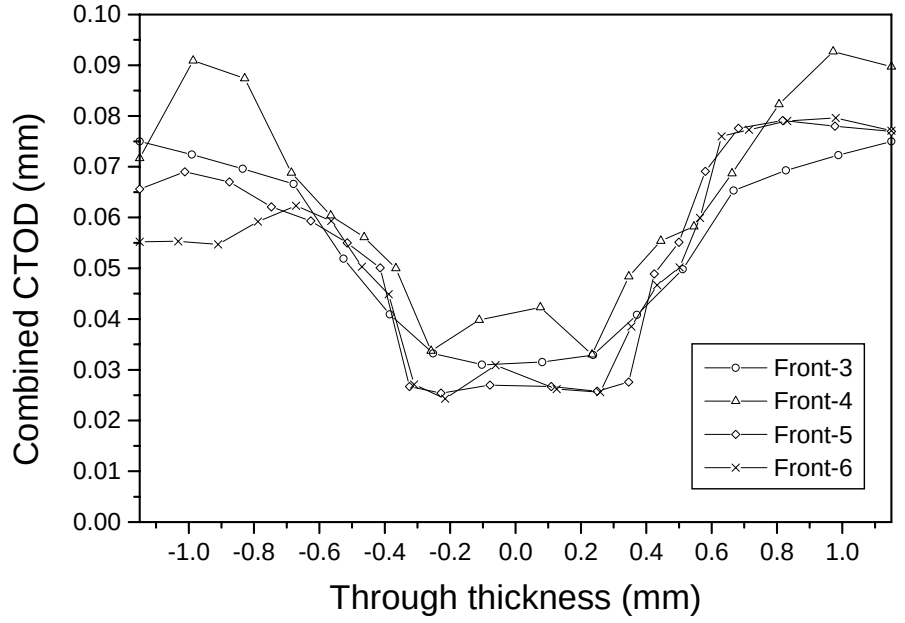

Fig. 11 Variation of total CTOD along crack fronts #3, #4, #5, #6 at 0.5 mm behind the crack front.

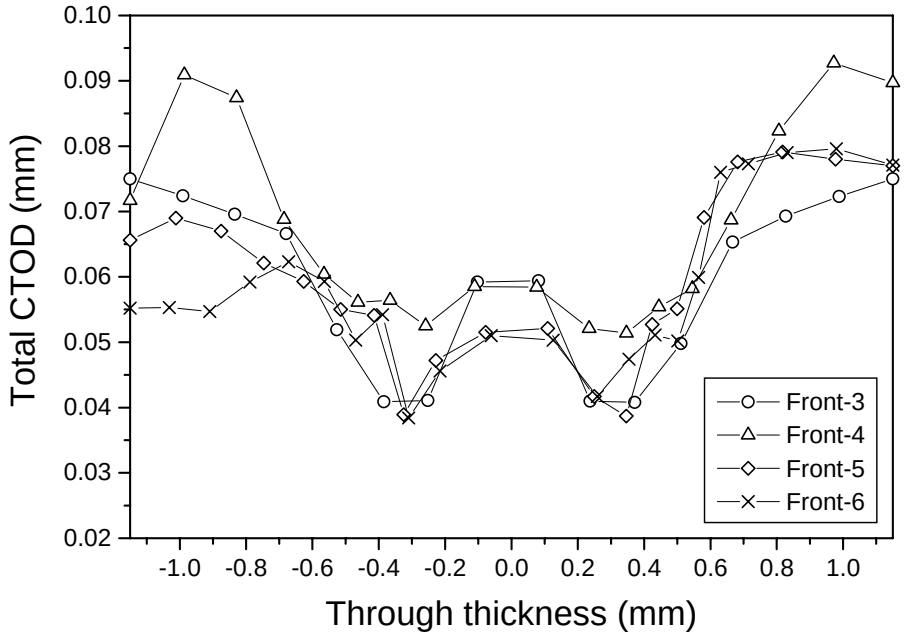

Fig. 12 Variation of total CTOD along crack fronts #3, #4, #5, #6 based on improved CTOD calculations in the middle region of the crack front.

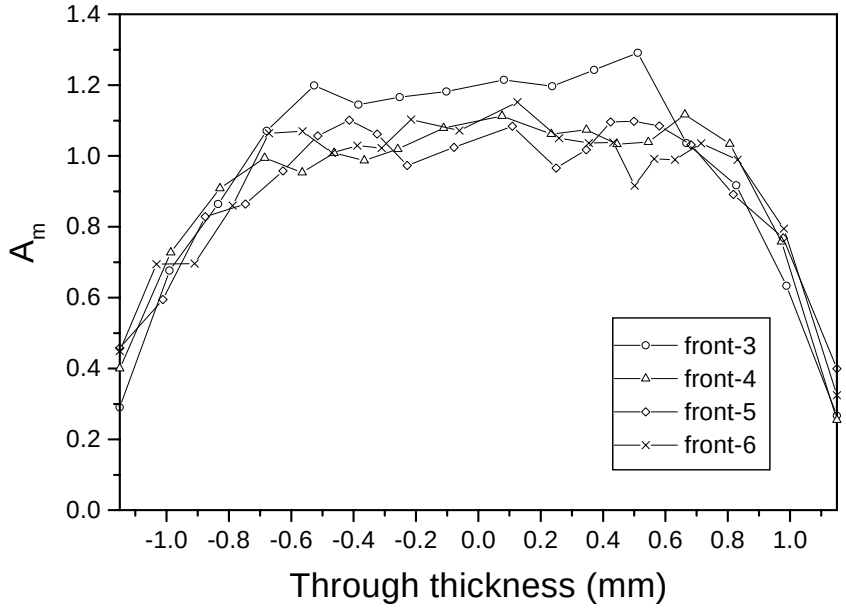

Fig. 13 Variation of stress constraint A_m along crack fronts #3, #4, #5, #6

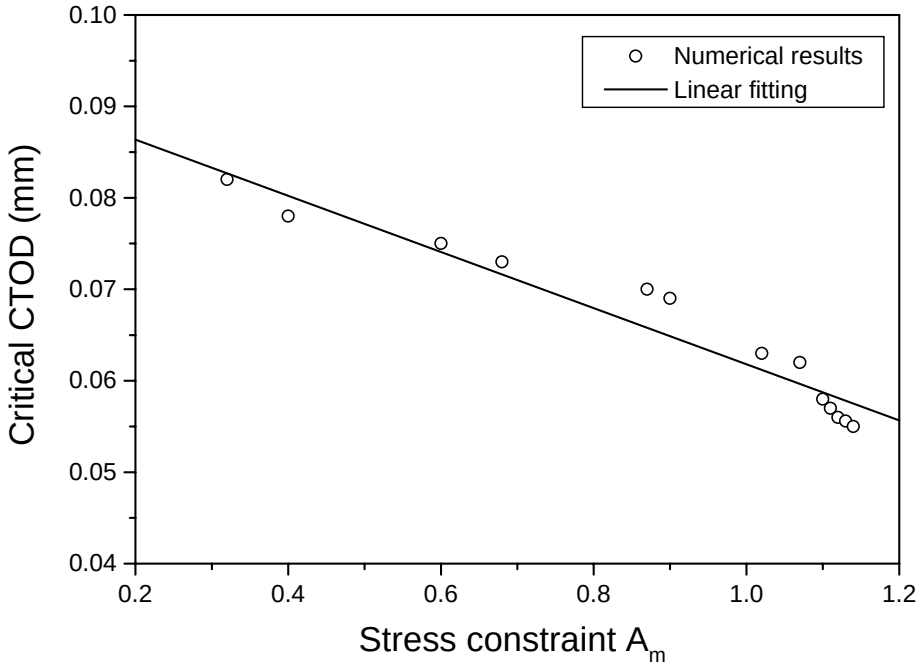

Fig. 14 Correlation between the critical CTOD and stress constraint A_m

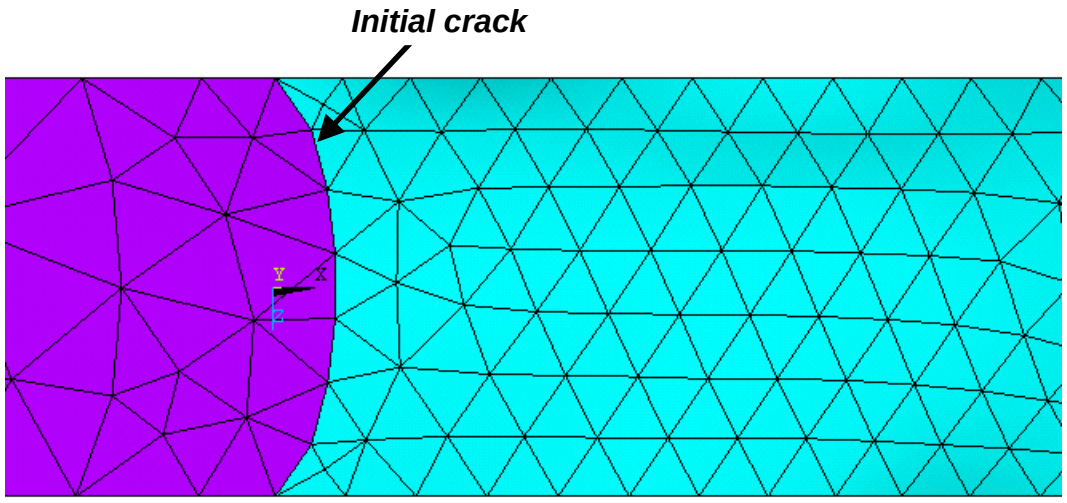

Fig. 15 Finite element mesh on the fracture surface

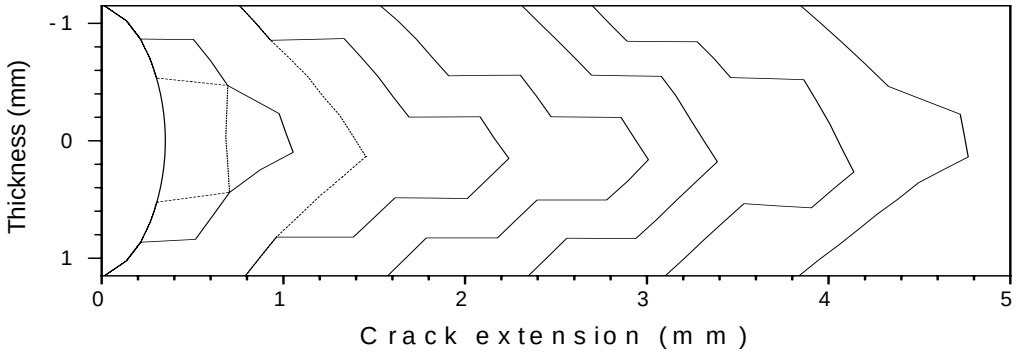

Fig. 16 Predicted crack front profiles (with nodal release).

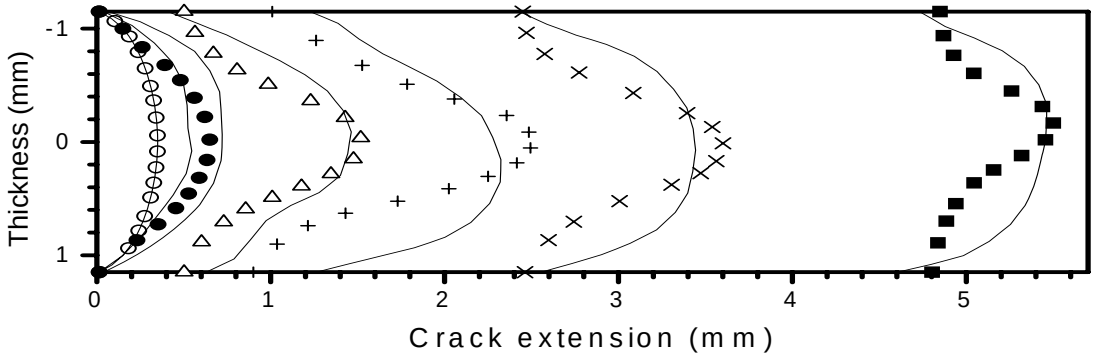

Fig. 17 Comparisons of predicted (solid lines, with local remeshing) and measured (symbols) crack-front profiles.

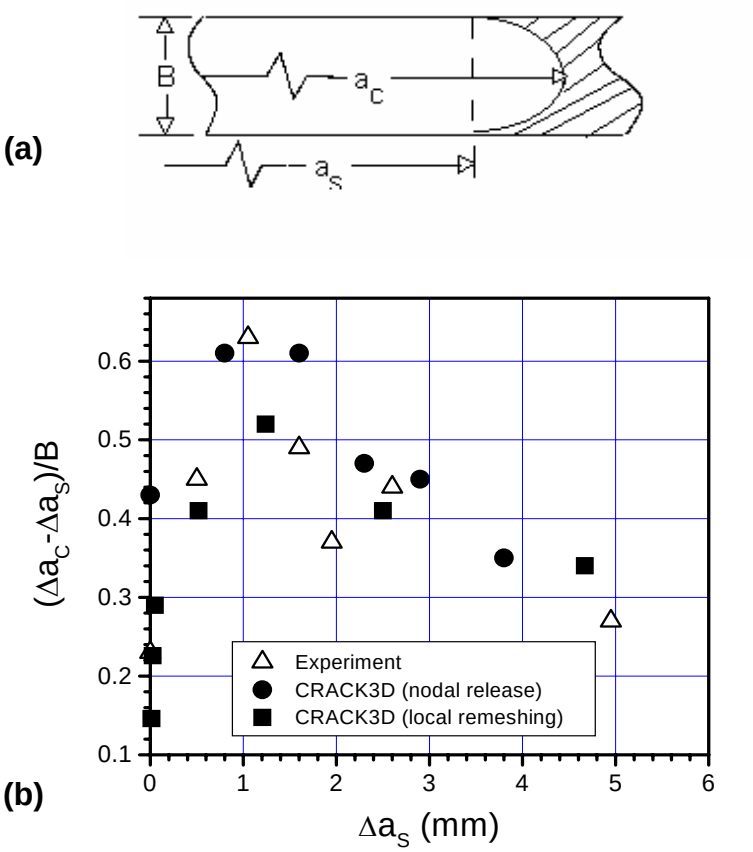

Fig. 18 Crack front tunneling during crack growth: (a) definition of a non-dimensional crack tunneling depth, (b) comparisons of measured and predicted crack tunneling depth variations with crack growth.

IV. A combined experimental and finite element study of crack slanting in a ductile material under mixed-mode loading

Abstract. Slant fracture is widely observed during crack growth in thin sheet specimens made of ductile materials, providing a good case for investigating three-dimensional criteria for mixed-mode ductile fracture. To gain an understanding of slant fracture events and to provide insight for establishing a slant fracture criterion, stable tearing fracture experiments on combined tension-torsion (nominal mixed-mode I/III) specimens and nominal Mode I Arcan specimens made of Al 2024-T3 are analyzed using the finite element method under three-dimensional conditions. Two types of finite element models are considered for the study of slant fracture: (a) combined tension-torsion specimens containing stationary, flat and slant cracks subject to loads corresponding to the onset of crack growth, and (b) stable tearing crack growth with slanting in a nominal Mode I Arcan specimen. Analysis results reveal that there exists a strong correlation between the direction of the maximum effective plastic strain ahead of a crack front and the orientation direction of slant fracture. In particular, it is observed that (a) at the onset of crack growth, the angular position of the maximum effective plastic strain around the crack front serves as a good indicator for the slant fracture surface orientation during subsequent crack growth; and (b) during stable tearing crack growth with a flat-to-slant transition, the crack growth path on each section plane through the thickness of a specimen coincides with the angular position of the maximum effective plastic strain around the crack front. The results of this study suggest that the effective plastic strain may be used as a fracture parameter for predicting the fracture surface path of stable crack growth with slant fracture.

IV.1. Introduction

A phenomenon often observed in stable tearing crack growth experiments on thin plate specimens made of ductile materials (e.g. aluminum alloys) is that an initially flat crack tends to turn and grow as a slant crack after a short flat-to-slant transition. Figure 1a shows a typical crack surface involving the development of slant fracture under nominal Mode I loading conditions. This behavior has been reported widely in fatigue experiments (Rickerby and Fenici, 1984; Zuidema and Blaauw, 1988; Zehnder, 2000), stable tearing tests (Meyn et al., 1989; Narasimhan et al., 1992; Amstutz, 1995; Mahmoud and Lease, 2003), and dynamic crack growth tests (Krafft et al., 1961).

Experiments on compact tension or C(T) specimens with initial, slant cracks have been carried out for different ductile materials, for instance, steels (Kumar and Hirth, 1991) and aluminum alloys (Manoharan, 1997). Different slant cracks were used to obtain different Mode III and Mode I ratios under remote Mode I loading conditions. These studies indicate that slant cracks tend to lower the critical value of the total mixed-mode J-integral, J_{mc}. To this end, it is worth noting that experiments on middle-crack-tension or M(T) specimens made of Al 2024-T351, conducted by Dawicke and Sutton (1994), showed that the critical crack-tip opening angle (CTOA) value measured on a specimen surface is higher in the case of a flat crack than in the case of a slant crack.

Crack-front shapes in Mode I loaded Al 2024-T351 plate specimens, recorded at different stages of crack growth, have been compared by James and Newman (2003). The optically measured fracture crack-front shapes revealed that specimens experiencing a flat-to-slant transition have much lower tunneling magnitudes than those with only flat fracture surfaces. Here the tunneling parameter defined by Dawicke and Sutton (1994), which is the normalized difference between the maximum interior crack extension and the crack extension on the specimen surface, is used to define tunneling magnitude.

Under pure tension and combined tension-torsion (mixed-mode I/III) loading conditions, experiments conducted by Sutton et al. (2001) on single-edge crack specimens made of aluminum alloy 2024-T3 suggest that the slant angle, which is the angle between the slant plane and the original flat crack plane, has a one-to-one correspondence with the ratio of a nominal shear stress, S_T, due to a remote torque load T, to a nominal tensile stress, S_P, due to a remote tension load P (Fig. 1b). For each fixed loading ratio, the slant angle initially increases with the amount of crack extension during a flat-to-slant transition and eventually achieves, more or less, a steady-state value. It is found that the slant angle decreases as the amount of torsion loading increases. When only tension is applied, the slant angle is ~38º, which is the largest slant angle. It is noted that the same slant angle is also observed in Arcan experiments, also on Al 2024-T3 specimens, by Amstutz (1995) under remote Mode I loading conditions.

Analyses of fracture surfaces of M(T) specimens made of Al 2024 have been performed by Bron et al. (2004). Comparisons of flat and slant fracture surfaces revealed that the formation of the slant plane is related to shear band localization. An earlier study by Randolph and Piascik (1995) also showed that shear lips were formed along the specimen's free surfaces at the beginning of the stable tearing process and then they grew to form a slant crack.

Based on continuous damage mechanics, a numerical study of the flat-to-slant transition was carried out by Besson et al. (2001) using the Rousselier model (Rousselier, 1987). It was assumed that crack growth was controlled by porosity and that a material failed when porosity reached a critical value. The authors made a qualitative prediction of the flat to slant transition by changing certain model parameters such as the initial plastic strain for void nucleation. However, this model overestimated the structural response and underestimated the crack growth rate. Gullerud and his coauthors (Gullerud et al., 1999) argued that the lack of agreement with experimental evidence was due to the fact that this model required a high constraint level to drive the damage process. One approach to obtain an improved prediction (Steglich and Brocks, 1998) is to use small finite elements with element size on the order of the inter-particle spacing, which is about 10-20 μm for Al 2024, a very small number.

Analytical and numerical studies of slant fracture using traditional fracture mechanics concepts have been very limited in the literature. Under linearly elastic conditions, the crack tip stress fields for plates loaded in tension and out-of-plane shear was derived by Zehnder et al. (2000) based on superposition of the stresses from in-plane and out-of-plane loads. Through an analysis of the crack-tip stress fields, the authors attempted to explain why the crack took the slant orientation.

To shed light on the underlying mechanics of slant fracture, three-dimensional finite element analyses of selected Al 2024-T3 specimen geometries with initial flat and slant cracks under nominal Mode I loading condition were carried out by Maghoub et al. (2003). For the specimen with a slant crack, the slant angle was set to 38º, which is the value from a nominal Mode I experiment of the same material (Amstutz, 1995). Comparisons of deformation and stress fields around the flat and slant crack fronts revealed that, among other observations, the von Mises effective stress ahead of a slant crack is more uniform through the plate thickness and is higher than observed in the case of a flat crack undergoing the same loading conditions. The findings in Mahgoub et al. (2003) are consistent with the observations in Bron et al., (2004). The authors indicated that the effective stress and other stress field features promote shear fracture, which is believed to be related to the formation of slant fracture.

Slant fracture usually involves mixed-mode I/III loading conditions. Due to the complexity of general mixed-mode I/III problems, analytical solutions of the 3D crack front stress and deformation fields do not exist. However, under more idealized conditions, such as linear elasticity, small scale yielding, Mode I or Mode III dominance, and/or with negligible field variations in the plate thickness direction, a limited number of studies have been published, such as those by Pan (1990), Pan and Shih (1990), Hui and Zehnder (1993) and Gao and Shih (1998).

Currently there are no fracture criteria for quantitative prediction of slant fracture and many slant fracture issues remain unresolved. For example, under combined tension-torsion loads (Sutton et al., 2001), one may ask whether is it possible (a) to predict the experimentally observed orientation of the slant fracture surface that tends to create contact and interference between the two crack surfaces instead of opening and clearance between the surfaces, and (b) to predict the experimentally observed dependence of the stable slant angle on the torsion/tension loading ratio?

The purpose of the current work is to gain a further understanding of the slant fracture phenomenon and to provide insight for establishing a slant fracture criterion for quantitative prediction of stable tearing crack growth with slant fracture. To this end, three-dimensional (3D) elastic-plastic finite element analyses of stable tearing experiments involving slant fracture are carried out. The focus will be on two types of experiments: (a) combined tension-torsion (nominal mixed-mode I/III) experiment and (b) a nominal Mode I Arcan experiment. The specimens are made of Al 2024-T3 material. It will be shown that the angular position of the maximum effective plastic strain around the crack front, which coincides with the direction of the maximum extent of the effective plastic strain contours around the crack front, correlates strongly with the orientation of the slant fracture surface and with the crack growth paths on section planes through the thickness of a specimen. Based on the analysis results, it will be argued that the effective plastic strain may be used as a fracture parameter for predicting the fracture surface orientation during slant fracture. It is believed that the findings of this study can serve as a basis for formulating a fracture criterion for predicting mixed-mode ductile fracture events under 3D conditions.

Subsequent sections are arranged as follows. In Section 2, 3D finite element models of the combined tension-torsion experiments (Sutton et al., 2001) and the Mode I Arcan (Amstutz, 1995) on Al 2024-T3 specimens are described. In Section 3, crack-front strain fields for the combined tension-torsion experiments at the onset of crack

growth, obtained under 3D, elastic-plastic and large deformation, are presented and their implications investigated. Section 4 provides the results of a 3D stable tearing crack growth simulation along an experimentally observed 3D fracture surface, of a Mode I Arcan experiment with crack slanting. Finally, a summary of the main findings of this study and concluding remarks are given in Section 5.

IV.2. 3D Finite Element Models

IV.2.1 Combined Tension-Torsion Experiments

Combined tension-torsion experiments on Al 2024-T3 specimens have been carried out by Sutton et al. (2001) to investigate stable tearing crack growth under remote mixed-mode I/III loading conditions. These experiments are analyzed in this study to gain an understanding of possible correlations between the crack-front deformation states at the onset of crack growth and the slant fracture surface orientation during subsequent crack growth.

Figure 2 shows the in-plane geometry of the plate specimen in a global Cartesian coordinate system (the specimen thickness is 2.3 mm). The specimen was fatigue pre-cracked in the LT orientation (hence the tension loading is in the rolling or longitudinal direction and the crack is parallel to the transverse direction), with an initial a/w=0.083, where a is the pre-crack length and w the width of the plate. The pin holes near the top and bottom specimen surfaces were used to clamp the specimen to a tension-torsion loading fixture consisting of a pair of loading tangs, grip plates, and a backing plate for alignment and installation (which was detached prior to the start of an experiment).

Three loading cases, S_T/S_P=0.00, S_T/S_P=1.66 and S_T/S_P=6.64, are considered in this study, where S_T is a nominal value of the maximum shear stress due to the applied torque T and S_P is a nominal value of the average normal stress due to the tensile load P, and they are given by

$$\begin{cases} S_T = 3T\,(t^{\,2}\,w)^{-1} \\ S_P = P\,(t\,w)^{-1} \end{cases} \qquad (1)$$

where t is the specimen thickness and w is the specimen width. It is noted that S_T/S_P=0.00 corresponds to a Mode I loading condition.

For illustration purposes in this and subsequent sections, Figure 3 shows a schematic drawing of a plate specimen with a slant crack and a crack-front rectangular Cartesian coordinate system in which the y axis is along the tensile loading direction and the x-y plane coincides with the specimen's mid-plane. Three of the specimen's through-thickness section planes, namely the front surface, the mid-plane, and the back surface, which correspond to, respectively, z=0.5t, 0, and -0.5t, are also noted in the figure. When the slant angle is zero the specimen contains an initially flat crack; otherwise the specimen contains an initially slant crack. A crack-front local polar coordinate system (r, θ) can be associated with a through-thickness section plane (e.g. the front surface, the mid-plane, and the back surface), as shown in Fig. 3 for the mid-plane, with r=0 at the crack front and θ=0° parallel to the positive x direction.

Actual material properties for the specimen and the loading fixture are employed. The aluminum specimen has a Young's modulus of 71.7 GPa and an initial yield stress of 344.8 MPa, while the loading fixture, which is made of steel 15-5PH (a high-strength stainless steel), has a Young's modulus of 207 GPa and an initial yield stress of 1,724

MPa. A Poisson's ratio of 0.3 is taken for both the steel and the aluminum alloy. Both materials exhibit strain-hardening behavior and the dependence of the materials' flow stress on the effective plastic strain in uniaxial tension is shown in Fig. 4. The materials are assumed to obey the J2 flow theory of plasticity.

A finite element representation of the tension-torsion specimen with a flat crack, with consideration of the four grip plates in the fixture-specimen connection region, is illustrated in Fig. 5. The mesh shown in Fig 5 is a converged mesh used for analysis. In particular, Fig. 5a provides an overall view of the finite element model. Figure 5b is a local in-plane view of the focused mesh around the crack front; the crack is not visible but it lies to the left of the center point of the mesh. In the radial direction, the element size decreases towards the crack front. In the circular direction, forty rings of elements are distributed uniformly around the crack front. Figure 5c shows a three-dimensional view of the mesh in a near-crack-front region with a radius of 4.5 mm. In the thickness direction, there are sixteen layers of elements, with a decreasing layer thickness from the plate mid-plane towards the front and back surfaces (the element size on the surface is one fifth of that in the mid-plane). This mesh consists of 26,304 twenty-node brick elements with 113,985 nodes (25,072 elements in the specimen region and 1,232 elements in the fixture region). Because of large out-of-plane deformation in the combined tension-torsion experiments, it is necessary to apply a large deformation finite element formulation. The general-purpose finite element code ANSYS was employed with the updated Langrangian method.

The specimen is loaded as follows. The bottom surface of the lower fixture/specimen region is held fixed while the top surface of the upper fixture/specimen region is loaded according to the conditions specified in Table 1, which correspond to the critical moment of the onset of stable tearing fracture. Specifically, the upper grip is rotated by an experimentally measured torque T (which is applied through a set of statically equivalent point forces) and displaced vertically by U_y that results in a reaction F_y in agreement with the measured value. The use of a large deformation formulation and the applied loading process described above have been shown (Lan et al., 2004) to be effective for modeling the thin tension-torsion specimen. It is noted that this particular loading approach for applying accurate boundary conditions is required since reliable experimental data was available only for the tensile reaction force, F_y, the applied torque, T (about the *y* axis) and the resulting torsion angle ϕ (rotation about the *y* axis). The good agreement shown in Table 1 between the predicted and measured specimen response in terms of F_y and ϕ demonstrates that the large deformation option and applied finite element loading conditions are appropriate.

IV.2.2 Mode I Arcan Experiment

As a special case of the mixed-mode I/II Arcan stable tearing crack growth experiments performed by Amstutz (1995) on Al 2024-T3 specimens, the Mode I experiment on a specimen with the LT orientation (in which the initial crack orientation is perpendicular to

Table 1 Finite element loading conditions, predicted specimen response, and test data for three tension-torsion test cases

Test Case	Top Surface Conditions	Predicted Response	Test Data
S_T/S_P=0.00	Uy=0.48 mm	Reaction Fy=37.56 KN Rotation angle $\phi = 0^o$	Reaction Fy=37.19 KN Rotation angle $\phi = 0^o$
S_T/S_P =1.66	Uy=0.28 mm T=32.06 N*m	Reaction Fy=24.85 KN Rotation angle $\phi = 10.96^o$	Reaction Fy=25.24 KN Rotation angle $\phi = 11.83^o$
S_T/S_P =6.64	Uy=-0.03mm T=42.91 N*m	Reaction Fy=8.91 KN Rotation angle $\phi = 17.24^o$	Reaction Fy=8.43 KN Rotation angle $\phi = 17.83^o$

the material's rolling direction) provides a good case for investigating the slant fracture phenomenon and is chosen for detailed analysis in the current work. In this Mode I Arcan experiment, as the specimen containing an initially flat fatigue pre-crack is loaded under remote Mode I loading conditions, the flat crack first experiences a flat-to-slant transition growth period and then grows as a slant crack with an almost constant slant angle.

Figure 6 shows the in-plane geometry of the Arcan fixture and specimen, in which the specimen has a thickness of 2.3 mm and the fixture (made of 15-5PH stainless steel) has a thickness of 19 mm. The locations of the pinholes on the outer edge of the fixture provide a range of values for the loading angle ϕ where $\phi = 0°$ corresponds to Mode-I loading and $\phi = 90°$ corresponds to Mode-II loading. The three interior holes on each of the fixture halves are used to attach the specimen to the fixture.

The crack growth event in the Arcan Mode I specimen is modeled using a nodal release technique in which the prescribed crack growth path is based on the measured fracture surface. Shown in Fig. 7 is a converged 3D finite element mesh of the fixture/specimen system used for the crack growth simulation. Since the fixture and connecting pins in the Arcan experiments are relatively rigid compared to the aluminum specimen, the fixture-specimen system is treated as one continuous solid with two regions of different thicknesses and material properties (Deng and Newman, 1999). This mesh consists of 12,101 ten-node tetrahedral elements with 21,040 nodes. The smallest element size along the crack surface is ≈ 0.2 mm.

The stable tearing crack growth process (see Fig. 7c), starting from a flat fatigue pre-crack, following a flat-slant transition region, and settling into a slant crack growth region with a slant angle ≈38^0, is simulated using CRACK3D, which is a finite element code developed at the University of South Carolina for 3D crack growth simulation using nodal release and local re-meshing options (see Zuo et al., 2004, 2005).

Crack growth along the measured fracture surface in Fig. 7c is achieved through the advancement of an assumed straight crack front (thus crack tunneling is not modeled) via a nodal release procedure, in which the crack front nodes (originally tied

together by rigid springs) are separated (released). Nodal release is performed when, based on the mixed-mode crack tip opening displacement (CTOD) criterion (Ma et al., 1999; Sutton et al., 2000), the generalized CTOD value on the front surface of the specimen and at a fixed distance behind the crack tip reaches an experimentally determined critical value. In this study, an experimentally determined critical CTOD value of 0.095 mm at 1.0 mm behind the crack tip (which corresponds to a critical CTOA value of 5.44^{o}) is used. Unlike the combined tension-torsion experiments, large out-of-plane deformation is not present in Arcan specimens, and as such, it is found that only the small-deformation option in CRACK3D is needed to properly simulate the crack growth process.

IV.3. Results for the combined tension-torsion experiments

Tension-torsion specimen models with stationary flat and stationary slant cracks have been analyzed using loading conditions corresponding to the onset of crack growth. For models containing a flat crack, the finite element analysis results will show that there is a strong correlation between the direction of the maximum effective plastic strain at the onset of crack growth and the subsequent slanting direction. This correlation will be further demonstrated by results from models with a slant crack, which suggests that the effective plastic strain may serve as a good indicator for predicting crack growth with slant fracture.

IV.3.1 Tension-Torsion Models with a Flat Crack

Effective plastic strain contours

The effective plastic strain contours on the specimen's front surface (z=t/2) just before the onset of crack growth is shown in Fig. 8 for three tension-torsion loading cases (with torsion/tension ratios S_T/S_P=0.00, 1.66 and 6.64). Besides the observation that the size of the contour extent increases with the torsion/tension ratio, the results also reveal that the orientation angle (relative to the x-axis) of the maximum extent of the effective plastic strain contours on the front surface decreases with the torsion/tension ratio. Specifically, for the contour level of 0.0001, the maximum contour extent for the pure tension case (S_T/S_P=0.00) occurs at $\theta \approx +/-46°$ relative to the x-axis, while those for the mixed tension-torsion cases the maximum $\theta \approx 37°$ (S_T/S_P=1.66) and $\theta \approx 36°$ (S_T/S_P=6.64) on the front surface occurs. On the back surface, the angles for S_T/S_P=1.66 and 6.64 are the same as those on the front surface but with negative signs, which is due to an anti-symmetry between the contour orientations on the front and back surfaces (compare, for example, Fig. 8b and Fig. 9 for the case of S_T/S_P=1.66). On the specimen's mid-plane, the effective plastic strain contours are symmetric about the x-axis and the maximum extent occurs more or less along the x-axis direction (see Fig. 10).

To make connections with experimental observations (Sutton et al., 2001), it is noted that the orientation of the slant fracture surface in a tension-torsion experiment is such that the presence of a torsion load component will tend to create crack surface contact and interference instead of opening and clearance. Specifically, for a mixed tension-torsion loading case, the subsequent slant orientation after the onset of crack growth is such that the crack path on the model specimen's front surface will tilt

upwards while the crack path on the back surface will go downwards. This is entirely consistent with the orientation of the maximum extent of the effective plastic strain contours, as shown in Fig. 8b (front surface) and Fig. 9 (back surface) for the case of S_T/S_P=1.66. Furthermore, experimental results (Fig. 1b) show that the slant angle decreases as the torsion/tension load ratio increases (the slant angle is $\theta \approx 38°$, 33.5° and 31°, respectively, for S_T/S_P=0.00, 1.66 and 6.64). This is also consistent with the numerical results that the orientation angle of the maximum extent of the effective plastic strain contours decreases on the front surface with the torsion/tension ratio.

Angular variations of the effective plastic strain field

In order to reinforce the observation that there is a strong correlation between the effective plastic strain distribution and the orientation direction of slant fracture, the angular variations of the effective plastic strain around the crack front is examined. These angular variations are given for a through-thickness section plane (e.g. the front surface, the mid-plane, and the back surface) of the specimen, in terms of the local polar coordinate θ (see Fig. 3), with r=0 at the crack front and θ=0° parallel to the positive x direction.

Figure 11 shows the angular variations of the effective plastic strain ε_p (normalized by the initial yield strain ε_0) along a circular path of radius r=1.50mm, on the mid-plane and the front and back surfaces, for three tension-torsion loading cases. It is seen from Fig. 11a that the effective plastic strain on the front surface reaches a maximum at $\theta \approx +/-45^0$, 34^0 and 30^0, respectively, for S_T/S_P=0.00, 1.66 and 6.64. Hence the absolute value of the angle at which the maximum effective plastic strain occurs on the front surface decreases as torsion increases. This trend is strongly indicative of the trend observed experimentally for the slant angle, namely, that the absolute value of the slant angle decreases as torsion increases. Specifically, experimental results showed that, after a short flat-to-slant transition, the slant angle in tension-torsion experiments is $\theta \approx 38^0$, 33.5^0 and 31^0, respectively for S_T/S_P=0.00, S_T/S_P=1.66 and S_T/S_P=6.64. For the case of S_T/S_P=0.00, the slant angle may be $\theta \approx 38^0$ or -38^0, but for cases with a torsion loading component (e.g. S_T/S_P=1.66 and S_T/S_P=6.64), the slant angle is always positive, which confirms the trend observed for the predicted maximum effective plastic strain angles on the front surface.

Consistent with the positions of the maximum effective plastic strain on the front surface, those on the back surface have the same but opposite angular values (see Fig. 11c). As such, if these angles are indicators of where the crack path will tend to turn on the front and back surfaces, these indicators will correctly predict the qualitative trends exhibited by the subsequent slant fracture orientations seen from the experimental results: (a) when torsion is present, the slant orientation will tend to created crack surface contact and interference instead of crack opening and clearance; and (b) the slant angle decreases as the torsion/tension ratio increases. The observation (see Fig. 11b) that the angle at which the maximum effective plastic strain occurs on the specimen's mid-plane is 0^o (for S_T/S_P=0.00 and S_T/S_P=1.66) or somewhere around 0^o (for S_T/S_P=6.64) is also consistent with the predicted overall slant orientation through the specimen thickness.

The above comparisons demonstrate again that there is a strong correlation between the effective plastic strain distribution and the direction of crack growth with slant fracture. This effective plastic strain argument will be discussed again in Section 3.2.

Other stress and strain field variations

For completeness and comparison, other relevant field variations at the onset of crack growth are included here. First, the radial variations of the stress constraint σ_m/σ_e (which is the ratio between the mean stress σ_m and the von Mises effective stress σ_e) and the effective plastic strain ε_p will be presented, and then the angular variations of σ_m, σ_e and σ_m/σ_e will be given.

Figure 12 shows the radial variations of the constraint σ_m/σ_e along the direction $\theta=0°$ ahead of a flat crack on the front surface, mid-plane, and the back surfaces, with three tension-torsion loading cases. It is seen that, in all loading cases, the mid-plane constraint value (Fig. 12b) rises quickly as the crack front is approached and, near the crack front, it is much higher than those on the front and back surfaces (Figs. 12 a, c, which show almost identical variations, suggesting some kind of constraint symmetry about the mid-plane). It is also observed that the constraint value decreases as the torsion/tension ratio increases.

Figure 13 describes the radial variations of the effective plastic strain (normalized by the initial yield strain ε_0) along $\theta=0°$ on the front surface (the front and back surfaces have identical variations) and on the mid-plane. It is seen that, close to the crack front (when $r<0.3$mm), ε_p increases rapidly as the crack front is approached and as the torsion/tension ratio increases, which is especially true on the front and back surfaces.
Figures 14, 15, and 16 gives the angular variations of the von Mises effective stress, the mean stress, and the constraint, respectively, along $r=1.50$mm for the mid-plane and the front and back surfaces for three loading cases. Based on the data in the figures, two observations are noted. First, the effective stress (Fig. 14) is more or less flat ahead of the crack front, which suggests that it may not serve well as a parameter for predicting the crack path. Second, the mean stress (Fig. 15) and the constraint (Fig. 16) have a peak value somewhere around $\theta=0$. More specifically, for $S_T/S_P=0.00$, the peak value occurs exactly at $\theta=0°$ on the mid-plane and front and back surfaces, and for $S_T/S_P=1.66$ and 6.46, it occurs at $\theta=0°$ only on the mid-plane.

IV.3.2 Tension-Torsion Models with a Slant Crack

In the preceding section it has been argued that the effective plastic strain distribution at the onset of crack growth in tension-torsion specimens containing a flat crack provides a good indicator for the orientation of the subsequent slant fracture surface. In this section, further evidence will be provided for this argument. To this end, one modification is made to the tension-torsion specimens in the 3D finite element analyses performed earlier: the flat crack is replaced with a slant crack while all other input data, such as material properties, geometrical dimensions, and boundary conditions are kept the same. In doing so, it is hoped that the following issues can be clarified: (1) If the slant angle of the stationary slant crack equals the experimentally measured slant angle, will the effective plastic strain distribution indicate a constant slant angle during subsequent crack growth? (2) If the slant angle is smaller than the measured value, will the effective plastic strain distribution indicate an increase in the slant angle during

subsequent crack growth? (3) If the slant angle is larger than the measured value, will the effective plastic strain distribution indicate a decrease in the slant angle during subsequent crack growth?

To address these questions, 3D finite element analyses for tension-torsion specimen models containing stationary slant cracks have been carried out. The slant crack models have the same material, geometry and applied remote loading conditions as those with flat cracks except that the crack surface in the slant crack model forms a slant angle, α, with that of the flat crack surface (see Fig. 3). For each of the three tension-torsion loading cases S_T/S_P=0.00, 1.66, and 6.64 (for which the measured slant angles are, respectively, $\theta \approx 38^0$, 33.5^0 and 31^0), five slant angles have been considered: 0°, 10° and 20° (which are smaller than the measured slant angle), 55° (which is larger than the measured slant angle), and the measured slant angle itself. The results are presented below. Since conclusions from the results for the three tension-torsion cases are the same, only those for the case of S_T/S_P=1.66 are reported here.

Angular variations of the effective plastic strain field

Figure 17 shows the angular variations of the effective plastic strain along r=1.50mm on the front surface (Fig. 17a) and on the middle plane (Fig. 17b), for the case of S_T/S_P=1.66 and for the five slant angle values (α=0°, 10°, 20°, 33.5°and $55°$). It is clearly seen that, when the slant angle equals 0°, 10°, or 20°, which are smaller than the experimentally observed slant angle of $33.5°$, the angle at which the maximum effective plastic strain occurs on the front surface (Fig. 17a) is positive (it is worth noting that the corresponding angle on the back surface the same value but opposite sign). According to the argument made in the preceding section, this would suggest that in the subsequent crack growth, the crack path on the front surface will curve upwards while that on the back surface will go downwards, thus resulting an increase in the slant angle. Furthermore, it is observed that the angle for the maximum effective plastic strain will decreases as the slant angle gets closer to the measured value. Hence, based on the effective plastic strain argument, the predicted increase in the slant angle for subsequent crack growth will be smaller when the difference between the stationary slant angle and the measured angle is smaller.

On the other hand, when the slant angle is 55°, which is larger than the measured slant angle of 33.5^0, the angle at which the maximum effective plastic strain occurs is negative on the front service (and positive on the back surface). Based on the effective plastic strain argument, this would suggest that the crack path in subsequent crack growth will turn downwards on the front surface and upwards on the back surface, resulting in a decrease in the slant angle. It is interesting to note that, on the mid-plane (Fig. 17b) the angle at which the maximum effective plastic strain occurs is basically zero regardless of the slant angle, which suggests that the crack path on the mid-plane will stay on the straight path, a result that is consistent with experimental observations.
Another important observation is that, when the slant angle equals the measured value of $33.5°$, the angle at which the maximum effective plastic strain occurs is always zero on all surfaces (see, e.g., Fig. 17), regardless of the tension-torsion ratio. This is further confirmed by Fig. 18, which shows that the maximum effective plastic strain peak is always located at θ=0° on all section planes through the thickness of the specimen.

Based on the effective plastic strain argument, this set of observations would suggest that the crack path on each section plane through the specimen thickness will not change direction. Thus the slant angle during subsequent crack growth will stay constant, which is confirmed by the tension-torsion experimental results.

Table 2 Slant-angle dependence of the angle at which the maximum effective plastic strain occurs on the front and back surfaces for three tension-torsion loading cases (α^* denotes the experimentally observed stable slant angle for the three loading cases).

S_T/S_P	Slant angle (Degree)									
	0°		10°		20°		α^*		55°	
	Front	Back	Front	Back	Front	Back	Front	Back	Front	Back
0.00	±45	±45	40.5	-40.5	31.5	-31.5	0	0	-31.5	31.5
1.66	34	-34	27	-27	13.5	-13.5	0	0	-40.5	40.5
6.64	30	-30	18	-18	9	-9	0	0	-54	54

A summary of the predicted slant-angle dependence of the angle at which the maximum effective plastic strain occurs on the front and back surfaces for all three tension-torsion loading cases is given in Table 2. This table and the analyses presented in the preceding paragraphs clearly demonstrate that the effective plastic strain distribution provides a good indicator for predicting the fracture surface paths during stable crack growth with slant fracture. This argument will be further supported by findings from a finite element simulation of stable crack growth along an experimentally observed slant fracture surface in a nominally Mode I loaded Arcan specimen, which will be described in Section 4.

Other stress and strain field variations

For comparison, the radial variations of constraint and effective plastic strain ahead of the slant crack front (at the onset of crack growth) are included for the case of S_T/S_P=1.66. Figure 19 shows the radial variations of the constraint along θ=0° on the front surface and the mid-plane, around slant cracks with various slant angles (variations on the back surface are not shown because they are basically the same as those on the front surface). It is seen that the constraint level on the front surface (Fig. 19a) is always lower than 0.6, while on the mid-plane (Fig. 19b) it rises quickly (with the exception of α=55°) as the crack front is approached. Also on the mid-plane, constraint decreases as the slant angle increases. Except for the case α=55°, the constraint level on the mid-plane is always greater than that on the front surface (Fig. 19a).

Figure 20 presents the radial variations of the effective plastic strain along θ=0° around slant cracks with various slant angle; variations on the back surface are identical to those on the front surface (Fig. 20a). Variations on the mid-plane (Fig. 20b) are supplemented with a closer view near the crack front (Fig. 20c). As can be seen from Figs. 20a and c, the effective plastic strain near the crack front increases when the slant

angle increases from 0° to 33.5° (which is the measured slant angle for S_T/S_P=1.66), and its value decreases when the slant angle is 55°.

IV.4. Results for the Mode I Arcan Experiment

Results presented in Section 3 are from finite element models containing stationary, flat and slant cracks subjected to loading conditions corresponding to the onset of stable tearing crack growth. Effective plastic strain distributions around the stationary crack fronts are correlated to the orientation of slant fracture surface in the subsequent crack growth events.

To further establish the correlation between slant fracture and the effective plastic strain and lay a solid foundation for developing a criterion for predicting slant fracture, this section focuses on results from finite element simulations of an actual stable tearing crack growth event involving slant fracture, as reported by Amstutz (1995) on an Al 2024-T3 specimen for a Mode I Arcan experiments, in which an initially flat fatigue pre-crack turns into a slant crack as the crack front advances. Figure 7 shows the finite element model for this specimen. The model contains a prescribed crack path based on measurements of the fracture surface profile after the experiment. The stable tearing crack growth process is simulated using CRACK3D (see Zuo et al. 2004) using a nodal release option so that the evolution of the effective plastic strain field variations can be captured and examined in detail as the crack undergoes flat-to-slant transition.

Figure 21 provides nine snapshots abstracted from simulation movies of the fracture event as seen on the front surface, mid-plane, and the back surface, revealing the evolution of the effective plastic strain contours on (a) the front surface, (b) the mid-plane, and (c) the back surface, with crack extension increments (1) $\Delta a = 2.0\ mm$, (3) $\Delta a = 4.0\ mm$ and (3) $\Delta a = 6.0\ mm$. For example, Fig. 21.b2 shows the effective plastic strain contours on the mid-plane when the crack has advanced 2 mm. The white line in each figure represents the actual crack path on each section plane, which turns downwards on the front surface, stays almost straight on the mid-plane, and moves upwards on the back surface. These figures clearly demonstrate that, as the crack advances, the crack path on each section plane basically follows the direction of the maximum extent of the effective plastics strain contours.

Figure 22 presents the angular variations of the effective plastic strain along r=1.5 mm on the front surface, mid-plane, and the back surface for various amounts of crack extension from $\Delta a = 0.00\ mm$ to $\Delta a = 8.00\ mm$. Several important observations can be made from these figures. First, each angular variation curve on the mid-plane (Fig. 22b) has only one maximum and it always occurs at about θ=0°, which is consistent with the observation that the crack path on the mid-plane is always along the direction of θ=0° (i.e. the crack path stays straight). Second, except at the onset of crack growth (i.e. $\Delta a = 0.00\ mm$), each angular variation on the front and back surface has only one maximum, which occurs at an angle that is negative or approximately 0° on the front surface and is positive or approximately 0° on the back surface. Third, the maximum value of the effective plastic strain increases as Δa increases and the absolute value of the angle associated with the maximum value decreases gradually and eventually settles down to 0° as the crack experiences the flat to slant transition (the flat-to-slant transition region is about 4 mm, as shown in Fig. 7c) and stays on the stable slant fracture surface. That is, as the crack grows the direction of the maximum effective

plastic strain on each section plane becomes more and more aligned with the crack path direction. Stated more explicitly, the direction of the maximum effective plastic strain on each section plane always points towards the correct crack growth direction.

The second and third observations from Fig. 22 are expressed quantitatively in Table 3, which lists the direction (the angle) of the maximum effective plastic strain on the three section planes for crack extension increments from $\Delta a = 0.00\ mm$ to $\Delta a = 8.00\ mm$. The double values (i.e. θ ≈ +/-45°) for the front and back surfaces at the onset of crack growth are expected because of a mathematical bifurcation for crack slanting for a specimen containing a perfectly flat crack under Mode I loading conditions. In practice, the actual crack slanting direction is affected by imperfections. For example, the initial fatigue pre-crack is probably not perfectly flat, that is, the crack surface may have an initial slant angle, leading to a unique direction for the maximum effective plastic strain at the onset of crack growth. To see this, consider the case in which the initial fatigue crack surface has an exaggerated initial slant angle of $-10°$. Then a unique maximum effective plastic strain direction of about -36° (instead of θ ≈ +/-45°) will be observed for the front surface. Of course, if a smaller initial slant angle is used, the unique maximum effective plastic strain direction will be closer to θ ≈ -45° on the front surface.

Table 3 Direction of the maximum effective plastic strain on the three section planes for $\Delta a = 0.00\ mm$ to $\Delta a = 8.00\ mm$.

Crack extension (mm)	Front surface (degree)	Mid-plane (degree)	Back surface (degree)
0.00	± 45	0	± 45
1.00	-31.5	-1	40.5
2.00	-25	-5	17
3.00	-7	-5	9
4.00	-4	1	3
5.00	1	2	3
6.00	0	1	0
7.00	0	0	0
8.00	0	0	0

A more visually convincing representation of the above observations can be seen from Fig. 23, which plots the variation of an angle θ^* with crack extension on the front surface (Fig. 23a), the mid-plane (Fig. 23b) and the back surface (Fig. 23c). The angle θ^* is relative to the x-axis and is positive if counterclockwise. In the case of experimental data, the angle represents the crack growth direction (the kink angle). In the case of simulation data, two sets of values are denoted by θ^*: (a) the angular position around the crack tip (at r=1.5 mm away from the crack tip) where the maximum ε_p occurs, and

(b) the direction with the maximum radial extent of ε_p contours. This figure clearly illustrates the equivalence between the direction of the maximum extent of the effective plastic strain contours and the angle at which the maximum effective plastic strain occurs, and the strong correlation of the maximum effective plastic strain angle with the crack growth path on each section plane and hence with the overall orientation of the slant fracture surface. Taken together, these observations and previous findings point to the conclusion that the effective plastic strain ahead of a crack front provides a good indicator for predicting the direction of crack growth path on each section plane through the thickness of a specimen, and hence, for predicting the overall orientation of the slant fracture surface.

IV.5. Summary and concluding remarks

The phenomenon of slant fracture in several combined tension-torsion specimens and in a nominal Mode I Arcan specimen, all made of Al 2024-T3, has been studied using the finite element method.

For the tension-torsion specimens, 3D finite element models containing stationary, flat and slant cracks subject to loads at the onset of crack growth have been analyzed under elastic-plastic and large deformation conditions. Results show that the direction of the maximum effective plastic strain at the onset of crack growth strongly correlates with the orientation of the slant fracture surface during subsequent stable tearing crack growth.

For the nominal Mode I Arcan specimen, a 3D finite element model containing a flat fatigue pre-crack and a measured slant fracture surface for the subsequent stable tearing crack growth path has been used to simulate the actual slant fracture process in the specimen. Simulation results confirm the findings from the tension-torsion experimental analyses and further demonstrates that the direction of the maximum effective plastic strain (or the direction of the maximum extent of the effective plastic strain contours) provides a good indicator for the direction of the crack growth path on section planes through the thickness of the specimen, and hence with the overall orientation of the slant fracture surface.

The findings of this study suggest that the direction of the maximum effective plastic strain may be utilized as an effective parameter for predicting the slant fracture orientation. While these findings contribute to the understanding of mechanics issues in slant fracture and may provide a basis for formulating a 3D mixed-mode fracture criterion for predicting crack growth events in ductile materials, much work still remains to be done. For example, in addition to the effective plastic strain, stress constraint is also known to be a key parameter in controlling ductile failure processes (e.g. McClintock, 1968; Rice and Tracey, 1969; Hancock and Mackenzie, 1976; Walsh et al., 1989; Bao and Wierzbicki, 2004). An important open issue is the role of the dependence of the critical effective plastic strain on the stress constraint level in the prediction of ductile crack growth events. It is hoped that the findings presented in this paper will offer useful insights for further work in this research area.

IV.6.References

Amstutz, B. E. (1995). Characterization of mixed-mode stable tearing in thin sheet 2024-T3 aluminum alloy. Master thesis, University of South Carolina, Columbia, SC 29208.

ANSYS Finite Element Code, ANSYS, Inc. Canonsburg, PA.

Bao, Y. and Wierzbicki, T. (2004). A comparative study on various ductile crack formation criteria. *Journal of Engineering Materials and Technology* **126**, 314-324.

Besson, J., Brocks, W., Chabanet, O. and Steglich, D. (2001). Ductile rupture of aluminum sheet materials. *European Journal of Finite Element* **10,** 401-415.

Bron, F., Besson, J. and Pineau, A. (2004). Ductile rupture in thin sheets of two grades of 2024 aluminum alloy. *Materials Science and Engineering A* **380,** 356-364.

Dawicke D. S., Sutton M. A. (1994). CTOA and crack tunneling measurements in thin sheet 2024-T3 aluminum alloy. *Experiment Mechanics* **34**, 357–368.

Deng, X. and Newman, J. C. (1999). A study of some issues in stable crack growth simulations. *Engineering Fracture Mechanics* **64,** 291-304.

Gao, X. and Shih, C.F. (1998). A parametric study of mixed-mode I/III ductile fracture in tough materials under small scale yielding. *Engineering Fracture Mechanics* **60,** 407-420.

Gullerud, A., Dodds, R., Hampton, R. and Dawicke, D. (1999). Three dimensional modeling of ductile crack growth in thin sheet metals: computational aspects and validation. *Engineering Fracture Mechanics* **63,** 347–373.

Hancock, J.W. and Mackenzie, A.C. (1976). On the mechanisms of ductile failure in high-strength steels subjected to multi-axial stress-states. *Journal of the Mechanics and Physics of Solids* **24**, 147-169.

Hui, C.Y. and Zehnder, A.T. (1993). A theory for the fracture of thin plates subjected to bending and twisting moments. *International Journal of Fracture* **61.** 211-229.

James, M. A. and Newman, J.C. (2003). The effect of crack tunneling on crack growth: experiments and CTOA analyses. *Engineering Fracture Mechanics* **70,** 457-468.

Krafft, J.M., Sullivan, A.M. and Boyle, R.W. (1961). Effect of dimensions on fast fracture instability of notched sheets. *Proceedings of the Crack Propagation Symposium*, Cranfield, UK, Vol. 1., 1961.

Kumar, A.M. and Hirth, J.P. (1991). Mixed-Mode I/III fracture testing. *Scripta Metallurgica et Materialia* **25,** 985-990.

Lan, W., Deng, X., Sutton, M. A., Zuo, J. and Cheng, C. S. (2004). Three-dimensional finite element analyses of stable ductile fracture tests. *Proceeding of International Conference on Fracture and Damage of Advanced Materials*, Hangzhou, China, 216-226.

Ma, F., Deng, X., Sutton, M. A. and Newman, J. C.. “A CTOD-based mixed-mode fracture criterion,” *Mixed-Mode Crack Behavior, ASTM STP* 1359, K. J. Miller and D. L. McDowell, Eds., American Society for Testing and Materials, West Conshohocken, PA, 1999, pp. 86-110.

Mahgoub, E., Deng, X., and Sutton, M. A. (2003).Three-dimensional stress and deformation fields around flat and slant cracks under remote Mode I loading conditions.

Engineering Fracture Mechanics **70,** 2527-2542.

Mahmoud, S. and Lease K. (2003). The effect of specimen thickness on the experimental characterization of critical crack-tip-opening angle in 2024-T351 aluminum alloy. *Engineering Fracture Mechanics* **70**, 443-456.

Manoharan, M. (1997). Development of a mixed-mode fracture mechanism map and its extension to mixed-mode fracture. *Recent advances in fracture, proceedings of a symposium held at the Annual Meeting of the Minerals, Metals and Materials Society,* 373-384.

McClintock, F. A. (1968). A criterion of ductile fracture by the growth of holes. *Journal of Applied Mechanics* **35**, 363-371.

Meyn, D. A., Webb, T. W. and Aifantis, E. C. (1989). Hydrogen-assisted cracking studies of 4340 steel by using the optical method of caustics. *Engineering Fracture Mechanics* **33**, 913-925.

Narasimhan, R., Rosakis, A.J. and Moran, B. (1992). A three-dimensional numerical investigation of fracture initiation by ductile failure mechanisms in a 4340 steel. *International Journal of Fracture* **56,** 1-24.

Pan, J. (1990). Asymptotic analysis of a crack in a power-law material under combined in-plane and out-of-plane shear loading conditions. *Journal of the Mechanics and Physics of Solids* **38,** 133-159.

Pan, J. and Shih, C.F. (1990). Elastic-plastic analysis of combined mode I and mode III crack-tip fields under small-scale yielding conditions. *Journal of the Mechanics and Physics of Solids* **38,** 161-181.

Randolph, L.W, and Piascik, R. S. (1995). Three-dimensional crack growth assessment by microtopographic examination. *ASTM STP 1256 on Fracture Mechanics,* 303–318.

Rice, J.R. and Tracey, D.M. (1969). On the ductile enlargement of voids in triaxial stress fields. *Journal of the Mechanics and Physics of Solids* **17**, 201-217.

Rickerby, D.G. and Fenici, P. (1984). Fatigue crack growth in thin section type 316 stainless steel. *Engineering Fracture mechanics* **19**, 585-599.

Rousselier, G. (1987). Ductile fracture models and their potential in local approach of fracture. *Nuclear Engineering and Design* **105,** 97–111.

Steglich,D. and Brocks, W. (1998). Micromechanical modeling of damage and fracture of ductile materials. *Fatigue & Fracture of Engineering Materials and Structures* **21,** 1175–1188.

Sutton, M.A., Helm, J.D. and Boone, M.L. (2001). Experimental study of crack growth in thin sheet 2024-T3 aluminum under tension-torsion loading. *International Journal of Fracture* **109,** 285-301.

Sutton, M. A., Deng, X., Ma, F., Newman, J. C. and James, M. **(**2000). Development and application of a crack tip opening displacement-based mixed mode fracture criterion. *International Journal of Solids and Structures* **37,** 3591-3618.

Sutton, M. A., Zhao, W., Boone, M. L., Reynolds, A. P. and Dawicke, D. S. (1997) Prediction of crack growth direction for mode I/II loading using small-scale yielding and void initiation/growth concepts. *International Journal of Fracture* **83**, 275–290.

Walsh, J.A., Jata, K.V. and Starke, E.A., Jr. (1989). The influence of Mn dispersoid content and stress state on ductile fracture of 2134 type Al alloys. *Acta*

Metall. **37**, 2861-2871.

Zehnder A. T., Viz, M. J. and Potdar, Y. (2000). Fatigue fracture in plates in tension and out-of-plane shear. *Fatigue & Fracture of Engineering Materials and Structures* **23**, 403-415.

Zuidema, J. and Blaauw, H.S. (1988). Slant fatigue crack growth in Al 2024 sheet material. *Engineering Fracture mechanics* **29**, 401-413.

Zuo, J., Deng, X. and Sutton, M.A. (2004). Computational Aspects of 3D Crack Growth Simulations. Paper # IMECE 2004-60699, Proc. of 2004 ASME International Mechanical Engineering Congress, Nov. 13-20, 2004, Anaheim, CA.

Zuo, J., Deng, X. and Sutton, M.A. (2004). Advances in Tetrahedral Mesh Generation for Modeling of Three-dimensional Regions with Complex, Curvilinear Crack Shapes. *International Journal for Numerical Methods in Engineering* **63**, 256-275, 2005.

IV.7. Figures

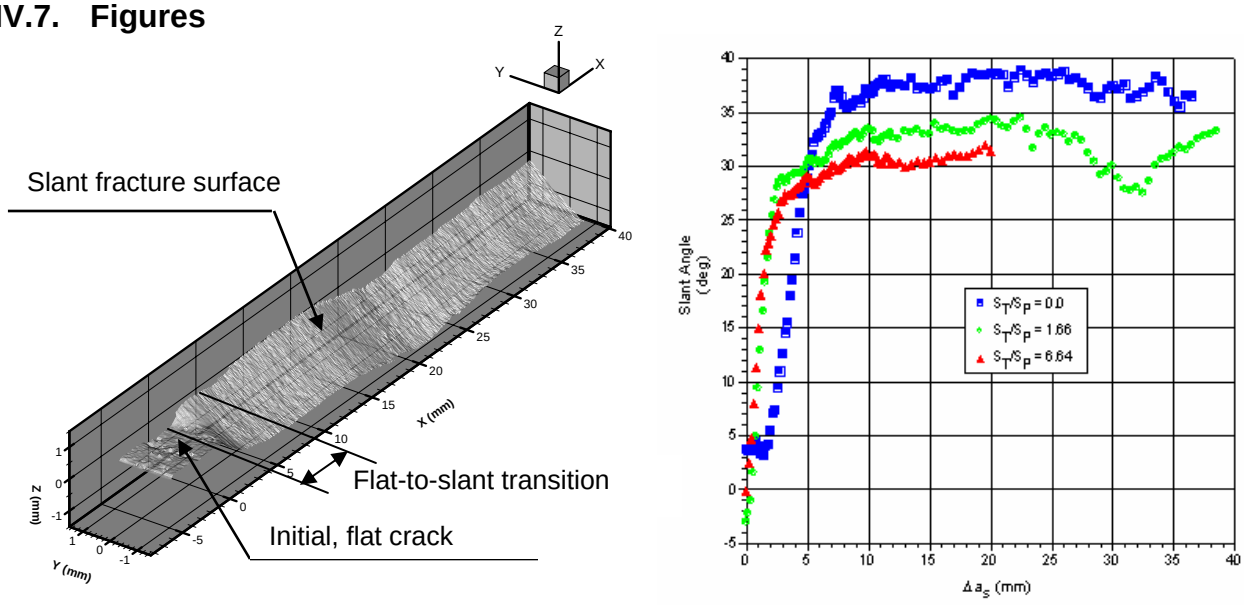

(a) (b

Fig. 1 (a) A typical slant fracture surface showing an initially flat crack surface and a flat-to-slant transition region, and (b) evolution of slant angle during combined tension-torsion tests in Al 2024-T3 specimens (Sutton, et al., 2001), as a function of the amount of crack

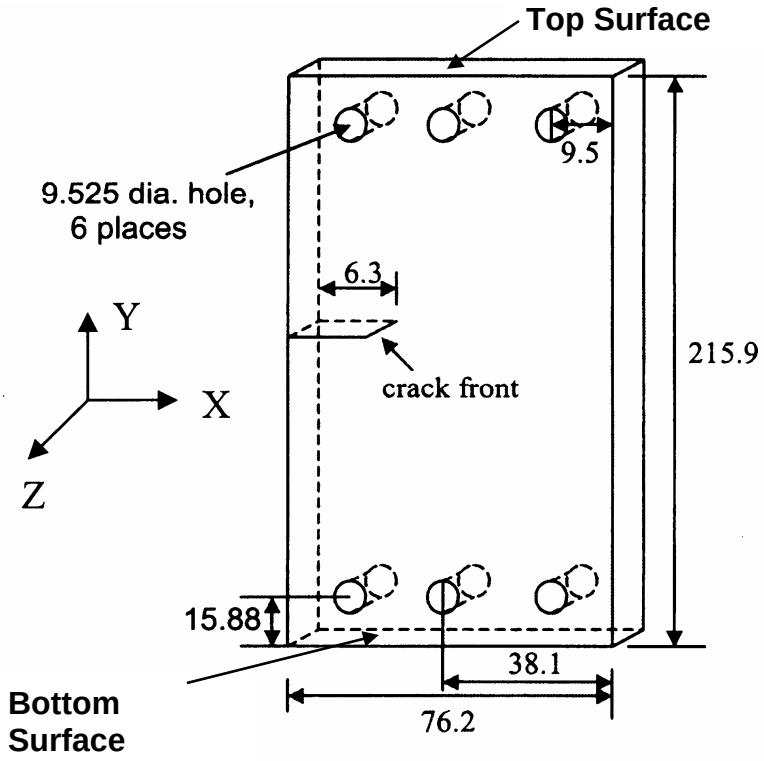

Fig. 2 Combined tension-torsion test specimen geometry (all dimensions in mm)

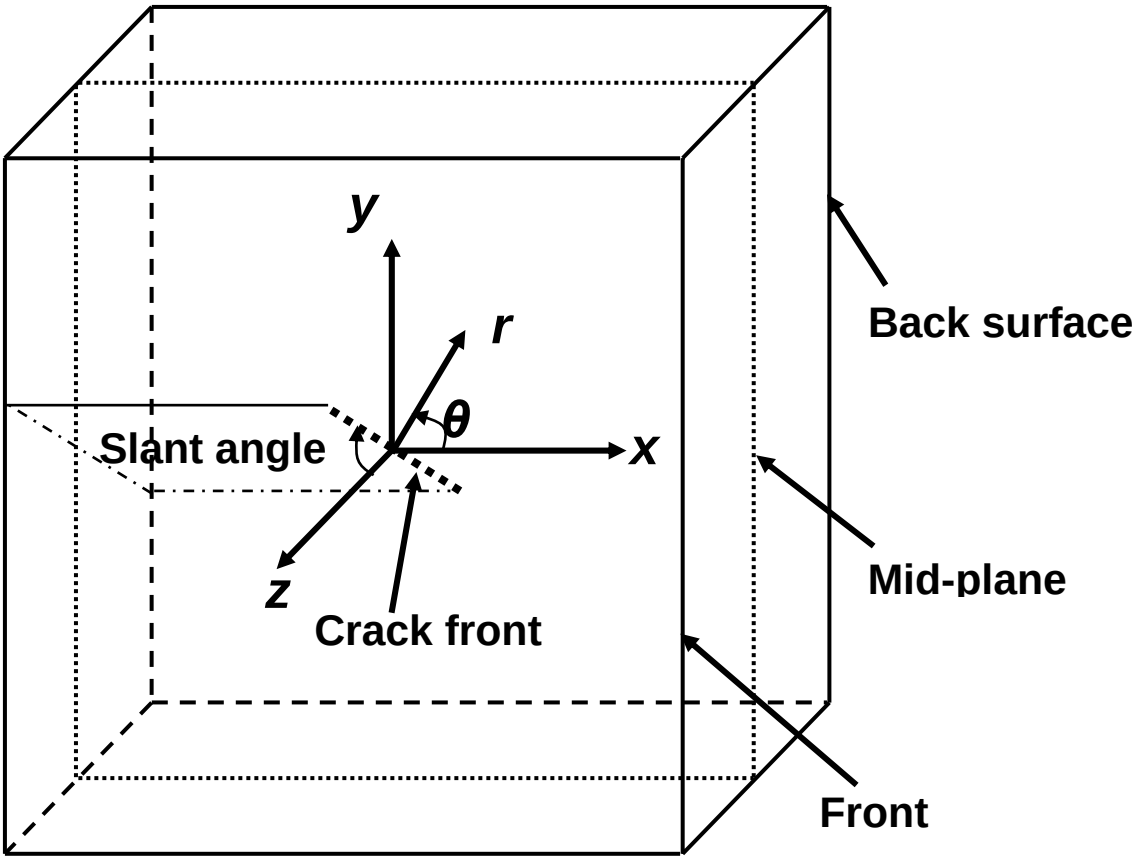

Fig. 3 A schematic of a plate specimen showing a slant crack, a crack-front coordinate system, and a local polar coordinate system.

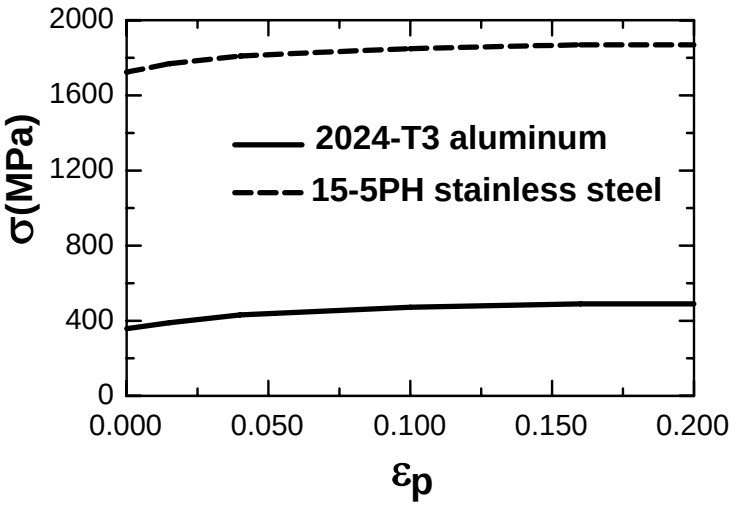

Fig. 4 Strain hardening curves for the specimen (Al 2024-T3) and fixture (15-5PH stainless steel)

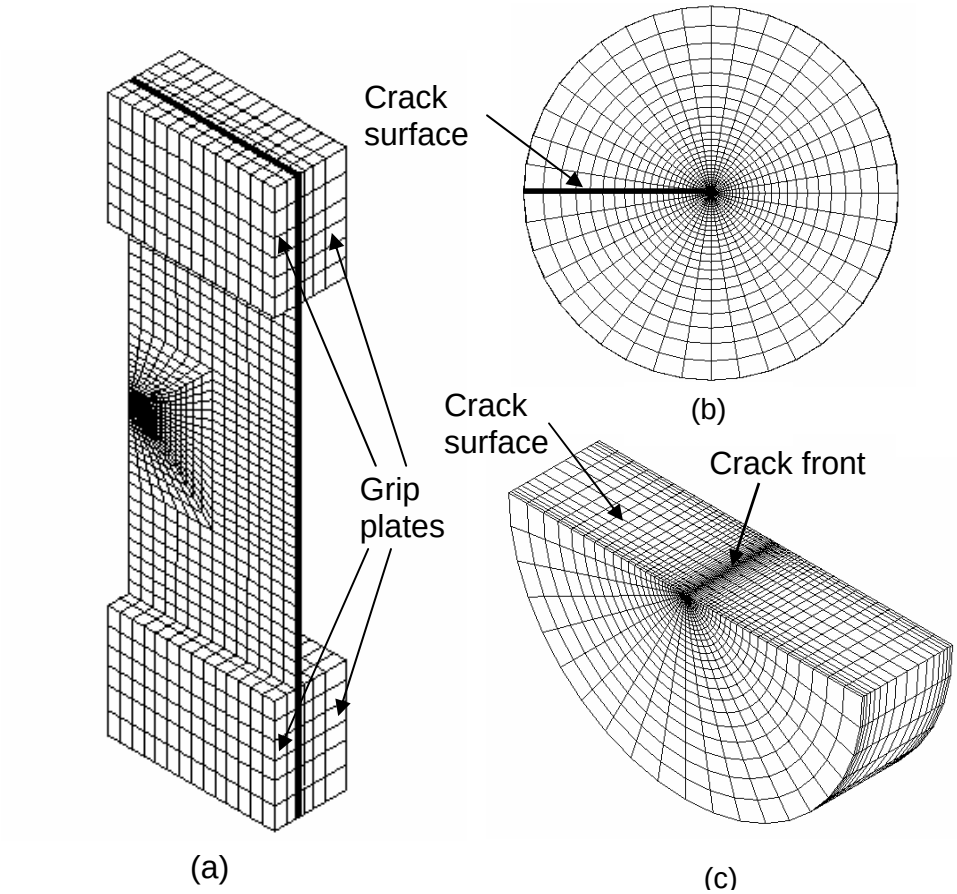

Fig. 5 A converged finite element mesh for the tension-torsion specimen: (a) a global view, showing four grip plates, (b) a local in-plane view of the focused mesh around the crack front, (c) a three-dimensional view of the mesh in a near-crack-front region.

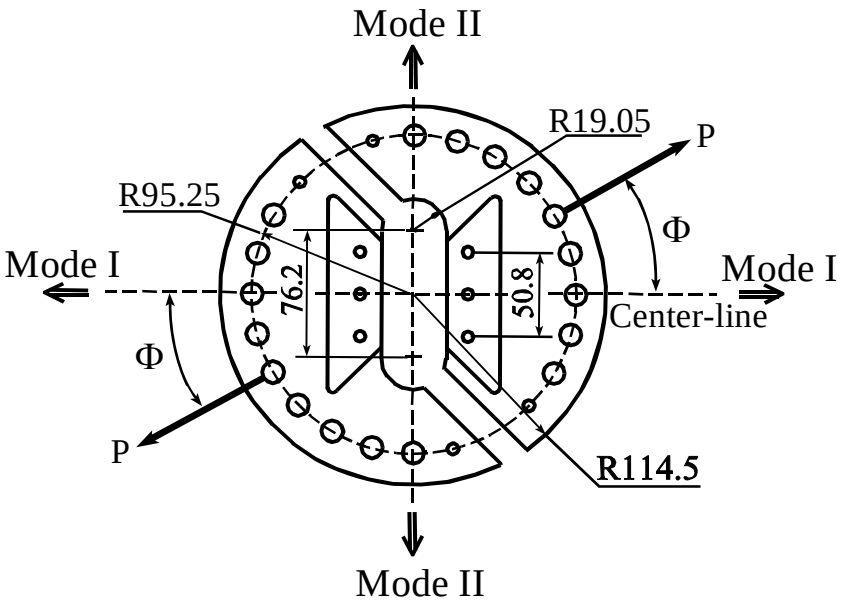

(a)

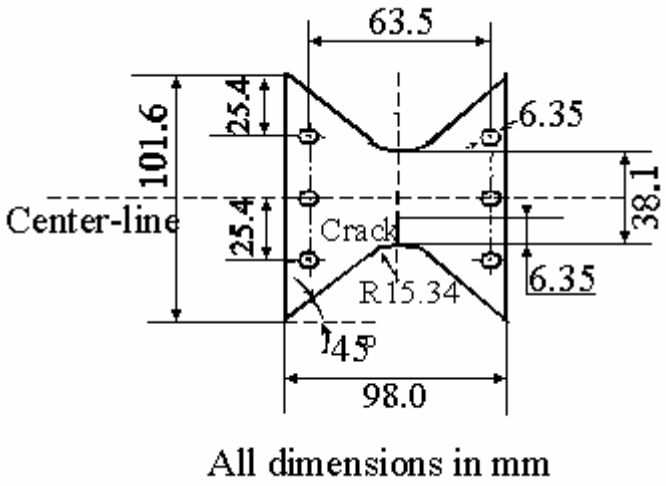

(b)

Fig. 6 In-plane geometry of the Arcan fixture and specimen: (a) fixture; (b) specimen.

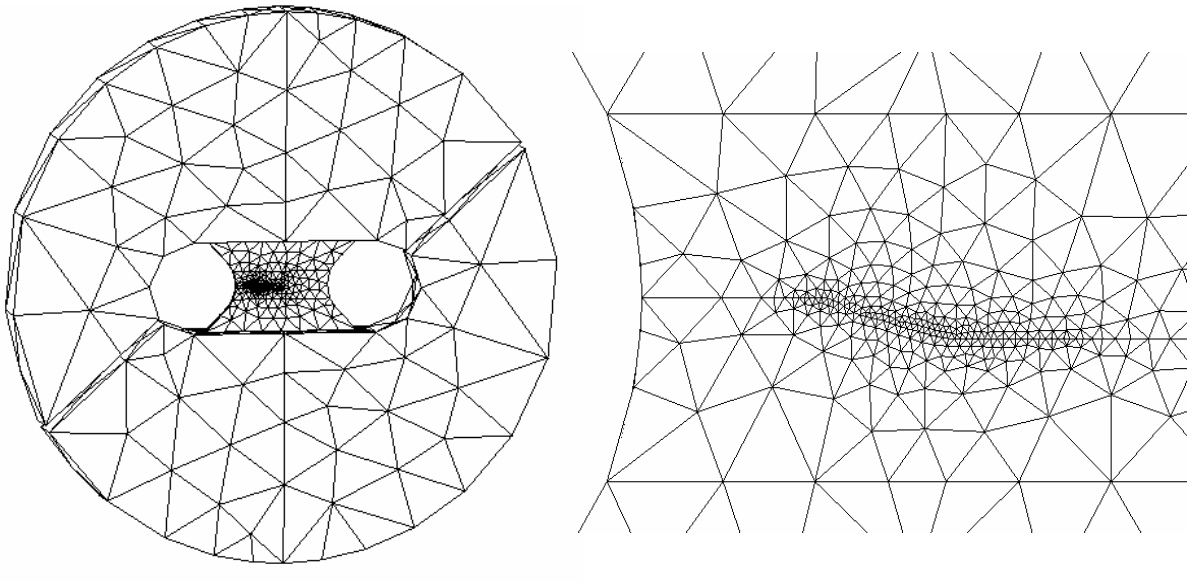

(a) (b)

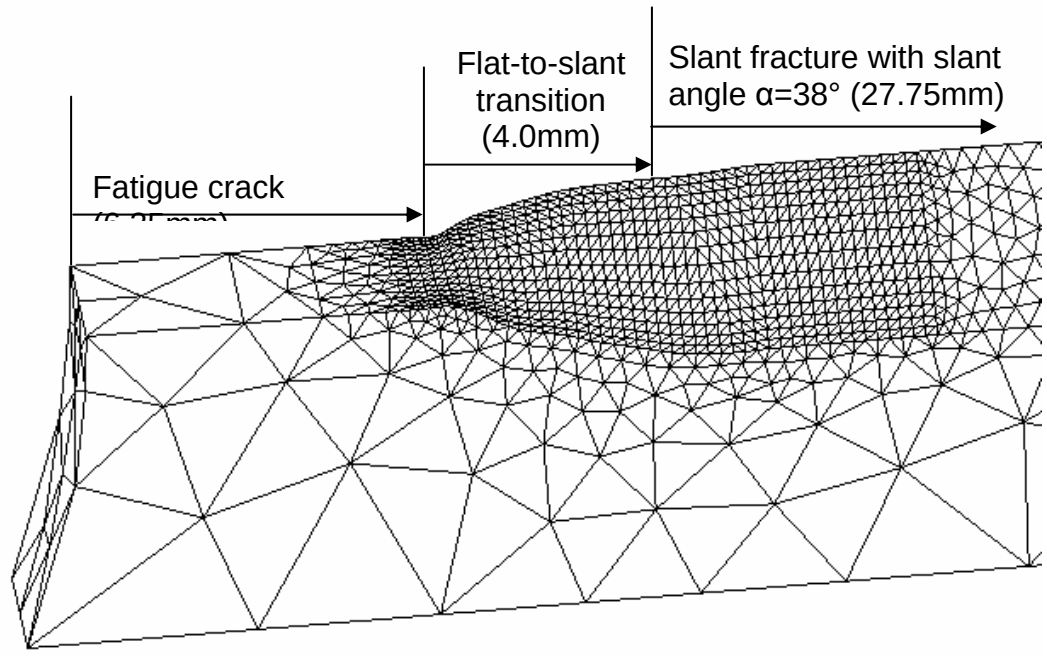

(c)

Fig. 7 Finite element mesh for an Arcan LT specimen loaded in Mode I (viewed from the front): (a) the global mesh, (b) a local view focusing on the crack path region, and (c) a local view showing different regions and their dimensions of the fracture surface along a measured flat-slant crack growth path.

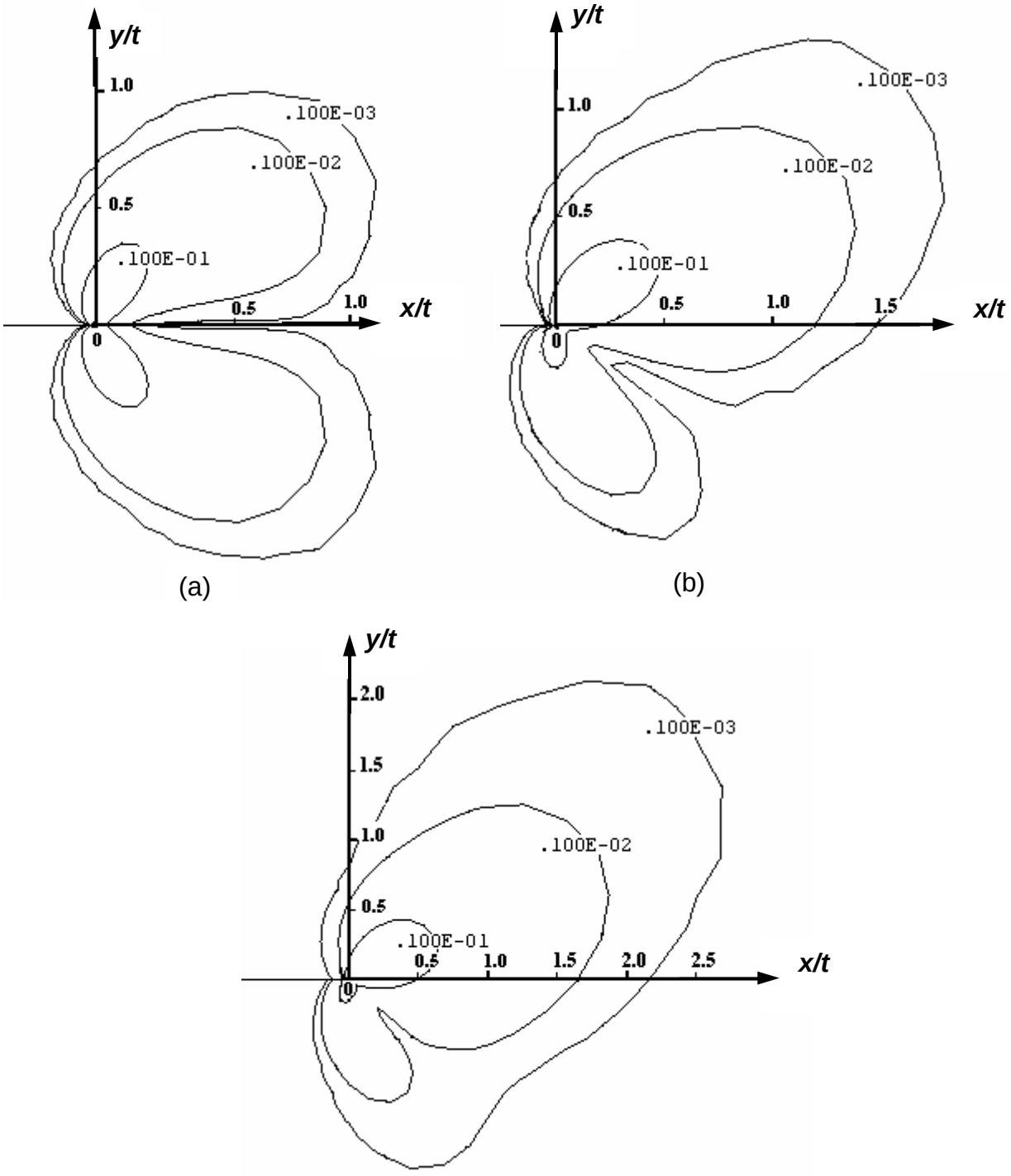

Fig. 8 Effective plastic strain contours on the specimen front surface for three tension-torsion loading cases: (a) $S_T/S_P=0.00$ (b) $S_T/S_P=1.66$ (c) $S_T/S_P=6.64$.

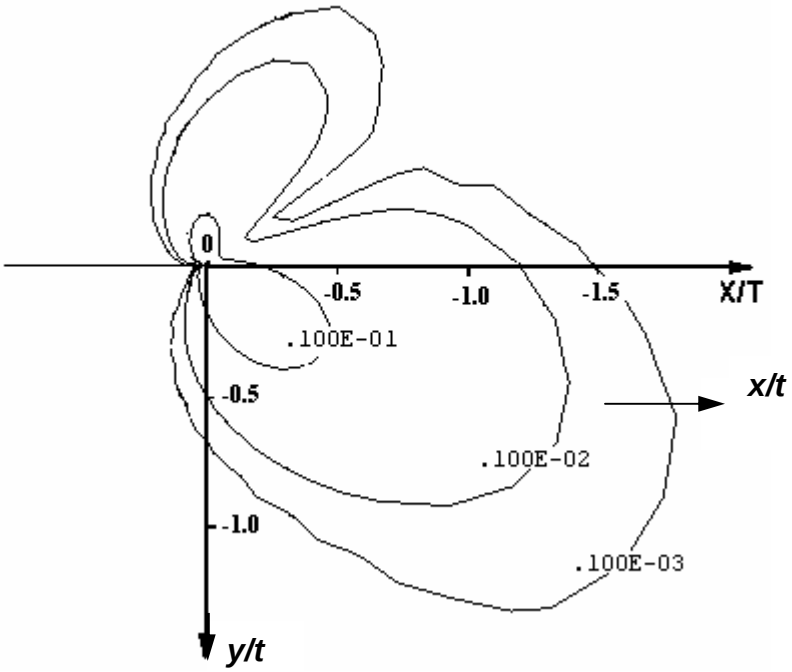

Fig. 9 Effective plastic strain contours on the specimen back surface, for the tension-torsion loading case of S_T/S_P=1.66.

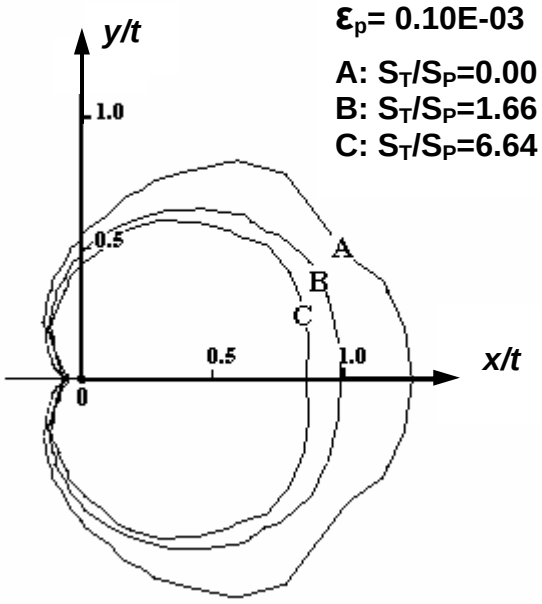

Fig. 10 Effective plastic strain contours for a strain level of 0.10e-3, on the specimen middle plane, for three tension-torsion loading cases.

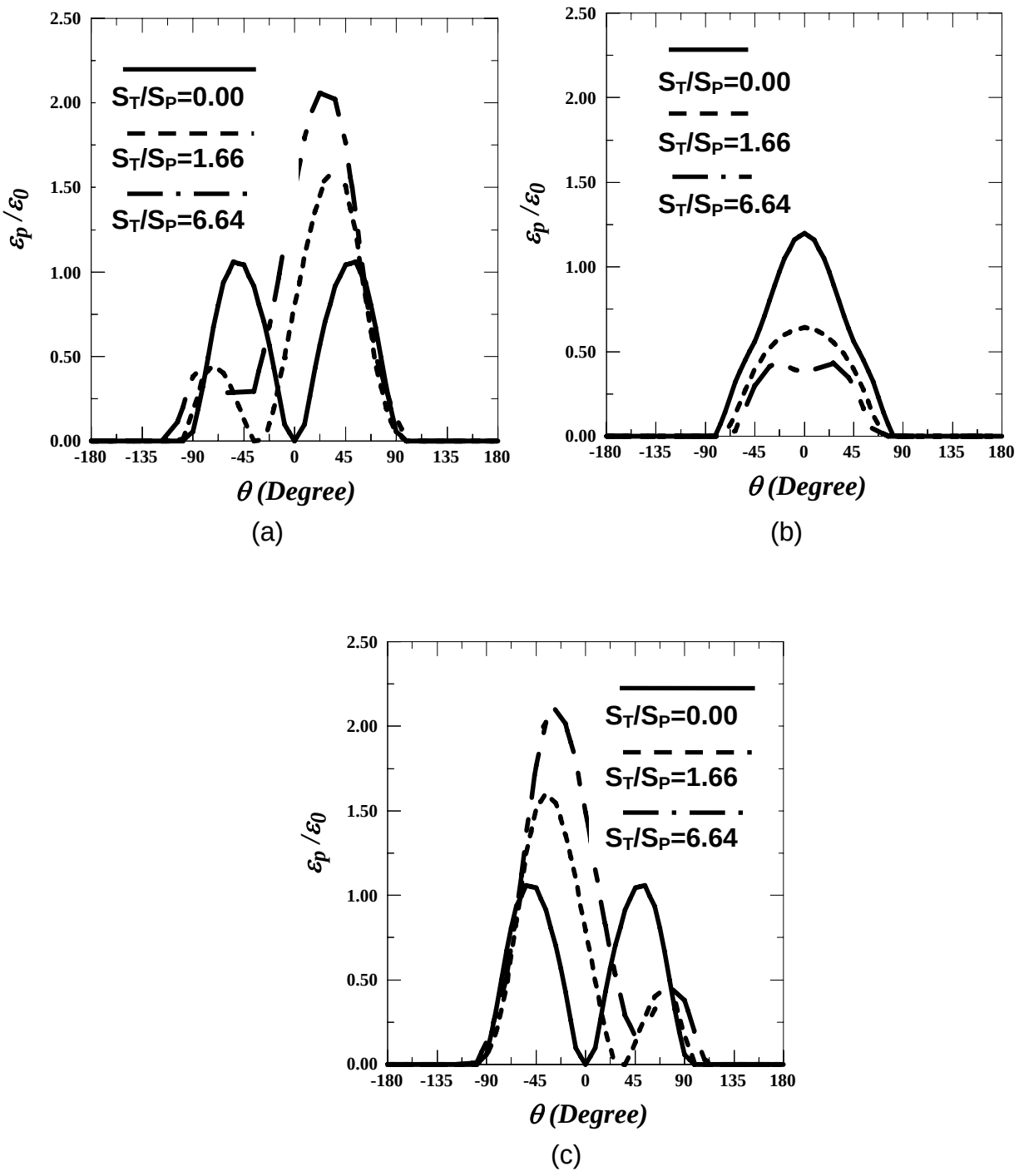

Fig. 11 Angular variations of the effective plastic strain (normalized by the initial yield strain) along r=1.50 mm around a flat crack: (a) on the front surface, (b) on the middle-plane, and (c) on the back surface.

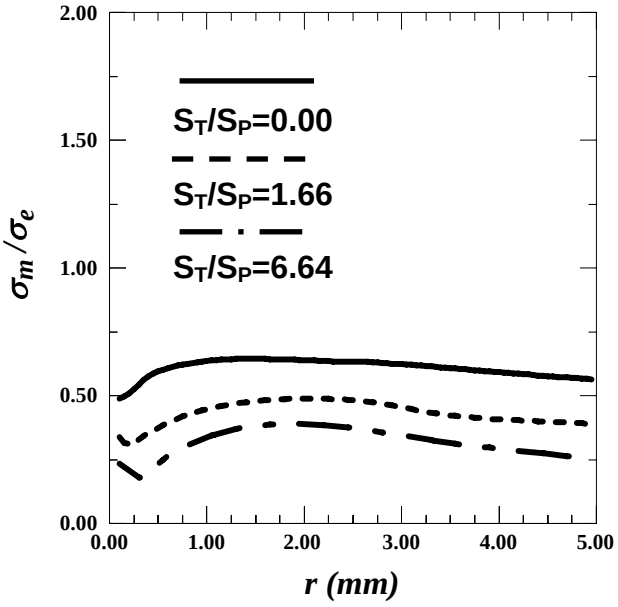

(a)

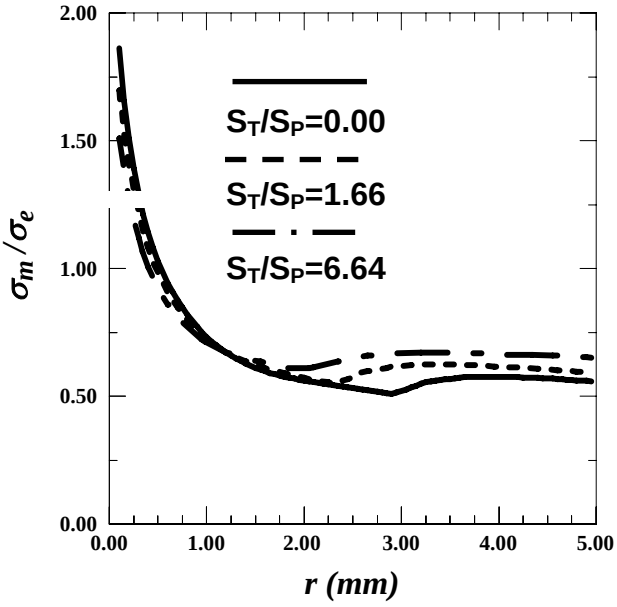

(b)

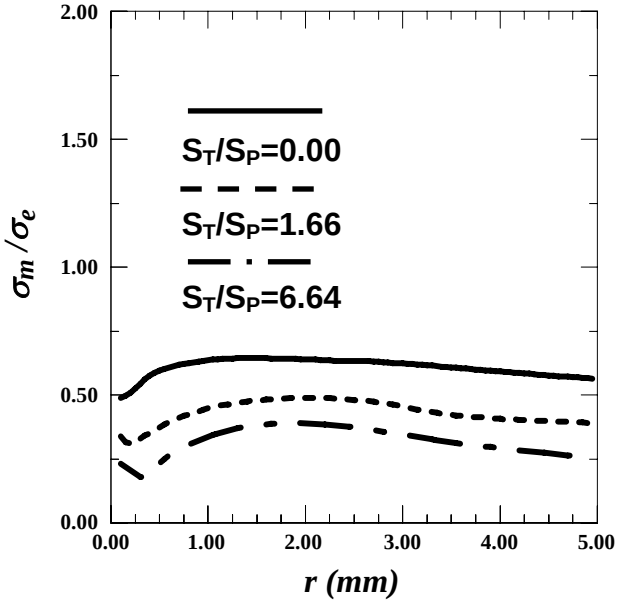

(c)

Fig. 12 Radial variations of the constraint along θ=0° ahead of a flat crack: (a) on the front surface, (b) on the middle-plane, and (c) on the back surface.

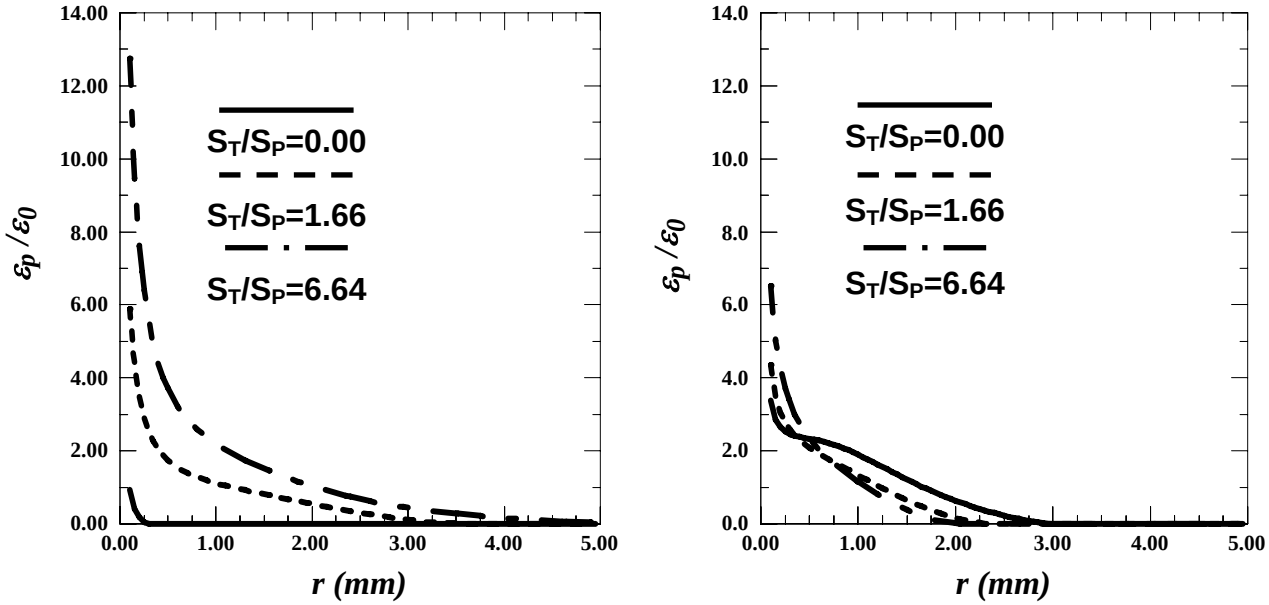

Fig. 13 Radial variation of the effective plastic strain (normalized by the initial yield strain) along θ=0° ahead of a flat crack: (a) on the front and back surfaces and (b) on the mid-plane.

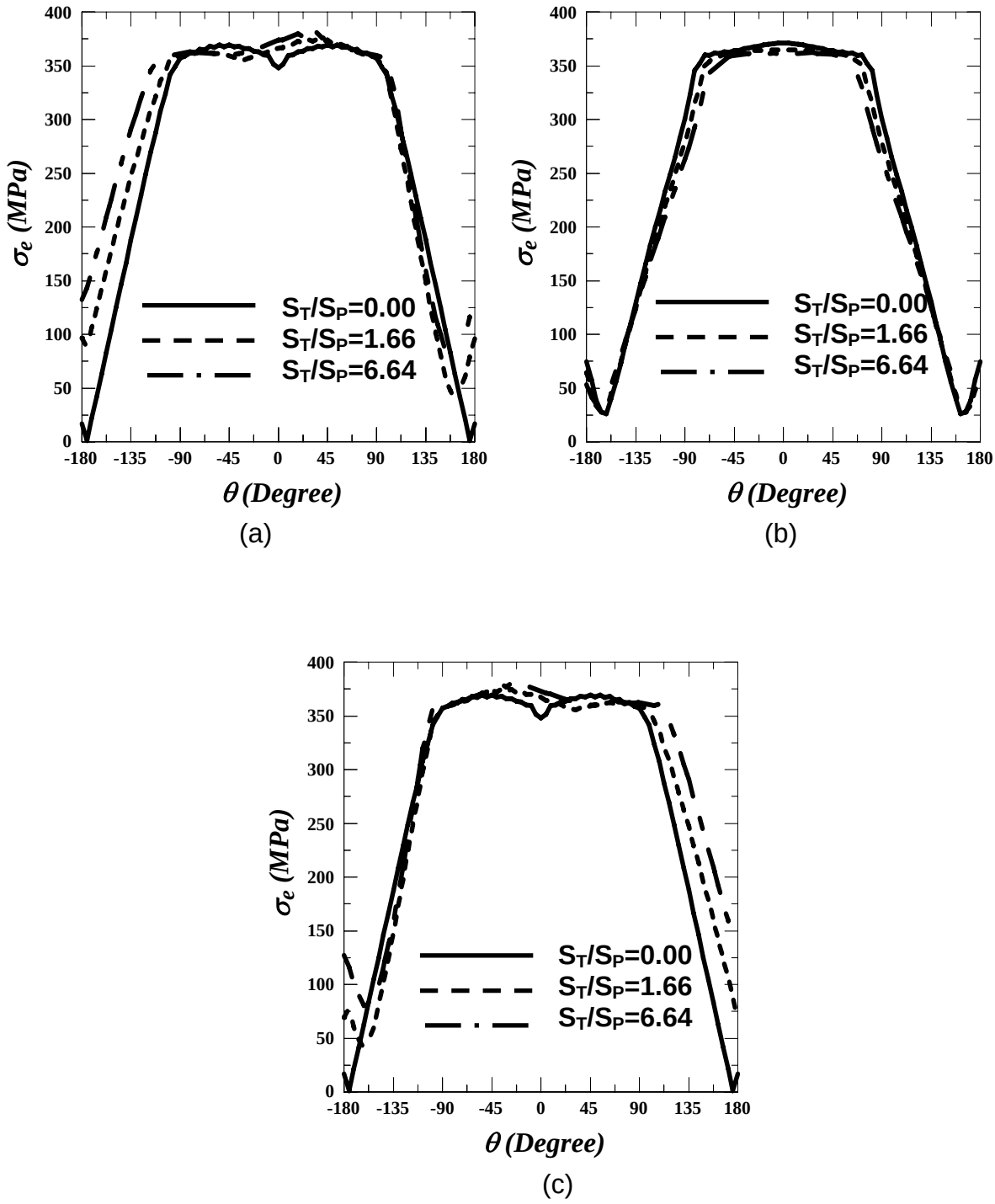

Fig. 14 Angular variations of the von Mises effective stress along r=1.50 mm around a flat crack: (a) on the front surface, (b) on the mid-plane, and (c) on the back surface.

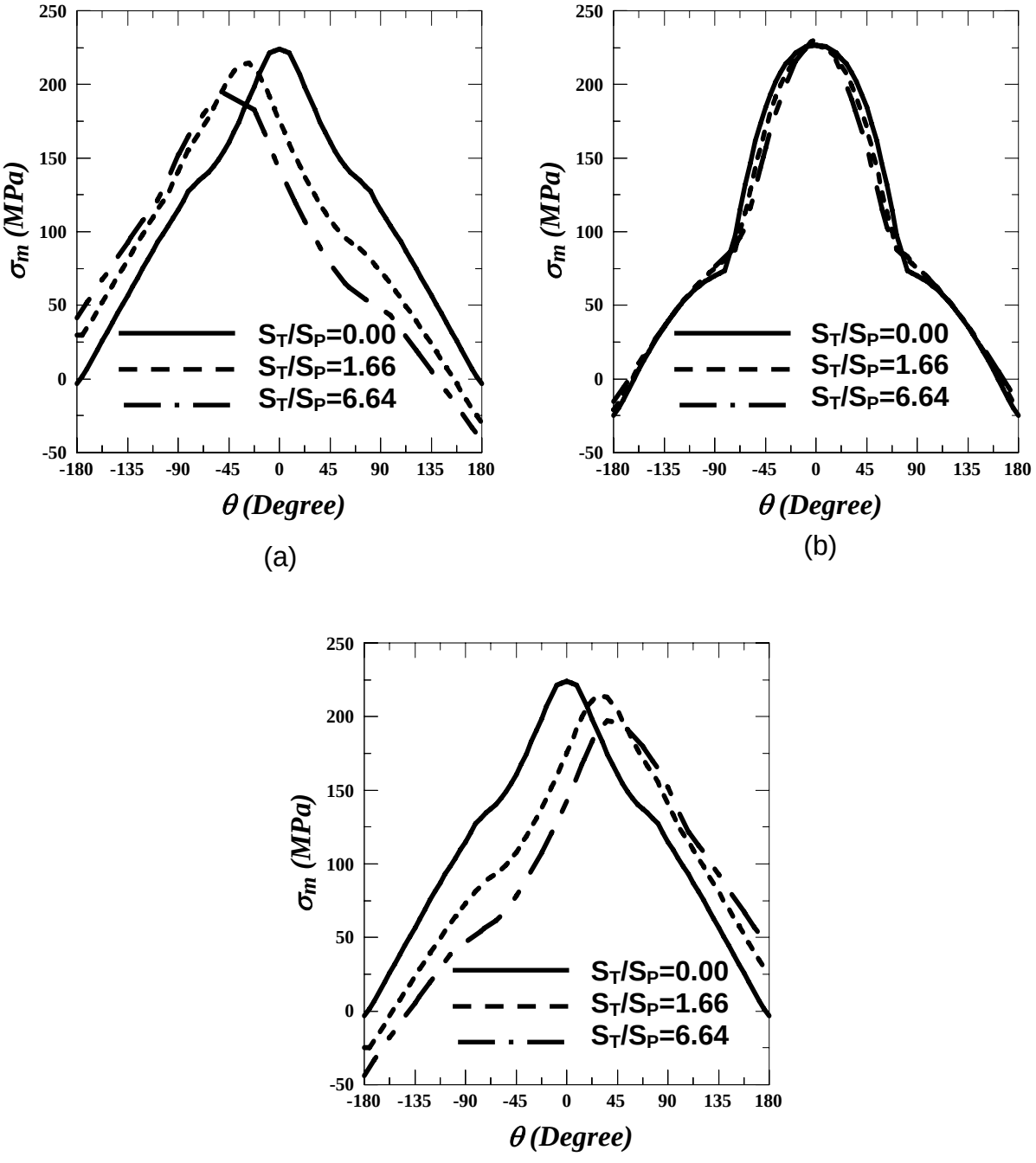

Fig. 15 Angular variations of the mean stress along r=1.50 mm around a flat crack: (a) on the front surface, (b) on the mid-plane, and (c) on the back surface.

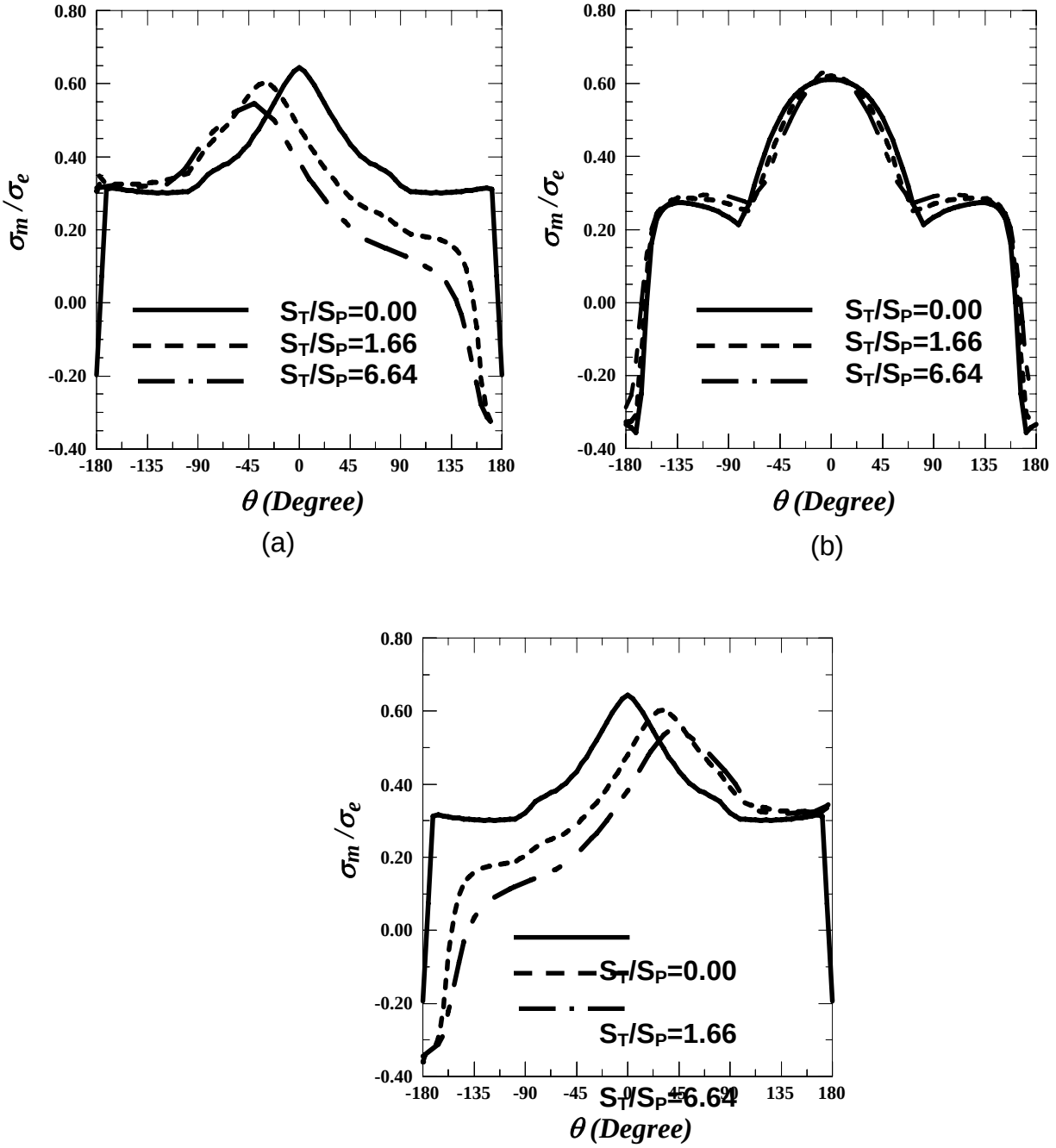

Fig. 16 Angular variations of the constraint along r=1.50 mm around a flat crack: (a) on the front surface, (b) on the mid-plane, and (c) on the back surface.

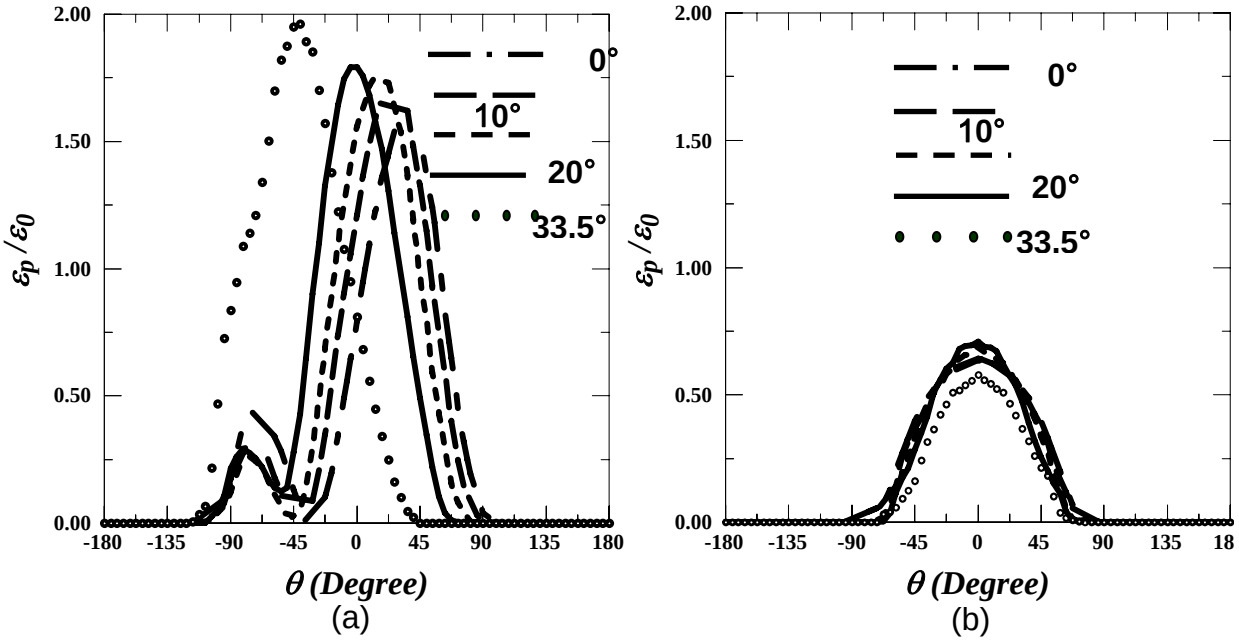

Fig. 17 Angular variations of the effective plastic strain along r=1.50 mm around slant cracks with various slant angles: (a) on the front surface and (b) on the mid-plane.

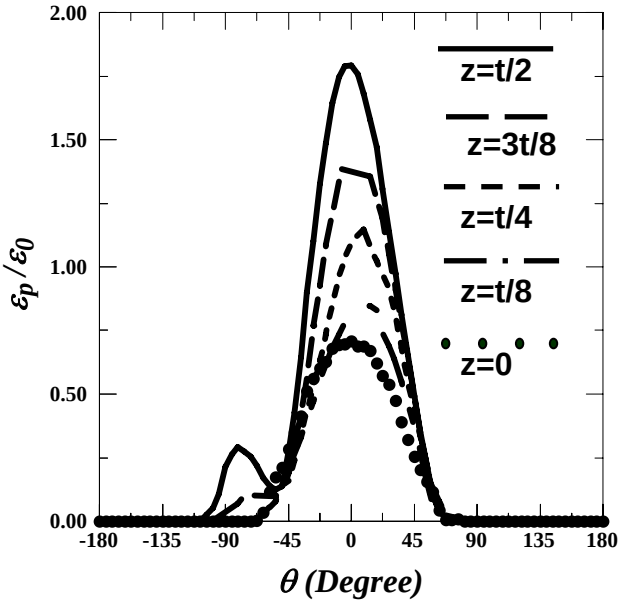

Fig. 18 Angular variations of the effective plastic strain along r=1.50 mm around a slant crack that equals the measured value on several through-thickness section planes.

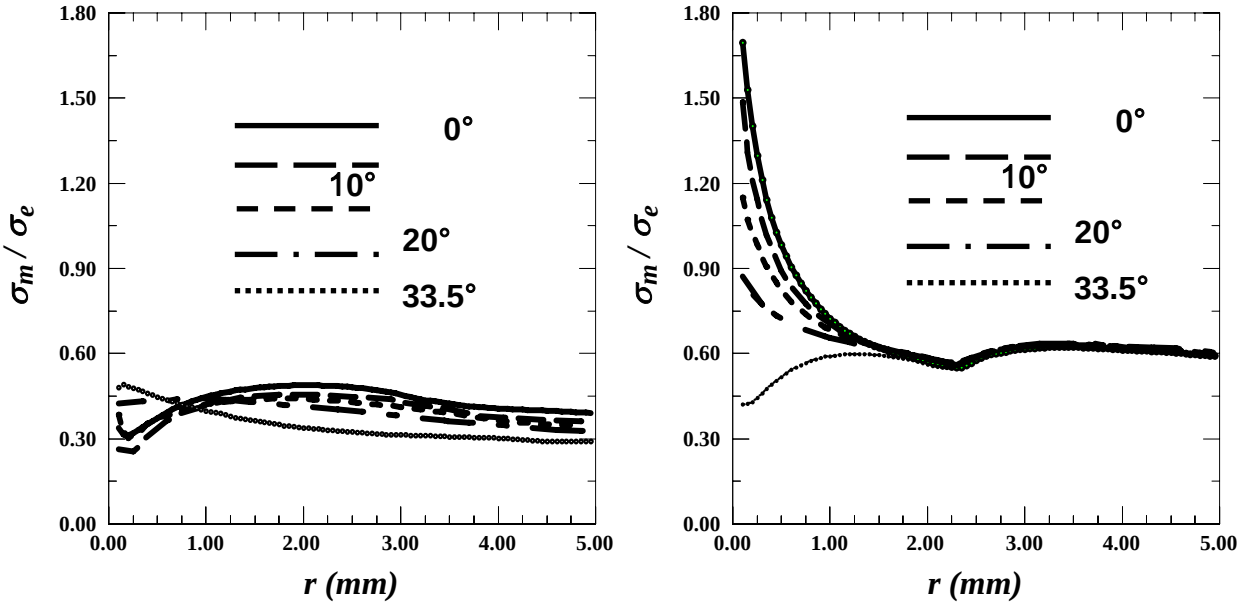

Fig. 19 Radial variations of the constraint along θ=0° around slant cracks with various slant angles: (a) on the front surface and (b) on the mid-plane.

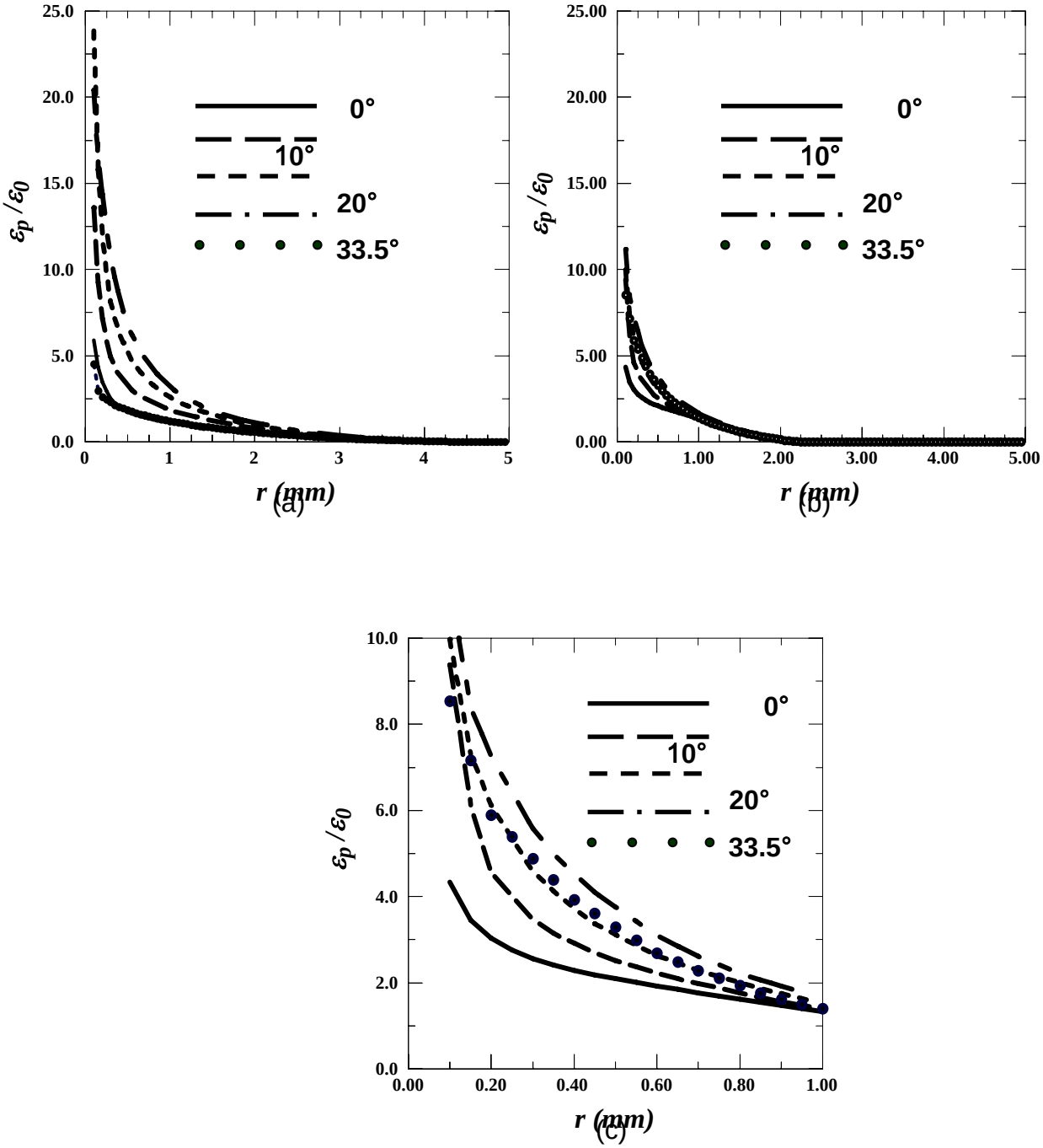

Fig. 20 Radial variations of the effective plastic strain along θ=0° around slant cracks with various slant angles: (a) on the front surface, (b) on the mid-plane, and (c) a local view of variations on the mid-plane.

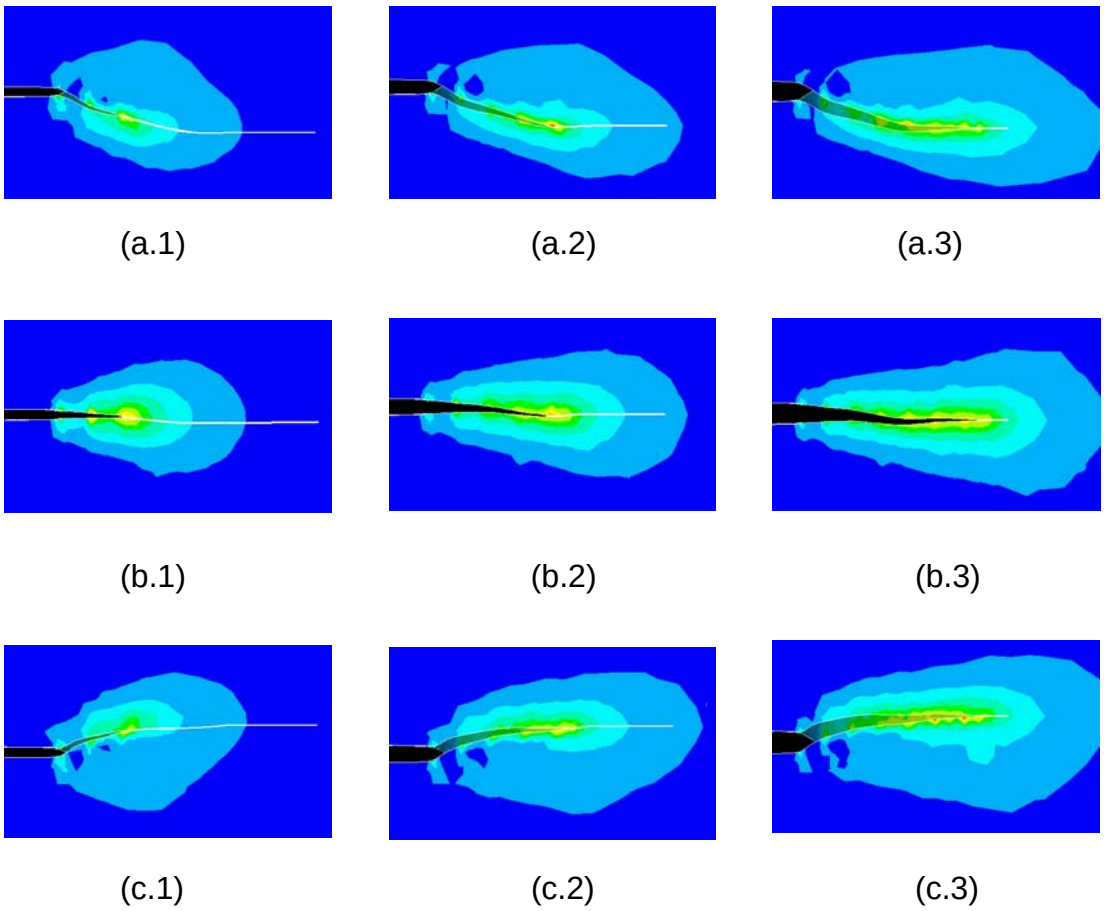

Fig. 21 Evolution of the effective plastic strain contours on (a) the front surface, (b) the mid-plane, and (c) the back surface, with a crack extension amount of (1) $\Delta a = 2.0\ mm$, (3) $\Delta a = 4.0\ mm$ and (3) $\Delta a = 6.0\ mm$.

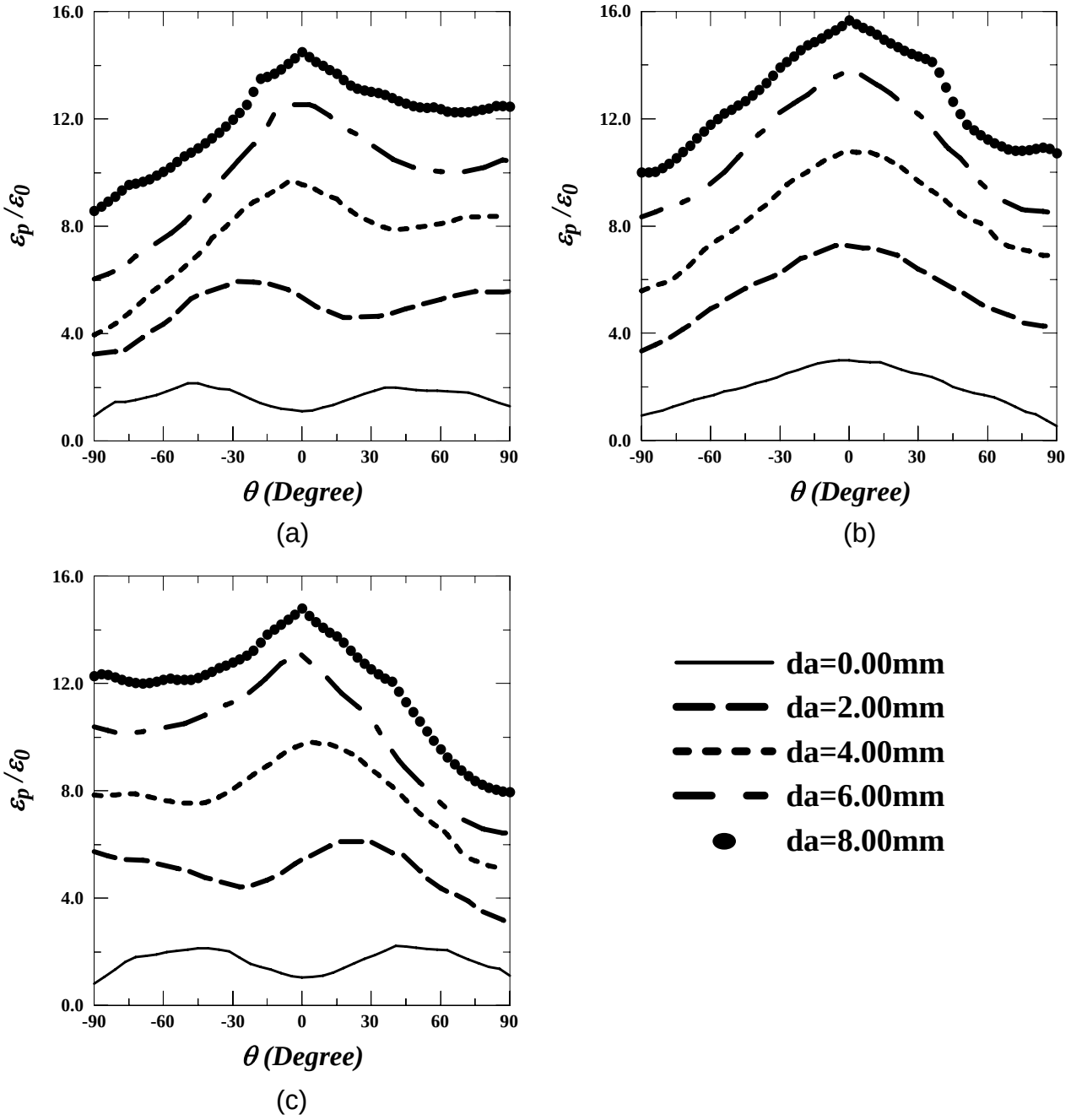

Fig. 22 Angular variations of the effective plastic strain along r=1.5 mm on (a) the front surface, (b) the middle plane and (c) the back surface, for various amounts of crack extension.

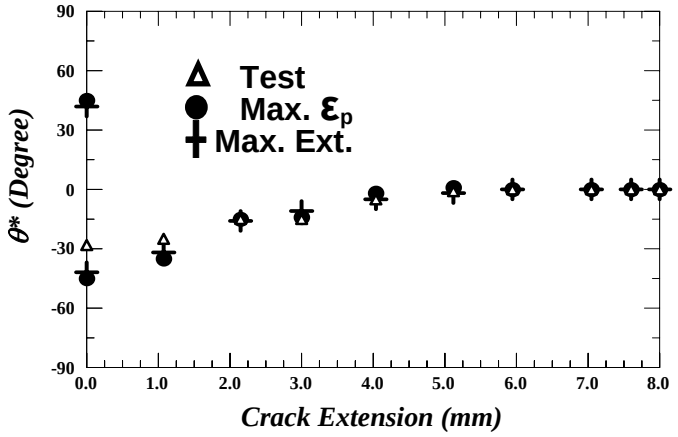

(a)

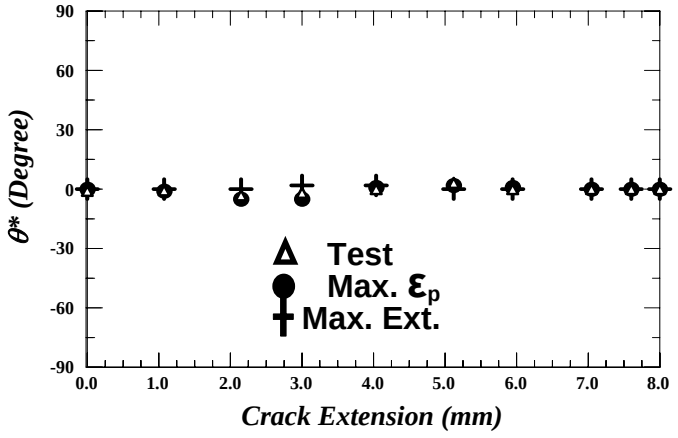

(b)

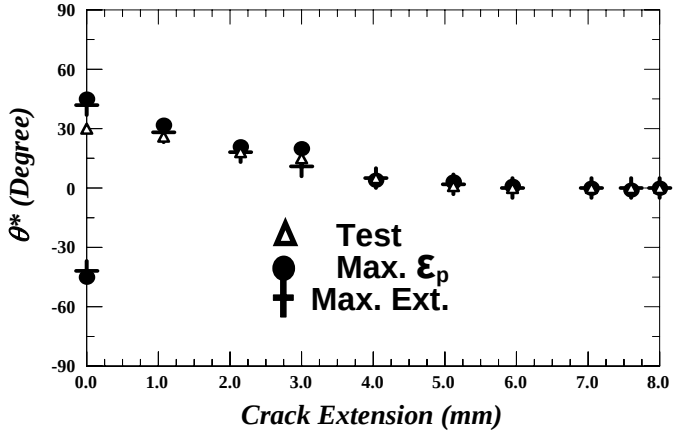

(c)

Fig. 23 Variation of θ^* with crack extension on (a) the front surface, (b) the mid-plane and (c) the back surface, where θ^* is the crack growth direction (for test), the angle at which the maximum ε_p occurs (for simulation), or the direction with the maximum extent of ε_p contours (for simulation). The angle θ^* is relative to the x-axis and is positive if counterclockwise.

V. List of Publications

1. Weiming Lan, Xiaomin Deng, MA Sutton and C.S. Cheng, “Study of slant fracture in ductile materials”, accepted for publication in the **International Journal for Fracture**

2. J. Zuo, X. Deng, and M. A. Sutton, “Advances in Tetrahedral Mesh Generation for Modeling of Three-dimensional Regions with Complex, Curvilinear Crack Shapes ***International Journal for Numerical Methods in Engineering***, 63 256-275 (2005).

3. J. Zuo, M. A. Sutton, and X. Deng, “Basic studies of ductile failure processes and implications for fracture prediction,” **Fatigue and Fracture of Engineering Materials and Structures**, 27, 231-243 (2004).

4. E. Mahgoub, X. Deng, and M. A. Sutton, “Three-dimensional stress and deformation fields around flat and slant cracks under remote Mode I loading conditions,” ***Engineering*** **Fracture Mechanics** 70 2527-2542 (2003).

5. J. Zuo, X. Deng, M.A. Sutton, and C-S Cheng “Crack Tunneling**:** Effect of Stress Constraint”, Paper # IMECE 2004-60700, ***Proc. of 2004 ASME International Mechanical Engineering Congress***, Nov. 13-20, 2004, Anaheim, CA.

6. J. Zuo, X. Deng and M. A. Sutton, “Computational Aspects of 3D Crack Growth Simulations”, Paper # IMECE 2004-60699***, Proc. of 2004 ASME International Mechanical Engineering Congress***, Nov. 13-20, 2004, Anaheim, CA.